

EXTRACELLULAR REGULATION AND SCALING OF SENSORY DENDRITES
AND TISSUE-SPECIFIC CRISPR MUTAGENESIS TOOLS IN *DROSOPHILA*

A Dissertation

Presented to the Faculty of the Graduate School

of Cornell University

In Partial Fulfillment of the Requirements for the Degree of

Doctor of Philosophy

by

Amy Rosetta Poe

December 2018

© 2018 Amy Rosetta Poe

EXTRACELLULAR REGULATION AND SCALING OF SENSORY DENDRITES
AND TISSUE-SPECIFIC CRISPR MUTAGENESIS TOOLS IN *DROSOPHILA*

Amy Rosetta Poe, Ph. D.

Cornell University 2018

The diverse and intricate dendritic branching patterns of neurons determine their ability to collect synaptic and sensory information. Defects in the formation and maintenance of dendritic patterns underlie many neurological disorders. Therefore, it is essential to understand how neurons develop dendritic arbors with the proper branching patterns in a complex nervous system. During animal development, many neurons establish dendritic territories early and then expand dendritic arbors proportionally to the body size in a process called scaling. Among those neurons, some are capable of filling empty space in the receptive field with highly dynamic dendritic branches. Dendritic scaling and space filling require an integration of intrinsic mechanisms, extracellular signals, and information about the organism's nutritional environment. To understand the multi-level mechanisms controlling dendrite branching, my research used *Drosophila* class IV dendritic arborization (da) neurons. For the first part of my thesis, I identified the epidermal cell-derived heparan sulfate proteoglycans (HSPGs), Dally and Sdc, as permissive signals for the space filling of class IV da neuron. We demonstrated that HSPGs stabilize dendrites by promoting microtubule stabilization. These data uncover novel pathways through which extracellular signals regulate dendritic space-filling in sensory neurons.

In the second part of my thesis, I examined the relationship between sensory

neuron and larval body growth under normal and nutrient stress conditions. My research revealed distinct cellular responses of sensory neurons and epidermal cells to nutrient restriction, with sensory dendrites growing preferentially under nutrient stress. Interestingly, autophagy and the expression of the transcription factor FoxO is suppressed in sensory neurons, making neurons insensitive to nutrient restriction. These experiments reveal distinctive molecular mechanisms regulating neuron/non-neural cell growth.

Finally, we developed and optimized a tissue-specific gene loss-of-function (LOF) strategy using the CRISPR/Cas9 system. This system allowed us to generate efficient tissue-specific gene knockout and to analyze redundantly acting genes in neural development. Using this strategy, we discovered the redundant and perdurant functions of SNARE components in dendrite morphogenesis. Together, my research reveals novel mechanisms in which extracellular signals, the nutritional environment, and redundantly acting genes regulate dendrite branching pattern formation.

BIOGRAPHICAL SKETCH

Amy Rosetta Poe was born and raised in Newnan, Georgia. She received her B.S. in Biology, *summa cum laude*, from Berry College in Mount Berry, Georgia in 2011. During her time in college, she completed an undergraduate honor's thesis on "Genetic Networks and Developmental Instability in *Drosophila melanogaster*" in the lab of Dr. John Graham. After graduation from college, she worked as a research technician at the Georgia Institute of Technology in the lab of Dr. Greg Gibson. She then began graduate school at Cornell University in August 2013.

ACKNOWLEDGMENTS

I would first like to thank my advisor, Chun Han, for his guidance and constant support. Chun is a very supportive mentor who is always willing to give advice and help (if needed) on experiments and research questions. Chun encouraged me to pursue teaching experiences as a graduate student and provided me with many opportunities to teach and mentor students in the lab. I would also like to thank my committee members, Mariana Wolfner and David Deitcher, for their helpful advice and suggestions.

I would also like to acknowledge the past and present members of the Han lab for their help with experiments and making the lab a great place to work every day. In particular, I would like to thank Maria Sapar and Hui Ji for their support and advice on experiments. I would also like to thank Kathy Wang for making many of the reagents used in the lab.

Finally, I would like to thank my parents and other family members for their support throughout graduate school.

TABLE OF CONTENTS

BIOGRAPHICAL SKETCH.....	v
ACKNOWLEDGMENTS.....	vi
TABLE OF CONTENTS.....	vii
LIST OF FIGURES.....	viii
LIST OF TABLES.....	xi
CHAPTER 1: Introduction.....	1
CHAPTER 2: Dendritic space-filling requires a neuronal type-specific extracellular permissive signal in <i>Drosophila</i>	35
CHAPTER 3: Robust CRISPR/Cas9-mediated tissue specific mutagenesis reveals gene redundancy and perdurance in <i>Drosophila</i>	97
CHAPTER 4: Suppression of FoxO expression and autophagy underlies preferential dendrite growth of <i>Drosophila</i> neurons during nutrient restriction.....	141
CHAPTER 5: General Discussion.....	177

LIST OF FIGURES

Figure	Page
1.1. Model Systems for Studying Dendrite Morphogenesis	3
1.2. Extrinsic and Intrinsic Mechanisms Regulating Dendrite Morphogenesis	9
1.3. Dendrite Patterning and Field Organization	15
1.4. Tissue-specific Gene Manipulation in <i>Drosophila</i>	24
2.1. Epidermis-derived HSPGs are required for local growth of C4da dendrites.	42
2.S1. Effects of knockdown of HS synthesis genes on dendrite morphology, HS level, and epithelial morphology.	44
2.2. HSPGs are specifically required for dendrite development of C4da neurons.	47
2.S2. HSPGs are not required for dendrite growth of other classes of da neurons.	49
2.3. Sdc and dally play partially redundant roles in promoting dendritic growth of C4da neurons.	52
2.S3. Effectiveness and specificity of HSPG RNAi.	54
2.4. HSPGs stabilize high-order C4da dendrites by promoting microtubule bundling.	58
2.S4. Dynamics of EB1-GFP in <i>ttv</i> knockdown.	61
2.5. HSPGs do not promote dendritic growth by transporting diffusible signals.	64
2.6. Ptp69D but not Lar is necessary for C4da dendritic growth.	68
2.S5. Lar and Ptp69D reporters, mutations, expressions and LOF phenotypes.	70

2.7. HSPGs and Ptp69D act in different genetic pathways.	74
2.S6. Lar and Ptp69D do not play redundant roles in dendrite development of C4da neurons.	76
2.8. A model for the roles of HSPGs and Ptp69D in dendritic growth.	79
3.1. Generation and evaluation of tissue-specific Cas9 lines.	103
3.2. Optimization of multi-gRNA design for tissue-specific gene knockout in Drosophila.	108
3.3. Efficiency of dual gRNA-mediated DNA deletion at the single cell level.	111
3.4. Enhancer-driven Cas9 is advantageous over Gal4-driven Cas9 in studying neural development.	114
3.S1. Cas9-LEThAL assay.	117
3.5. Post-mitotic knockout of Ptp69D is sufficient to reveal its function in C4da neurons.	119
3.S2. LOF of individual NSF and SNAP genes in C4da neurons.	123
3.6. CRISPR-TRiM analyses of NSF and SNAP genes in C4da dendrite morphogenesis.	125
4.1. C4da neurons exhibit a growth advantage under nutrient deprivation.	146
4.S1. Segment width provides a reliable measurement of animal size.	147
4.2. Preferential neuronal growth relies on InR-Tor signaling.	150
4.S2. InR-Tor signaling is necessary for neuronal cell growth.	152
4.3. Neurons exhibit suppression of autophagy under nutrient deprivation.	156
4.4. Differential responses of other classes of da neurons under nutrient deprivation.	159
4.5. FoxO activity underlies differential growth of neurons and epidermal cells.	161

LIST OF TABLES

Table	Page
3.S1. List of positive and negative tester lines, related to Figure 3.1.	105
3.S2. Results of the Cas9-LEThAL assay.	118

CHAPTER 1

INTRODUCTION

As highly polarized cells with a typical structure consisting of a cell body, axon, and dendrites, neurons are essential building blocks of a functional nervous system. Neurons exhibit complex and diverse dendritic branching patterns with some neurons only growing very few dendrites and some developing highly arborized, complex structures. As an organism develops, coordinated dendritic growth and branching establish the neuron's receptive field allowing for sampling of synaptic inputs (1). Moreover, both intracellular (intrinsic) and extracellular (extrinsic) mechanisms regulate dendritic growth and branching patterns (1). Defects in dendrite branching patterns and maintenance contribute to many neurological and neurodevelopmental disorders including autism, Fragile X syndrome, Rett syndrome and Down syndrome (2). Therefore, understanding the molecular mechanisms regulating dendrite branch formation provides critical insight into nervous system development and functioning.

In the past few decades, major progress has been made in understanding the molecular and cellular mechanisms regulating dendrite morphogenesis (1). Using many model organisms including *Drosophila*, *C. elegans*, and zebrafish, prior studies have determined the mechanisms controlling dendrite growth, dendritic field size, organization, and branching patterns (1, 3). Despite this prior extensive analysis of dendrite morphogenesis in many model organisms, many questions still remain. First, how do neurons achieve their type-specific dendrite branching patterns? What role do extracellular signals play in dendrite morphogenesis? How do both intrinsic and extrinsic mechanisms integrate to regulate dendrite growth? Finally, during development, how does overall animal growth coordinate with dendrite growth of peripheral sensory neurons?

In this chapter, I will first provide an overview of the various model systems used for studying dendrite morphogenesis. I will then summarize the general cellular and molecular mechanisms regulating dendrite morphogenesis focusing primarily on *Drosophila* dendritic arborization neurons. Next, I will examine the roles by which extracellular signals and the surrounding cellular environment influence dendrite branching patterns. I will then address how both intrinsic and extrinsic mechanisms integrate to coordinate dendrite growth with overall animal body growth. Lastly, I will discuss methods for performing tissue-specific gene manipulation in *Drosophila*.

Popular Model Systems for Studying Dendrite Morphogenesis

Several neuronal systems have been successfully used to study dendrite morphogenesis in a variety of model organisms. Study of these model systems has uncovered many of the molecular and cellular mechanisms regulating dendrite growth. However, each system has its own advantages and disadvantages. I will briefly describe each model system, its advantages, and any potential limitations. Figure 1.1 provides a visual summary of all the model systems discussed in this section.

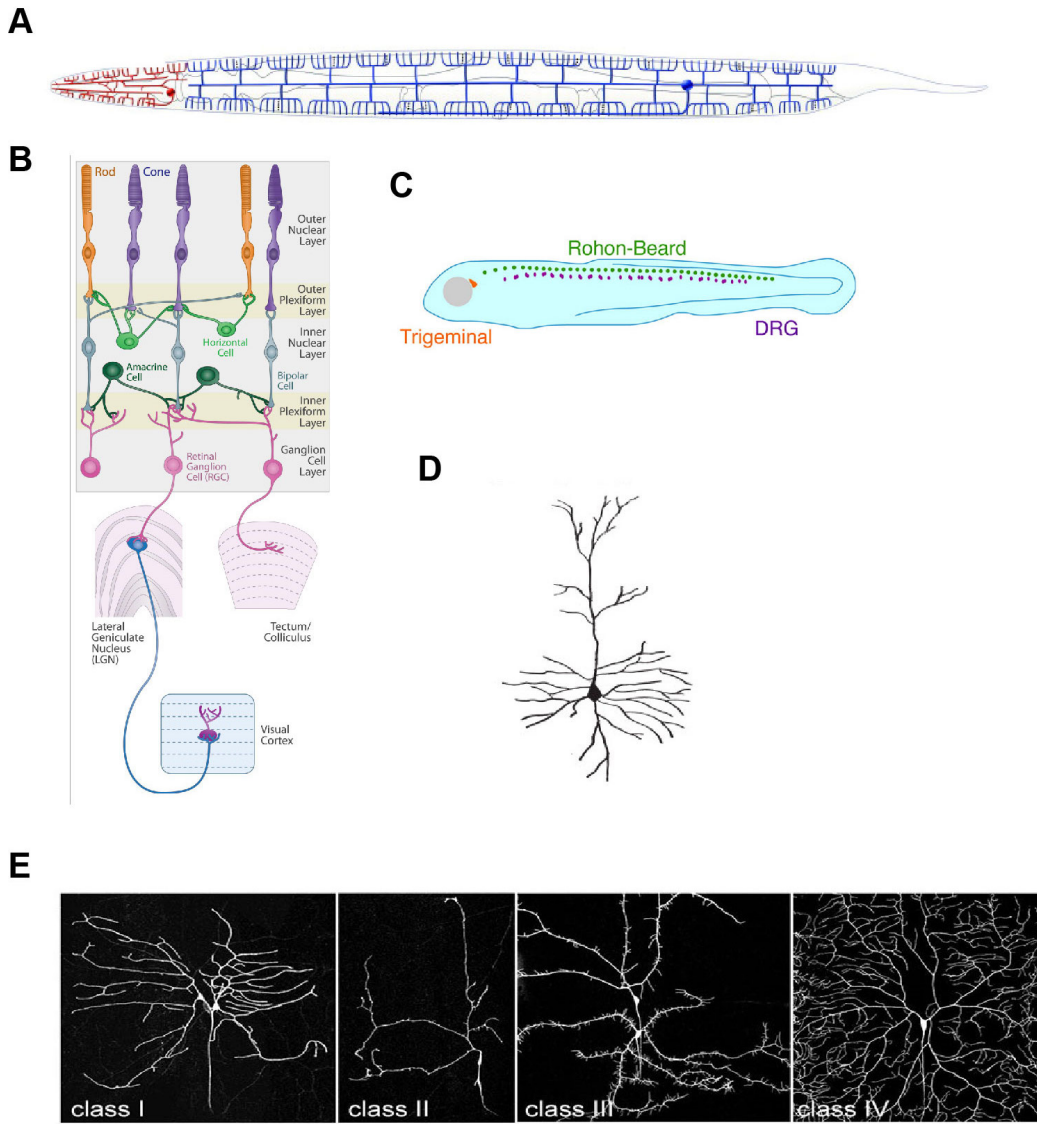


Figure 1.1. Model Systems for Studying Dendrite Morphogenesis. (A) A diagram showing the typical morphology of the *C. elegans* PVD neuron (in blue) and FLP neuron (in red) covering the adult worm. Average field size of PVD neurons is 125-150 μm (4). Image was adapted from (5). (B) Retinal ganglion cells (RGCs) and amacrine cells occupy distinct layers of the vertebrate retina as shown in this diagram. Field size of RGCs varies based on cell type with an average size of 400 μm in mice (6). Image was adapted from (7). (C) The three types of zebrafish somatosensory neurons including the trigeminal, dorsal root ganglia (DRG), and Rohon-Beard (RB) neurons which project sensory axons covering the trunk and tail of the larval fish. Average field size of RB neurons is 2.1-2.4 mm (8). Image was adapted from (9). (D) Vertebrate pyramidal neurons have apical and basal dendrites originating from a pyramid-shaped soma. Field size varies based on organism. In humans, the average apical dendrite length is 1.5 mm (10). Image was adapted from (11). (E) The four classes of *Drosophila* dendritic arborization (da) neurons have unique branching patterns. Average field size is between 200-500 μm . Images were taken by Chun Han. Refer to the text for more information on each model system.

Caenorhabditis elegans PVD and FLP neurons

The PVD and FLP neurons are highly branched mechanosensory neurons which cover the entire body of the adult worm (4, 12). There is one FLP neuron on each side of the worm head and there are two PVD neurons (PVDL and PVDR) covering the two sides of the body (4). These neurons respond to harsh mechanical stimuli, cold temperature, and are necessary for normal animal locomotion (4). The cell bodies of the PVD neurons are born in the L2 stage of larval development. As the larva develops, the primary (1°) branch extends anteriorly and posteriorly. Next, secondary (2°) branches develop at periodic intervals from the primary branch in the dorsal and ventral direction (perpendicular to the primary branch). In the L3 stage, tertiary (3°) branches extend from the 2° branches and finally quaternary (4°) branches form. The 4° branches extend their dendrites in a two-dimensional space between the hypodermis and muscle (4, 12). By the adult stage, the PVD neuron has a characteristic candelabra-like branching pattern which envelops the entire animal in dendrites in a non-overlapping manner (4, 12) (Figure 1.1A).

The extensive genetic and imaging techniques available in *C. elegans* make the PVD neurons an excellent model system for studying dendrite morphogenesis. Because the 4° branches develop in a two-dimensional cellular environment, this provides the opportunity to study how extracellular signals and dendrite-substrate interactions control overall dendrite morphogenesis.

Zebrafish Rohon-Beard (RB) neurons

Zebrafish have three types of somatosensory neurons which innervate the epidermis and detect touch sensation. The trigeminal neurons innervate the head region and the dorsal root ganglia (DRG) neurons innervate the rest of the body in the adult fish. Zebrafish larvae also have a transient population of neurons called Rohon-Beard (RB) neurons which are located in the

dorsal spinal cord (Figure 1.1C). The RB neurons project peripheral axons covering the trunk and tail and are present until the DRGs develop (9, 13). The RB neurons elaborate their axons beneath the skin between 16 hrs post-fertilization (hpf) and 36 hpf (9). Recent studies have looked at the extracellular mechanisms regulating RB axon guidance from the dorsal spinal cord to the larval epidermis (13, 14).

One advantage of this system is the ability to perform *in vivo* imaging of developing RB neurons in zebrafish larvae using recently developed transgenic reporters (8). Imaging of developing RB neurons allows for the identification of extracellular signals that guide the peripheral axons to the skin. However, genetic analysis in zebrafish is often complicated by unreliable, labor-intensive loss-of-function techniques such as morpholinos (15) and the presence of multiple redundantly acting genes. Additionally, *in vivo* expression analysis of genes of interest cannot be performed as easily as in other model systems.

Vertebrate retinal ganglion cells (RGCs) and amacrine cells

The vertebrate retina is composed of six cell types organized into three distinct “nuclear” layers separated by two “plexiform” layers (Figure 1.1B) (5). The outer nuclear layer contains the cell bodies for photoreceptors, the inner nuclear layer contains the cell bodies for interneurons including amacrine cells and bipolar cells, and the ganglion cell layer contains the cell bodies for retinal ganglion cells (RGCs). RGCs extend their dendrites from the ganglion cell layer into the inner plexiform layer (IPL) which also contains the dendrites of amacrine cells and axonal terminals of bipolar cells (1, 7). The IPL can be subdivided into multiple sublaminae with each sublamina containing distinct cell types (7). A remarkable feature of this system is that in the mammalian retina there are at least 20 types of RGCs, 30 types of amacrine cells, and 11 types of bipolar cells which together cover or tile the entire retina (1). Additionally, each type of

RGC targets its dendritic arbors to one specific sublamina corresponding to a distinct functional role. For example, cells that depolarize in response to increased illumination (the ON type) make up one half of the IPL and cells that hyperpolarize in response to increased illumination (the OFF type) make up the other half of the IPL (16-19).

Understanding the mechanisms by which different RGC types achieve laminar specificity is of considerable interest. In vivo imaging of zebrafish RGCs and amacrine cells indicates that some RGCs extend their dendrites into the appropriate lamina from the onset of circuit formation (18). Additional studies in mice indicate that RGC targeting is subject to dendritic remodeling and retractions to achieve laminar specificity (20). Homophilic adhesion molecules such as Dscam and Sidekick are expressed in distinct sublaminae layers by non-overlapping subsets of interneurons and RGCs in distinct sublaminae layers. Expression of these adhesion molecules plays a role in determining the laminar specificity of synapses (21). Extracellular cues such as Semaphorins and their receptors, Plexins, have also been shown to guide dendritic arbors to the appropriate laminar region (22).

One advantage of this system is the ability to study interactions between different cell types to achieve laminar specificity and tiling of the retina. Imaging studies in zebrafish also allow for in vivo analysis of RGC dendrite dynamics and targeting. However, analysis of mouse RGCs relies on immunohistochemistry and more laborious genetic techniques which can complicate studies of dendrite morphogenesis.

Drosophila melanogaster dendritic arborization (da) neurons

The dendritic arborization (da) neurons of *Drosophila* larvae are multi-dendritic sensory neurons part of the peripheral nervous system (23). The da neurons grow along the larval body wall in a two-dimensional space between epidermal cells and muscle which allows for easy

visualization of dendrite branching patterns with fluorescent markers (24, 25). The da neurons are classified into four classes (Class I, II, III, & IV) based on their dendrite branching patterns (23) (Figure 1.1E). Each side of the larval abdominal hemisegment has three Class I (C1) da neurons, four Class II (C2) da neurons, five Class III (C3) da neurons, and three Class IV (C4) da neurons (3). The C1 and C2 da neurons have simpler dendritic branching patterns and the C4 da neurons have the most complex branching pattern with the largest receptive field (23). As space-filling neurons, the C4 da neurons completely and nonredundantly fill their receptive fields with evenly spaced dendrites (26). Additionally, the four classes of da neurons have their own unique physiological functions in the larval nervous system (27-30). The C4 da neurons are nociceptive neurons which respond to harsh mechanical stimuli and high temperatures (27). While dendrites of the same neuron or the same class of neuron typically do not overlap with each other, the four classes of da neurons have overlapping dendritic fields that innervate the larval epidermis (23).

The da neuron model system has several advantages for studying the mechanisms regulating dendrite morphogenesis. First, the da neurons can be genetically manipulated using many common *Drosophila* techniques including the Gal4/UAS system, mosaic analysis with repressible cell marker (MARCM) (31) and mutagenesis screens. With the additional advantage of GEEM (Gene Expression with an independent Enhancer-driven cellular Marker) (24), da neuron morphology can be visualized while manipulating genes of interest in other neighboring tissues with the Gal4/UAS system. The presence of multiple classes of da neurons in the same cellular microenvironment also provides a unique system for studying extracellular regulation of dendrite development. Therefore, the da neurons are an excellent model system for uncovering the molecular mechanisms regulating dendrite morphogenesis.

Vertebrate pyramidal neurons

The pyramidal neurons in the vertebrate cortex and hippocampus have a characteristic morphology consisting of apical and basal dendrites originating from a pyramid-shaped soma (Figure 1.1D). There are typically several short basal dendrites and one large apical dendrite connecting the soma to a tuft of dendrites (32). The dendrite branching patterns of these neurons can vary depending on the neuron's location in the brain (32). During development, the neurons in the cortex and hippocampus undergo migration to specified locations which allows them to form connections with other neurons (33). The hippocampal pyramidal neurons process sensory and motor information and convey the output to targets throughout the brain (34).

The cortical pyramidal neurons convey information from the cerebral cortex to various cortical and subcortical targets (35). These neurons are born in the ventricular zone and then migrate along radial glial cells into the cortical plate (1, 36). During the migration, the leading process or apical dendrite is attracted to the pial surface by the extracellular chemoattractant, Semaphorin 3A (37). Additional extracellular factors such as BDNF, Notch, and Slit then control the growth and branching of high-order dendrites in the cortical pyramidal neurons (36).

Because the development of pyramidal neurons is difficult to trace using *in vivo* studies, these neurons are cultured on cortical slices (1). This technical disadvantage makes it difficult to study real-time dendrite dynamics and dendrite-substrate interactions during development. However, culturing these neurons does allow for the identification of extrinsic signals and chemical signals necessary for dendrite guidance and branching.

Intrinsic Mechanisms Regulating Dendrite Morphogenesis

Although organisms possess multiple neuronal cell types with diverse dendritic branching patterns, there are several general molecular mechanisms which regulate dendrite morphogenesis. Intrinsic mechanisms such as transcription factors, cytoskeleton regulators, and

motor proteins (1) play key roles in regulating dendrite patterning. In this section, I will summarize the key aspects of intrinsic regulation of dendrite branching patterns focusing primarily on *Drosophila* da neurons. However, many of these proteins and pathways are conserved and are necessary for dendrite development in other model systems (1). When appropriate, I will also provide examples of intrinsic regulation of dendrite branching patterns in other model systems. Figure 1.2 provides an overview of the intrinsic and extrinsic mechanisms regulating dendrite morphogenesis.

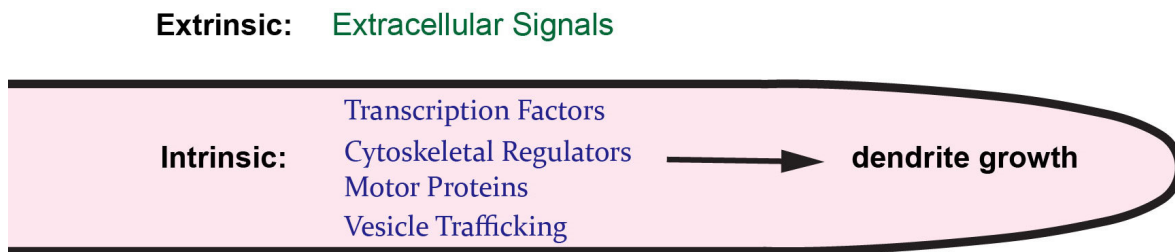


Figure 1.2. Extrinsic and Intrinsic Mechanisms Regulating Dendrite Morphogenesis. A diagram showing the general intrinsic and extrinsic mechanisms regulating dendrite growth. General intrinsic factors include varying levels and combinations of transcription factors, cytoskeletal regulators, motor proteins for vesicle transport, and the secretory/endocytic pathways. Refer to the text for details on each of these mechanisms. The dendrite image was adapted from Figure 2.8.

The specification and dendrite morphology of the four classes of da neurons are determined by varying combinations and expression levels of several key transcription factors (3). The zinc finger transcription factor, *Abrupt*, is highly expressed in C1da neurons, but not in the other classes (38, 39). Ectopic expression of *Abrupt* in the other classes leads to simplified dendritic arbors (38, 39) which suggests that *Abrupt* is necessary for ensuring the simpler morphology of the C1da neurons. In a complementary manner, the homeobox transcription factor *Cut* is highly expressed in C3da neurons and is expressed at intermediate levels in C4da

neurons, but is expressed at very low levels in C1da and C2da neurons (40, 41). Genetic studies indicate that the levels of Cut expression in each class of da neuron determine the unique patterning for that class (41). Loss of *cut* in C3da neurons causes a reduction in dendritic branching (41). In cortical pyramidal neurons, the vertebrate orthologs, Cux1 and Cux2, have also been shown to be necessary for dendrite branching and the formation of dendritic spines (42, 43). In mice, both Cux1 and Cux2 promote dendrite branching and synapse formation in layer II-III neurons of the cortex (43). Additionally, the transcription factor Collier (or Knot) is highly expressed in C4da neurons, but not in the other classes (44-46). Ectopic expression of Collier/Knot in the other classes results in an increase in branching complexity indicating that Collier/Knot is necessary for complex dendrite branching patterns (45). A fourth transcription factor, Spineless, is expressed in all four classes of da neurons and may enable dendrite diversification in response to other transcription factors (47). Loss of *spineless* in C1da and C2da neurons causes an increase in branching complexity and its loss in C3da and C4da neurons causes a decrease in branching complexity (47). In combination, these four transcription factors determine the identity and overall morphological characteristics of the four classes of da neurons.

Cellular Processes Regulating Dendrite Branching

Highly arborized neurons such as the C4da neuron extend their dendritic branches over large distances from the cell body. This large distance from the cell body requires the cell to transport the necessary building blocks for dendrite expansion over a considerable distance during animal development. The *Drosophila* dendritic cytoskeleton contains actin and microtubules which allows for the transport of necessary building blocks in the form of vesicles to the plasma membrane. Motor proteins are essential for the transport of these vesicles along the cytoskeleton to the plasma membrane resulting in an expansion of the dendritic arbor and an

overall increase in dendrite growth. Additionally, the secretory and endocytic pathways together regulate the secretion and transport of lipid and protein components to and from the plasma membrane. In this sub-section, I will discuss the roles each of these components play in regulating dendrite morphogenesis focusing first on the dendritic cytoskeleton, then motor proteins such as dynein and kinesin, and finally discussing the secretory and endocytic pathways.

Actin and microtubule regulators play an important role in regulating overall dendritic branching patterns. The Rho family of GTPases cycle between an active, GTP-bound form and an inactive GDP-bound form to control actin polymerization. Loss-of-function studies have shown that the Rho GTPase, Rac1, is necessary for C4da dendrite growth (48). Additional studies have shown that other regulators of actin dynamics such as the actin-stabilizing protein Tropomyosin and actin nucleation protein Spire are necessary for dendritic growth and branching in the C4da neurons (49, 50). Regulators of microtubule assembly also play essential roles in dendrite growth. For example, regulation of microtubule disassembly through the activity of the microtubule severing proteins, Katanin and Spastin, is necessary for C4da dendrite growth and functioning (51). Furthermore, phosphorylation of β -tubulin by the Minibrain (MNB)/DYRK1a kinase inhibits microtubule polymerization in C3da neurons leading to a reduction in terminal dendrite growth (52).

Microtubules in the dendritic arbor provide a track for dynein and kinesin motors to move vesicles and organelles to and from the dendritic membrane. This vesicular transport of organelles is necessary for dendrite development. Loss of dynein or kinesin motor activity in C4da neurons causes a substantial decrease and shrinking of the entire dendritic arbor (53, 54). Loss-of-function mutations of dynein motor genes such as *Dlic* (dynein light intermediate chain) in C4da neurons altered the distribution of endosomes, mitochondria, and Golgi outposts

(discussed below) in the dendritic arbor (54). These studies indicate that dynein motor activity is necessary for transporting these organelles to the microtubule minus-end thereby promoting distal dendrite growth (53, 54). Similar dendritic reduction phenotypes are also observed in C4da neurons of animals with mutations in the dynein cofactor, NudE (55). Additionally, the coil-coiled adaptor protein golgin/Lava Lamp (43) which links the Golgi with the dynein-dynactin complex, is necessary for C4da dendrite growth. Knockdown of *lva* in C4da neurons using RNA interference (RNAi) caused a severe reduction in dendrite growth (56). Together, these studies indicate that dynein motor activity is essential for C4da dendrite expansion.

The secretory and endocytic pathways are also necessary for dendritic growth. In hippocampal pyramidal neurons, specialized Golgi compartments called Golgi outposts concentrate at dendritic branchpoints suggesting that the secretory pathway is necessary for directed dendrite growth (57). A genetic screen in *Drosophila* da neurons identified mutations in *dendritic arbor reduction* (*dar2*, *dar3*, and *dar6*) genes as necessary for C4da dendritic development (56). These genes were identified as homologs of *Sec23*, *Sar1*, and *Rab1* which are critical regulators of ER-to-Golgi transport (56, 58). Monitoring both Golgi outpost dynamics and dendritic branch extension showed a correlation between the presence of Golgi outposts at the dendritic branchpoints and dendritic branch extension (56). This study suggests that Golgi outposts may supply the necessary molecules for dendritic branch growth. Additional evidence suggests that Golgi outposts in the C4da neurons act as acentrosomal microtubule nucleation sites leading to the formation of microtubules (59). Additional studies in both *Drosophila* da neurons and *C. elegans* PVD neurons indicate that exocytosis also regulates dendrite expansion (60, 61). The *Drosophila* SM protein, Rop, acts together with the exocyst subunit, Sec6, to promote C4da dendrite growth (61). Endocytosis of cellular components from the plasma

membrane may also contribute to dendrite growth and branching. Loss-of-function of Shrub, a Snf7 homolog (a key component of the ESCRT-III complex), in C4da neurons caused a reduction in the dendritic field, but an overall increase in dendrite branching near the cell body (62). Together, these studies indicate that a combination of the secretory pathway, exocytosis, and endocytosis regulate dendrite morphogenesis.

Dendritic Field Organization and Patterning

While intrinsic factors regulate dendrite branch formation in individual neurons, there are additional mechanisms regulating the overall organization of the neuron's dendritic field and its interactions with dendrites from neighboring neurons. Dendrite self-avoidance (isoneuronal repulsion) and tiling (heteroneuronal repulsion) ensure an even distribution of sensory dendrites over the entire animal (1, 3). Additionally, neuron-substrate interactions regulate overall dendrite patterning by providing dendrites a suitable environment for growth (25, 63). Once the dendritic field is established, intracellular signaling pathways such as Hippo (discussed below) maintain dendritic field coverage (64). In many neurons such as the C4da neurons, the dendritic arbor expands in proportion with overall animal growth through a process called scaling (65). In this section, I will summarize each of these mechanisms regulating dendritic field organization and branching patterns.

Self-Avoidance, Tiling and Neuron-Substrate Interactions

During larval development, the dendritic fields of each class of da neuron are organized through several mechanisms. First, sister dendrites of the same neuron avoid one another (self-avoidance) (Figure 1.3A). However, dendrites of different classes of da neuron overlap with each other (coexistence). Self-avoidance occurs through alternative splicing of the Down syndrome cell adhesion molecule (DSCAM) locus (1). Splicing occurs randomly so that each neuron

expresses a different subset of isoforms of *Dscam1* (66). Dendrites of the same neuron exhibit contact-dependent repulsion due to the presence of the same *Dscam1* isoforms on the dendritic membrane (67). Loss of *Dscam1* function in all classes of da neurons caused self-avoidance defects with an increase in isoneuronal dendrite crossings (68). Expression of the same *Dscam1* isoform in different da neuron classes also prevented the overlap of their dendritic fields indicating that each da neuron class expresses a distinct isoform allowing the dendrites to normally overlap (68). The dendrites in *C. elegans* PVD neurons also exhibit contact-dependent self-avoidance in order to envelop the entire animal in sensory dendrites (12). A recent study has determined that the Wnt-secretory factor MIG-14/Wntless is required for dendrite self-avoidance in PVD neurons. MIG-14 promotes dendrite self-avoidance through interactions with the WASP complex which regulates F-actin assembly (69).

Additionally, dendrites of the same class of da neuron also avoid one another in a process called tiling (3). Both C3da and C4da neurons tile the larval epidermis to achieve uniform coverage of the entire animal (26). Tiling is established by homotypic dendrite-dendrite repulsion between dendrites of the same class of neuron (26, 65, 70) (Figure 1.3B). Two experiments demonstrated the importance of homotypic repulsion in establishing tiling. First, if a C4da neuron is ablated in early embryonic stages, then the neighboring C4da neurons will grow into its territory (26, 65, 70). Additionally, duplicated C4da neurons show very little overlap between dendrites of the duplicated neurons (26). Both self-avoidance and tiling ensure that the entire larval epidermis is completely and non-redundantly covered with C3da or C4da dendrites (23). Genetic studies have identified an intracellular signaling pathway important for tiling among C4da neurons. The intracellular STE20 family kinase, Hippo, activates Tricornered (Trc), a NDR kinase in C4da neurons. Trc and Furry (Fry) together prevent overlap between

neighboring dendrites (64, 71). Additional studies indicate that components of the TOR complex 2 (TORC2) genetically interact with and activate Trc to regulate dendritic tiling in C4da neurons (72).

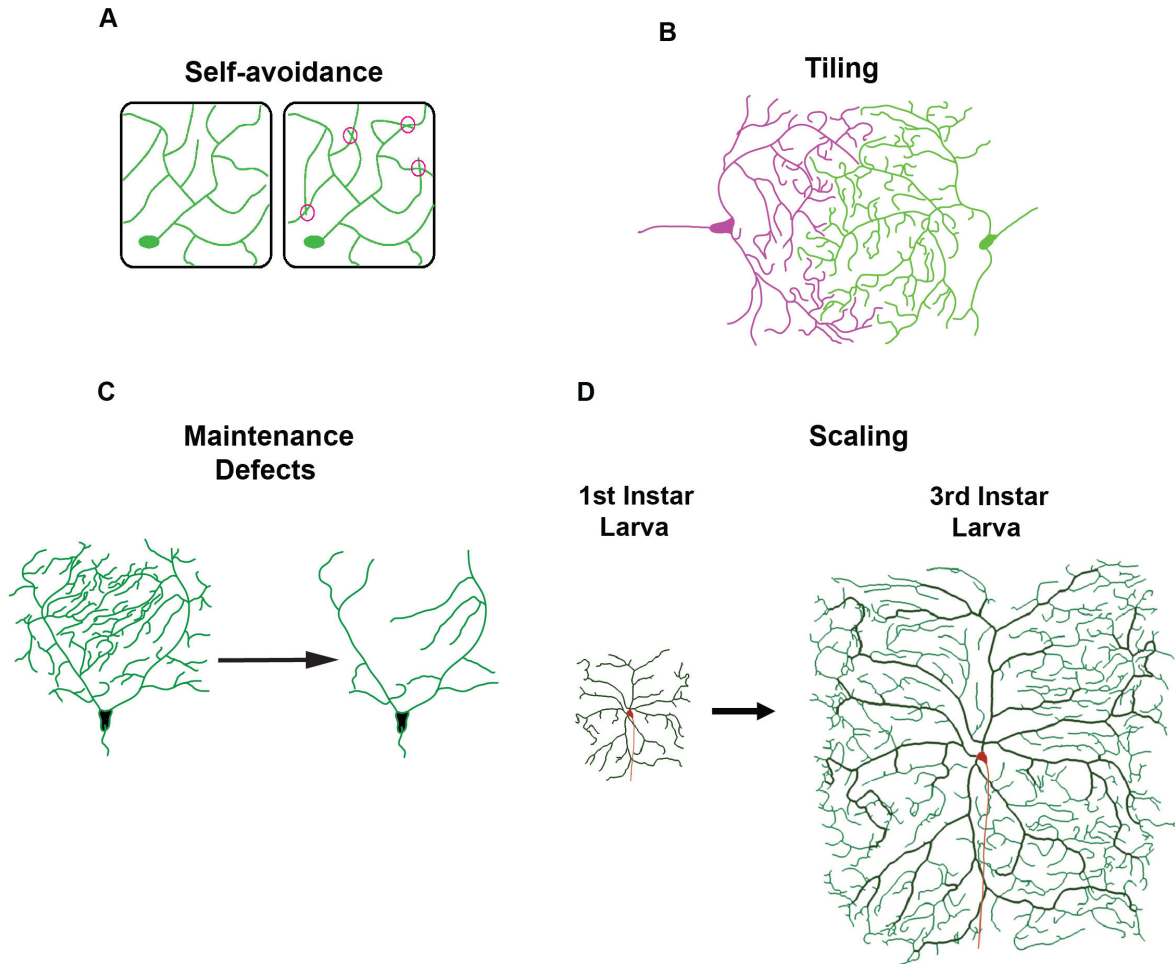


Figure 1.3. Dendrite Patterning and Field Organization.

General properties regulating dendritic field organization. (A) In the neuron on the left, the sister dendrites avoid one another. However, the neuron on the right has defects in dendrite self-avoidance resulting in crossing defects (red circles). Images in (A) are adapted from (1). (B) The purple and green neurons represent different C4da neurons. Dendrites of the same class of da neuron avoid one another in a process called tiling. (C) After establishment in their receptive field, dendritic arbors are maintained. Maintenance defects occur when dendritic branches are lost as the organism develops. (D) In first instar larvae, C4da neurons rapidly establish their receptive fields. As the animal grows in size, the C4da neuron extends many terminal dendrites to cover the newly available space in a process called scaling. Images in B, C, and D are adapted from prior drawings by Chun Han.

Analyses of neuron-substrate interactions demonstrate that C4da dendrites grow along the epidermis-derived extracellular matrix (ECM) and are confined to a 2-dimensional space between the epidermal basal surface and the ECM (25, 63). The neuronal integrins, *Mys* and *Mew*, are cell-autonomously required to attach C4da dendrites to the ECM. Integrin LOF in C4da neurons results in an increase in epidermal cell enclosure of dendrites resulting in increased noncontacting dendritic crossings. Genetic interaction analysis indicates that epidermal laminins likely act as ligands for neuronal integrins to regulate dendrite-ECM interactions (25). Interestingly, *trc* and *fry* mutants do not confine their dendrites to the 2D space resulting in noncontacting crossing defects. Forcing dendrite growth onto the ECM by overexpressing *Mys* and *Mew* in C4da neurons rescued the crossing defects in *fry* mutants (25). New analyses in C4da neurons demonstrate that mutations in the epidermis-derived ligand *sema-2b* cause dendrite detachment from the ECM. *Sema-2b* regulates dendrite-ECM adhesion by binding to the neuronal *PlexB* receptor. Additional genetic analysis indicates that the neuronal integrins, the TORC2 complex, and *Trc/Fry* signaling act downstream of *Sema-2b/PlexB* signaling to control dendrite-ECM adhesion and tiling (73).

Dendritic Field Maintenance & Growth-Promoting Pathways

Once established in their receptive field during development, dendritic arbors are actively maintained. In C4da neurons, the STE20 family kinase *Hippo* coordinates the tiling and maintenance of dendritic fields. In addition to *Hippo*'s roles in establishing tiling (discussed in the above section), *Hippo* acts together with the positive regulator *Salvador (Sav)* to activate the NDR kinase *Warts (Wts)* (64). Homozygous mutant C4da neurons for either *wts* or *sav* initially grow dendritic branches normally. However, as development proceeds, dendritic branches are lost resulting in large gaps in the dendritic field indicating that the branches are not maintained

(64) (Figure 1.3C). Additional studies have shown that Warts interacts with the Polycomb group (PcG) genes to promote dendritic maintenance through regulation of Hox gene expression in C4da neurons (74).

Overall dendritic field size is also regulated by cell growth-promoting pathways. Several studies in the *Drosophila* da neurons and in other systems indicate that the phosphoinositide 3-kinase (PI3K)-mTOR (mammalian target of rapamycin) signaling pathway controls dendritic growth (65, 75, 76). In hippocampal neurons, PI3K-mTOR signaling promotes the growth of dendrites and overall dendrite complexity (75, 76). In *Drosophila* da neurons, the PI3K-mTOR signaling pathway is necessary for C4da dendrite growth and overall scaling (discussed below) (65). Additional studies in C4da neurons demonstrate that components of the TORC1 (77) and TORC2 complexes are necessary for dendritic growth and tiling (72).

In many neuronal cell types, dendritic arbors develop in proportion with their receptive field in a process called scaling. This process ensures proper connectivity and sampling of sensory inputs in the receptive field. Dendrite scaling occurs in many neuronal cell types including *Drosophila* da neurons, retinal ganglion cells in goldfish, and mouse motoneurons (3). In C4da neurons, dendrite growth occurs in two phases over the course of larval development. First, the C4da neurons grow rapidly before 48 hours after egg laying (AEL) in order to establish their receptive fields (65). Later in larval development, as the animal grows in size, the C4da neurons grow at a similar rate as the larval body by extending dendritic branches to cover the newly developed receptive field. This later growth phase is referred to as scaling (Figure 1.3D) (65) and will be discussed in more detail later. The molecular mechanisms controlling dendrite scaling are only beginning to be understood.

Extrinsic Mechanisms Controlling Dendrite Development

Both intrinsic and extrinsic mechanisms are necessary for dendrite morphogenesis (1). As the above section demonstrates, intrinsic regulators of dendrite growth have been well studied in several model systems including *Drosophila* neurons. In the mammalian central nervous system, several secreted ligands and signaling pathways including Sema3A, Slit, and neurotrophins regulate axon and dendrite guidance in cortical pyramidal neurons (1). However, the mechanisms in which extracellular signals and the surrounding cellular environment influence dendrite development in the peripheral nervous system are not as well understood.

Perhaps one of the best studied examples of extracellular regulation of sensory dendrite branching is in the *C. elegans* PVD neurons. As mentioned previously, the 4° branches of the PVD neurons develop between the hypodermis and muscle tissues of the worm (4, 12). Early genetic studies have determined that two skin-derived adhesion molecules, MNR-1 and SAX-7, direct 4° branch growth through interactions with a neuronal receptor, DMA-1 (78). Additional studies have provided a more complete picture of how the 4° branches of the PVD neuron develop. Expression analysis using antibody staining demonstrates that SAX-7 forms regularly spaced stripes between the muscle and hypodermal cells. These stripes form before the 4° branches and are necessary for branch growth. The extracellular matrix protein, UNC-52/Perlecan, indirectly determines the SAX-7 pattern through the formation of hemidesmosomes in each hypodermal cell (79). More recent analysis of PVD dendrite branching has determined that an additional muscle-derived ligand, LECT-2, functions in a multi-protein complex with MNR-1 and SAX-7 to activate DMA-1 (80). DMA-1 then interacts synergistically with the claudin-like membrane protein HPO-30 to recruit the actin regulators, TIAM-1 and WRC (WAVE regulatory complex). These cooperative interactions drive actin polymerization leading to high-order dendrite branch formation (81).

In zebrafish larvae, the Rohon-Beard (RB) neurons elaborate sensory axons that innervate the skin (9). Genetic studies have determined that the leukocyte antigen-related (LAR) family of receptor protein tyrosine phosphatases are expressed in RB neurons and are required for sensory axon innervation of the skin. Knockdown of LAR in RB neurons caused skin innervation defects with axons improperly arborizing below the skin (14). To determine the possible signaling pathways important for sensory axon innervation, the authors looked at heparan sulfate proteoglycans (HSPGs). HSPGs act as ligands for LAR in the *Drosophila* neuromuscular junction (NMJ) (82) and in cultured dorsal root ganglion cells (83). Similar skin innervation defects were seen in *dackel* mutants in which HS biosynthesis is altered. Additionally, peripheral axons avoided areas of the skin injected with heparinase III, an enzyme that degrades heparan sulfate, which suggests that HSPGs act as attractants for sensory axons. Genetic interactions between *dackel* and LAR indicated that both genes act in the same genetic pathway to regulate sensory axon guidance to the skin (14). This study suggests that extracellular HSPGs guide sensory axons to the skin by interacting with LAR receptors in the RB neuron.

Although the intrinsic regulators of dendrite branching patterns in *Drosophila* da neurons have been well studied, less is known about how the extracellular microenvironment influences dendrite growth. Several extracellular molecules known to regulate axonal guidance in mammalian cortical pyramidal neurons also regulate *Drosophila* da dendrite branching. For example, dendrite targeting in C3da neurons relies on Netrin-Frazzled signaling. NetrinB is normally secreted by the nearby lateral chordotonal organ cap cells and acts as an attractive signal to direct C3da dendrite growth to this region. Localized mis-expression of NetrinB in the larval oenocytes shifted dendrite growth to these cells. This directed dendrite growth was dependent on Frazzled receptor functioning in the C3da neurons (84). Additionally, the

membrane receptor Robo and its ligand Slit regulate C4da dendrite branching and elongation. In C4da neurons, loss of Robo or Slit caused reductions in the number of higher order dendritic branches (85). However, the molecular mechanisms in which Robo-Slit signaling regulate C4da dendrite branching are still unknown.

A recent RNAi screen of cell surface receptors in C4da neurons identified a receptor tyrosine kinase (RTK), Ret, as necessary for dendrite growth and dendrite-ECM adhesion (86). Loss of Ret function in C4da neurons resulted in an increase in dendrite crossings due to detachment from the ECM. Additional analysis determined that Ret interacts with neuronal integrins to regulate dendrite-ECM adhesion likely through the activity of the Rho family GTPase, Rac1. Interestingly, Ret-mediated regulation of dendrite growth and stabilization occurs independently of integrin and Rac1, suggesting that additional unknown extracellular ligands are responsible (86). Recent evidence indicates that the epidermal-cell derived TGF- β ligand, Maverick (87), promotes C4da dendrite growth and patterning through the Ret receptor. Local changes in Mav expression levels direct C4da dendrite growth to regions with higher Mav availability (88).

Coordination of Larval Body-Organ Growth

Both intrinsic and extrinsic mechanisms must integrate to regulate dendrite morphogenesis in coordination with the growth of the rest of the body. As mentioned earlier, C4da dendrites scale with the rest of the larval body. As the animal develops rapidly in later larval developmental stages, C4da neurons grow terminal dendrites to fill in the receptive field. This process requires a coordination between the epidermal cell and neuronal growth-promoting pathways. Epidermal cells ensure proper dendritic scaling by expressing the microRNA *bantam*. *bantam* mutant animals display severe dendrite overgrowth phenotypes starting at 72 hrs AEL.

Genetic interactions studies found that *bantam* inhibits the neuronal PI3K-mTOR kinase pathway which thereby inhibits dendrite growth at later stages of larval development (65). More recent analysis of *bantam* functioning have found that the microRNA regulates epithelial endoreplication leading to changes in dendrite-extracellular matrix and dendrite-epithelium contacts. Reductions in epithelial endoreplication caused a decrease in the expression of the epidermal cell adhesion molecule, Mys, thereby altering the cell's adhesive properties. These changes then lead to alterations in dendrite-substrate contacts which would normally restrict dendrite growth at later developmental stages (89). These studies indicate that neurons and non-neural tissues coordinate under a given external growth condition. However, how the coordination of neuron/non-neural tissues is influenced by growth conditions including the nutrient environment are not as well understood.

Some insight into neuron/non-neural tissue growth coordination under nutrient stress can be gleaned from the phenomenon of brain sparing in *Drosophila* larvae. If *Drosophila* larvae are raised in nutrient restricted conditions after reaching critical weight, larval body growth is inhibited so that animal size is half its normal size. However, cells in the central nervous system (CNS) grow preferentially and are spared under nutrient stress. This organ sparing occurs through the activity of the receptor tyrosine kinase anaplastic lymphoma kinase (Alk). Alk activity in neural stem cells (neuroblasts) protects the cells from reductions in amino acids and insulin-like peptides (IIs) under nutrient restriction. Alk acts as an alternative signal to activate PI3-kinase and thereby promote growth of neuroblast lineages (90). However, it is not known if this mechanism occurs in other neuronal cell types in the PNS.

Tissue-specific Gene Manipulation in *Drosophila*

The ability to study dendrite morphogenesis *in vivo* relies on tissue-specific gene manipulation. Traditional techniques for performing tissue-specific gene loss-of-function (LOF) in *Drosophila* rely on the Gal4/UAS/Gal80 system and FLP/FRT-mediated mitotic recombination system. In the Gal4/UAS/Gal80 system, the Gal4 transcription factor binds the upstream activator sequence (UAS) to drive expression of a gene's coding-sequence. Gal4 activity is also temperature-sensitive which provides further temporal control over gene expression. Additionally, when Gal80 is present, it inhibits the activity of the Gal4 thereby blocking UAS expression (91) and Gal4 activity can be further regulated using a temperature-sensitive Gal80 (92). In the FLP/FRT system, the heat-inducible recombinase flippase (FLP) drives mitotic recombination at specific target FRT sites in the genome (93).

Conventional mosaic analysis in *Drosophila* generates homozygous mutant cells in heterozygous animals through FLP/FRT-mediated mitotic recombination. These mutant clones are generated randomly in the animal through heat-shock induction (94). Combining the Gal4/UAS/Gal80 system and FLP/FRT system allows for the generation of homozygous mutant cells in a tissue-specific and temporally-restricted manner (95). Mosaic analysis with repressible cell marker (MARCM) (31) expands upon these previous mosaic techniques to label homozygous mutant cells with a fluorescent reporter (Figure 1.4A). In this system, a tissue-specific Gal4 drives UAS-GFP expression (or some other fluorescent reporter) to label homozygous mutant daughter cells. A ubiquitously expressed Gal80 transgene is placed distal to a FRT site. Cells are initially heterozygous for a LOF mutation in a gene of interest which is located on the same chromosome arm as a second FRT site. The second FRT site is also located in *trans* to the chromosome arm containing the Gal80 transgene. After FLP/FRT-mediated recombination, Gal80 is removed from one of the daughter cells which allows Gal4-driven

reporter expression in the homozygous mutant daughter cell (31). Additional techniques such as twin-spot MARCM use reporter-specific silencers to differentially label each daughter cell which allows for lineage tracing analysis of cells in the mushroom body (96). While mosaic analyses are powerful techniques for generating a reliable gene LOF in a tissue-specific manner, there are several potential limitations. First, these techniques require preexisting mutations for a gene of interest on the same chromosome arm as a FRT site. Second, MARCM requires extensive, often laborious screening for labeled clones in the animal which can hamper large LOF screens. Additionally, multiple genetic components including Gal4/UAS/Gal80, FLP/FRT, and a LOF mutation are required in the same animal. Furthermore, MARCM cannot be used easily to study multiple genes located on different chromosome arms.

An easier method of tissue-specific gene silencing in *Drosophila* occurs through RNA interference (RNAi) (Figure 1.4B). RNAi uses the Gal4/UAS system to drive the expression of UAS-dsRNA or UAS-shRNA for a gene of interest with a tissue-specific Gal4 driver. This results in degradation of the gene's mRNA through the RISC complex (97). While this technique provides a powerful approach for conducting LOF screens in *Drosophila* (98, 99), there are several disadvantages. First, because the gene of interest is still present in the genome, RNAi often does not cause a complete knockdown of the gene's mRNA (98). Additionally, RNAi is prone to off-target effects which may complicate any potential conclusions regarding a gene's functioning (100).

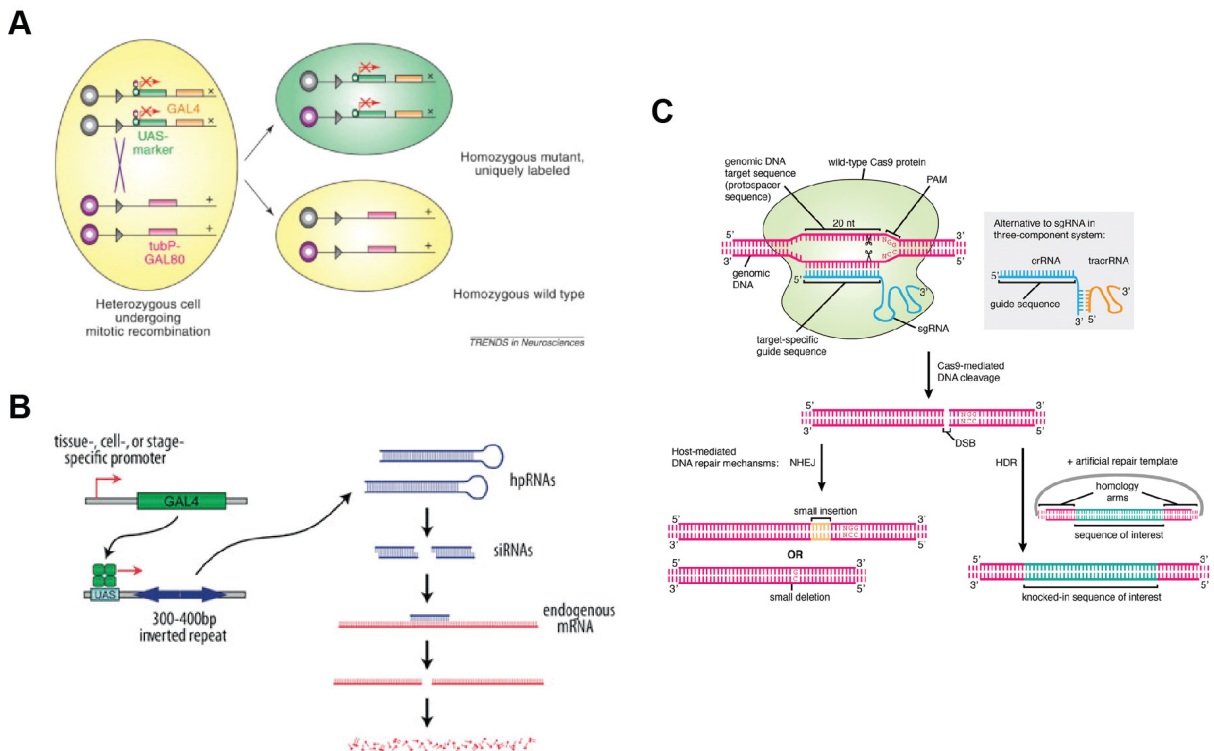


Figure 1.4. Tissue-specific Gene Manipulation in *Drosophila*.

(A) Diagram illustrating how mosaic analysis with a repressible cell marker (MARCM) generates marked homozygous mutant cells. See text for complete description of the various genetic components. Image was adapted from (31). (B) Diagram illustrating the components of tissue-specific RNA Interference (RNAi). See text for complete description. Image was adapted from the VDRC website (https://stockcenter.vdrc.at/control/library_rnai). (C) Diagram illustrating how the type II clustered regularly interspaced short palindromic repeats (CRISPR)/CRISPR-associated protein (Cas9) system generates sequence-specific double-strand breaks (DSBs). Briefly, the Cas9-induced DSBs are repaired by the host through either non-homologous end-joining (NHEJ) or homology-directed repair (HDR). See text for complete description of the individual components. Image was adapted from (101).

Because of these limitations, the type II clustered regularly interspaced short palindromic repeats (CRISPR)/CRISPR-associated protein (Cas9) system (102) has the potential to provide a simpler, more efficient tissue-specific LOF strategy due to the ease in generating targeted mutations. This system uses the bacterial RNA-guided Cas9 endonuclease to induce double-strand breaks (DSBs) at specific gene targeting sites. The targeting sites are determined by a chimeric guide RNA (gRNA) which recognizes a 20-nt targeting sequence next to a trinucleotide proto-spacer adjacent (PAM) sequence (102). The Cas9-mediated DSBs are then repaired by the host through either non-homologous end-joining (NHEJ) or homology-directed repair (HDR). Errors in the NHEJ repair process can result in either small insertion-deletions (indels) at the targeting site (103) or a deletion between two targeting sites (104, 105) (Figure 1.4C).

CRISPR/Cas9 was initially used in *Drosophila* to create heritable mutations through microinjections of DNA plasmids or in vitro-transcribed mRNA for both Cas9 and gRNAs into fertilized embryos (103, 106, 107). An additional study has improved on these initial approaches by generating germline mutations for the *white* gene locus using transgenic flies expressing the germline-specific *nanos*-promoter-driven Cas9 and ubiquitously-expressed (U6-promoter-driven) gRNAs. This approach achieved a higher germline mutation frequency than the initial methods (104). Other studies have achieved variable germline mutation rates by injecting gRNAs into transgenic flies expressing germline-specific *nanos*-promoter-driven Cas9 (105) or *vasa*-promoter-driven Cas9 (108). Despite these initial successes, the rate of mutagenesis has been highly variable between different studies and between different genes.

One way to improve CRISPR/Cas9-mediated gene editing in the *Drosophila* genome is to optimize several parameters controlling the expression level and efficiency of transgenic gRNAs. A previous study in *Drosophila* (109) has determined that the ubiquitously expressed U6:3

promoter-driven gRNA results in the highest frequency of somatic and germline gene mutations when compared to other U6 promoter-driven gRNAs. Additionally, combining the U6:1 and U6:3 promoters allows for simultaneous expression of two gRNAs (109). An analysis of gRNA target sequence length determined that gRNAs have an optimum targeting sequence length of 18-20 nucleotides. This study also determined that a higher GC content in the most proximal nucleotides to the PAM sequence results in a higher mutation rate (110). In order to maximize the gene targeting ability of the CRISPR/Cas9 system, studies in both *Drosophila* and rice have used the tRNA processing system to produce multiple gRNAs from a single construct (111, 112). This method uses tandem repeats of tRNA and gRNA sequences under the control of the RNA Polymerase III promoter. Endogenous RNases then recognize the tRNA structure and cleave the 5' and 3' ends which releases multiple individual gRNAs from the same transgene. Using this approach, LOF mutations can be generated in multiple genes in rice (111). This method has also been used successfully in *Drosophila* to produce multiple gRNAs from a single transcript resulting in heritable LOF mutations of multiple genes (112).

CRISPR/Cas9 has also been used to more precisely edit genes in the *Drosophila* genome using homology-directed repair (HDR) to introduce exogenous gene sequences (105, 109, 113). Using this approach, specific gene sequence changes can be introduced into a gene of interest which allows greater control over the type of LOF mutation (109). HDR can also be used to insert fluorescent markers into the coding region of a gene which can elucidate a gene's endogenous expression pattern (109). Additionally, HDR can be used to generate null alleles for developmentally essential genes (110) and to insert FRT sites into a gene (113). Modifications to the Cas9 endonuclease provide additional ways in which CRISPR/Cas9 can be used to investigate gene functioning. Several studies have used a catalytically dead version of Cas9

(dCas9) to recruit transcription activators and repressors (114, 115). CRISPR transcriptional activators (CRISPRa) recruit the transcriptional activation machinery to target genes using dCas9 fused to a tripartite activator domain (VPR). This approach effectively generates gain of function phenotypes at physiologically relevant expression levels (115). In a complementary manner, CRISPR interference (CRISPRi) uses dCas9 fused to a transcriptional repressor KRAB domain to inhibit transcription initiation at target genes (114).

Tissue-specific mutagenesis of genes in *Drosophila* has been accomplished by combining the CRISPR/Cas9 system with the Gal4/UAS system (109, 112, 116). In this system, tissue-specific Gal4 drives *UAS-Cas9* expression while gRNAs are expressed ubiquitously (109, 116) or expressed by UAS (112). This system of Gal4-driven Cas9 mutagenesis has been used successfully to investigate gene functioning in a variety of somatic tissues including the cuticle, wing imaginal discs, ovaries, and testes (109, 112, 116). However, Gal4-driven Cas9 has several potential disadvantages for studying gene functioning during dendrite morphogenesis. First, the Gal4 transcription step will delay Cas9 expression in the cell which will make it difficult to study early-acting genes. Second, the Gal4/UAS system can result in excessive levels of Cas9 protein in the cell which can be toxic (117). Toxic levels of Cas9 protein may then interfere with normal cell development. Finally, using Gal4-driven Cas9 restricts the use of the Gal4/UAS system which offers less genetic flexibility in the same animal. Therefore, a simpler and more robust tissue-specific gene mutagenesis approach is necessary to study dendrite morphogenesis in *Drosophila*.

Dissertation Outline

In Chapter 2, I describe work done to examine the extracellular regulation of dendrite growth in the C4da neurons. We determined that the epidermal cell-derived heparan sulfate

proteoglycans (HSPGs), Dally and Sdc, act redundantly as a permissive signal for dendrite growth. Through a novel long-term time-lapse imaging approach, we determined that HSPGs are required for terminal dendrite stabilization by promoting microtubule stabilization. Finally, we determined that the receptor protein tyrosine phosphatase, Ptp69D, is required for C4da dendrite growth in a parallel pathway to HSPGs.

In Chapter 3, I describe the development and optimization of CRISPR-mediated tissue-restricted mutagenesis (CRISPR-TRiM). This method utilizes a transgenic Cas9 driven by a tissue-specific enhancer which allows for targeted gene deletions. We developed tools to make and evaluate enhancer-driven Cas9 lines to determine tissue specificity and gene knockout efficiency. Additionally, we evaluated several multi-gRNA designs and determined that one design is more effective in generating gene knockouts. Using C4da neurons as a model system, we demonstrate that CRISPR-TRiM can effectively knockout multiple redundantly acting genes.

In Chapter 4, I describe preliminary work done to examine the relationship between overall animal growth and C4da dendrite growth under nutrient deprivation. We determined that C4da neurons grow preferentially compared to larval epidermal cells in low yeast conditions. The C4da neurons also exhibit a preferential suppression of autophagy under nutrient deprivation. Finally, we determined that activity of the transcription factor, FoxO, underlies the differential growth of neurons and epidermal cells. FoxO acts in epidermal cells to inhibit cell growth under nutrient stress while slightly promoting dendrite growth.

REFERENCES

1. Dong X, Shen K, & Bulow HE (2015) Intrinsic and extrinsic mechanisms of dendritic morphogenesis. *Annu Rev Physiol* 77:271-300.
2. Kulkarni VA & Firestein BL (2012) The dendritic tree and brain disorders. *Mol Cell Neurosci* 50(1):10-20.
3. Jan YN & Jan LY (2010) Branching out: mechanisms of dendritic arborization. *Nat Rev Neurosci* 11(5):316-328.

4. Albeg A, *et al.* (2011) *C. elegans* multi-dendritic sensory neurons: morphology and function. *Mol Cell Neurosci* 46(1):308-317.
5. Hall DH & Treinin M (2011) How does morphology relate to function in sensory arbors? *Trends Neurosci* 34(9):443-451.
6. Lin B, Wang SW, & Masland RH (2004) Retinal ganglion cell type, size, and spacing can be specified independent of homotypic dendritic contacts. *Neuron* 43(4):475-485.
7. Sanes JR & Zipursky SL (2010) Design principles of insect and vertebrate visual systems. *Neuron* 66(1):15-36.
8. Palanca AM, *et al.* (2013) New transgenic reporters identify somatosensory neuron subtypes in larval zebrafish. *Dev Neurobiol* 73(2):152-167.
9. Wang F, Julien DP, & Sagasti A (2013) Journey to the skin: Somatosensory peripheral axon guidance and morphogenesis. *Cell Adh Migr* 7(4):388-394.
10. Marin-Padilla M (2014) The mammalian neocortex new pyramidal neuron: a new conception. *Front Neuroanat* 7:51.
11. Valnegri P, Puram SV, & Bonni A (2015) Regulation of dendrite morphogenesis by extrinsic cues. *Trends Neurosci* 38(7):439-447.
12. Smith CJ, *et al.* (2010) Time-lapse imaging and cell-specific expression profiling reveal dynamic branching and molecular determinants of a multi-dendritic nociceptor in *C. elegans*. *Dev Biol* 345(1):18-33.
13. Sagasti A, Guido MR, Raible DW, & Schier AF (2005) Repulsive interactions shape the morphologies and functional arrangement of zebrafish peripheral sensory arbors. *Curr Biol* 15(9):804-814.
14. Wang F, Wolfson SN, Gharib A, & Sagasti A (2012) LAR receptor tyrosine phosphatases and HSPGs guide peripheral sensory axons to the skin. *Curr Biol* 22(5):373-382.
15. Timme-Laragy AR, Karchner SI, & Hahn ME (2012) Gene knockdown by morpholino-modified oligonucleotides in the zebrafish (*Danio rerio*) model: applications for developmental toxicology. *Methods Mol Biol* 889:51-71.
16. Choi JH, Law MY, Chien CB, Link BA, & Wong RO (2010) In vivo development of dendritic orientation in wild-type and mislocalized retinal ganglion cells. *Neural Dev* 5:29.
17. Walsh MK & Quigley HA (2008) In vivo time-lapse fluorescence imaging of individual retinal ganglion cells in mice. *J Neurosci Methods* 169(1):214-221.
18. Mumm JS, *et al.* (2006) In vivo imaging reveals dendritic targeting of laminated afferents by zebrafish retinal ganglion cells. *Neuron* 52(4):609-621.
19. Duan X, Krishnaswamy A, De la Huerta I, & Sanes JR (2014) Type II cadherins guide assembly of a direction-selective retinal circuit. *Cell* 158(4):793-807.
20. Kim IJ, Zhang Y, Meister M, & Sanes JR (2010) Laminar restriction of retinal ganglion cell dendrites and axons: subtype-specific developmental patterns revealed with transgenic markers. *J Neurosci* 30(4):1452-1462.
21. Yamagata M & Sanes JR (2008) Dscam and Sidekick proteins direct lamina-specific synaptic connections in vertebrate retina. *Nature* 451(7177):465-469.
22. Matsuoka RL, *et al.* (2011) Transmembrane semaphorin signalling controls laminar stratification in the mammalian retina. *Nature* 470(7333):259-263.
23. Grueber WB, Jan LY, & Jan YN (2002) Tiling of the *Drosophila* epidermis by multidendritic sensory neurons. *Development* 129(12):2867-2878.

24. Han C, Jan LY, & Jan YN (2011) Enhancer-driven membrane markers for analysis of nonautonomous mechanisms reveal neuron-glia interactions in *Drosophila*. *Proc Natl Acad Sci U S A* 108(23):9673-9678.
25. Han C, *et al.* (2012) Integrins regulate repulsion-mediated dendritic patterning of *Drosophila* sensory neurons by restricting dendrites in a 2D space. *Neuron* 73(1):64-78.
26. Grueber WB, Ye B, Moore AW, Jan LY, & Jan YN (2003) Dendrites of distinct classes of *Drosophila* sensory neurons show different capacities for homotypic repulsion. *Curr Biol* 13(8):618-626.
27. Hwang RY, *et al.* (2007) Nociceptive neurons protect *Drosophila* larvae from parasitoid wasps. *Curr Biol* 17(24):2105-2116.
28. Tsubouchi A, Caldwell JC, & Tracey WD (2012) Dendritic filopodia, Ripped Pocket, NOMPC, and NMDARs contribute to the sense of touch in *Drosophila* larvae. *Curr Biol* 22(22):2124-2134.
29. Xiang Y, *et al.* (2010) Light-avoidance-mediating photoreceptors tile the *Drosophila* larval body wall. *Nature* 468(7326):921-926.
30. Yan Z, *et al.* (2013) *Drosophila* NOMPC is a mechanotransduction channel subunit for gentle-touch sensation. *Nature* 493(7431):221-225.
31. Lee T & Luo L (2001) Mosaic analysis with a repressible cell marker (MARCM) for *Drosophila* neural development. *Trends Neurosci* 24(5):251-254.
32. Spruston N (2008) Pyramidal neurons: dendritic structure and synaptic integration. *Nat Rev Neurosci* 9(3):206-221.
33. Arikath J (2012) Molecular mechanisms of dendrite morphogenesis. *Front Cell Neurosci* 6:61.
34. Graves AR, *et al.* (2012) Hippocampal pyramidal neurons comprise two distinct cell types that are countermodulated by metabotropic receptors. *Neuron* 76(4):776-789.
35. Leone DP, Srinivasan K, Chen B, Alcamo E, & McConnell SK (2008) The determination of projection neuron identity in the developing cerebral cortex. *Curr Opin Neurobiol* 18(1):28-35.
36. Whitford KL, *et al.* (2002) Regulation of cortical dendrite development by Slit-Robo interactions. *Neuron* 33(1):47-61.
37. Polleux F, Morrow T, & Ghosh A (2000) Semaphorin 3A is a chemoattractant for cortical apical dendrites. *Nature* 404(6778):567-573.
38. Sugimura K, Satoh D, Estes P, Crews S, & Uemura T (2004) Development of morphological diversity of dendrites in *Drosophila* by the BTB-zinc finger protein abrupt. *Neuron* 43(6):809-822.
39. Li W, Wang F, Menut L, & Gao FB (2004) BTB/POZ-zinc finger protein abrupt suppresses dendritic branching in a neuronal subtype-specific and dosage-dependent manner. *Neuron* 43(6):823-834.
40. Blochlinger K, Bodmer R, Jan LY, & Jan YN (1990) Patterns of expression of cut, a protein required for external sensory organ development in wild-type and cut mutant *Drosophila* embryos. *Genes Dev* 4(8):1322-1331.
41. Grueber WB, Jan LY, & Jan YN (2003) Different levels of the homeodomain protein cut regulate distinct dendrite branching patterns of *Drosophila* multidendritic neurons. *Cell* 112(6):805-818.

42. Li N, Zhao CT, Wang Y, & Yuan XB (2010) The transcription factor Cux1 regulates dendritic morphology of cortical pyramidal neurons. *PLoS One* 5(5):e10596.
43. Cubelos B, *et al.* (2010) Cux1 and Cux2 Regulate Dendritic Branching, Spine Morphology, and Synapses of the Upper Layer Neurons of the Cortex. *Neuron* 66(4):523-535.
44. Crozatier M & Vincent A (2008) Control of multidendritic neuron differentiation in Drosophila: the role of Collier. *Dev Biol* 315(1):232-242.
45. Hattori Y, Sugimura K, & Uemura T (2007) Selective expression of Knot/Collier, a transcriptional regulator of the EBF/Olf-1 family, endows the Drosophila sensory system with neuronal class-specific elaborated dendritic patterns. *Genes Cells* 12(9):1011-1022.
46. Jinushi-Nakao S, *et al.* (2007) Knot/Collier and cut control different aspects of dendrite cytoskeleton and synergize to define final arbor shape. *Neuron* 56(6):963-978.
47. Kim MD, Jan LY, & Jan YN (2006) The bHLH-PAS protein Spineless is necessary for the diversification of dendrite morphology of Drosophila dendritic arborization neurons. *Genes Dev* 20(20):2806-2819.
48. Lee A, *et al.* (2003) Control of dendritic development by the Drosophila fragile X-related gene involves the small GTPase Rac1. *Development* 130(22):5543-5552.
49. Li W & Gao FB (2003) Actin filament-stabilizing protein tropomyosin regulates the size of dendritic fields. *J Neurosci* 23(15):6171-6175.
50. Ferreira T, Ou Y, Li S, Giniger E, & van Meyel DJ (2014) Dendrite architecture organized by transcriptional control of the F-actin nucleator Spire. *Development* 141(3):650-660.
51. Stewart A, Tsubouchi A, Rolls MM, Tracey WD, & Sherwood NT (2012) Katanin p60-like1 promotes microtubule growth and terminal dendrite stability in the larval class IV sensory neurons of Drosophila. *J Neurosci* 32(34):11631-11642.
52. Ori-McKenney KM, *et al.* (2016) Phosphorylation of beta-Tubulin by the Down Syndrome Kinase, Minibrain/DYRK1a, Regulates Microtubule Dynamics and Dendrite Morphogenesis. *Neuron* 90(3):551-563.
53. Satoh D, *et al.* (2008) Spatial control of branching within dendritic arbors by dynein-dependent transport of Rab5-endosomes. *Nat Cell Biol* 10(10):1164-1171.
54. Zheng Y, *et al.* (2008) Dynein is required for polarized dendritic transport and uniform microtubule orientation in axons. *Nat Cell Biol* 10(10):1172-1180.
55. Arthur AL, Yang SZ, Abellaneda AM, & Wildonger J (2015) Dendrite arborization requires the dynein cofactor NudE. *J Cell Sci* 128(11):2191-2201.
56. Ye B, *et al.* (2007) Growing dendrites and axons differ in their reliance on the secretory pathway. *Cell* 130(4):717-729.
57. Horton AC, *et al.* (2005) Polarized secretory trafficking directs cargo for asymmetric dendrite growth and morphogenesis. *Neuron* 48(5):757-771.
58. Lee MC, Miller EA, Goldberg J, Orci L, & Schekman R (2004) Bi-directional protein transport between the ER and Golgi. *Annu Rev Cell Dev Biol* 20:87-123.
59. Ori-McKenney KM, Jan LY, & Jan YN (2012) Golgi outposts shape dendrite morphology by functioning as sites of acentrosomal microtubule nucleation in neurons. *Neuron* 76(5):921-930.
60. Taylor CA, Yan J, Howell AS, Dong X, & Shen K (2015) RAB-10 Regulates Dendritic Branching by Balancing Dendritic Transport. *PLoS Genet* 11(12):e1005695.

61. Peng Y, *et al.* (2015) Regulation of dendrite growth and maintenance by exocytosis. *J Cell Sci* 128(23):4279-4292.
62. Sweeney NT, Brenman JE, Jan YN, & Gao FB (2006) The coiled-coil protein shrub controls neuronal morphogenesis in *Drosophila*. *Curr Biol* 16(10):1006-1011.
63. Kim ME, Shrestha BR, Blazeski R, Mason CA, & Grueber WB (2012) Integrins establish dendrite-substrate relationships that promote dendritic self-avoidance and patterning in *drosophila* sensory neurons. *Neuron* 73(1):79-91.
64. Emoto K, Parrish JZ, Jan LY, & Jan YN (2006) The tumour suppressor Hippo acts with the NDR kinases in dendritic tiling and maintenance. *Nature* 443(7108):210-213.
65. Parrish JZ, Xu P, Kim CC, Jan LY, & Jan YN (2009) The microRNA bantam functions in epithelial cells to regulate scaling growth of dendrite arbors in *drosophila* sensory neurons. *Neuron* 63(6):788-802.
66. Miura SK, Martins A, Zhang KX, Graveley BR, & Zipursky SL (2013) Probabilistic splicing of *Dscam1* establishes identity at the level of single neurons. *Cell* 155(5):1166-1177.
67. Matthews BJ, *et al.* (2007) Dendrite self-avoidance is controlled by *Dscam*. *Cell* 129(3):593-604.
68. Soba P, *et al.* (2007) *Drosophila* sensory neurons require *Dscam* for dendritic self-avoidance and proper dendritic field organization. *Neuron* 54(3):403-416.
69. Liao CP, Li H, Lee HH, Chien CT, & Pan CL (2018) Cell-Autonomous Regulation of Dendrite Self-Avoidance by the Wnt Secretory Factor MIG-14/Wntless. *Neuron* 98(2):320-334 e326.
70. Sugimura K, *et al.* (2003) Distinct developmental modes and lesion-induced reactions of dendrites of two classes of *Drosophila* sensory neurons. *J Neurosci* 23(9):3752-3760.
71. Emoto K, *et al.* (2004) Control of dendritic branching and tiling by the Tricornered-kinase/Furry signaling pathway in *Drosophila* sensory neurons. *Cell* 119(2):245-256.
72. Koike-Kumagai M, Yasunaga K, Morikawa R, Kanamori T, & Emoto K (2009) The target of rapamycin complex 2 controls dendritic tiling of *Drosophila* sensory neurons through the Tricornered kinase signalling pathway. *EMBO J* 28(24):3879-3892.
73. Meltzer S, *et al.* (2016) Epidermis-Derived Semaphorin Promotes Dendrite Self-Avoidance by Regulating Dendrite-Substrate Adhesion in *Drosophila* Sensory Neurons. *Neuron* 89(4):741-755.
74. Parrish JZ, Emoto K, Jan LY, & Jan YN (2007) Polycomb genes interact with the tumor suppressor genes *hippo* and *warts* in the maintenance of *Drosophila* sensory neuron dendrites. *Genes Dev* 21(8):956-972.
75. Kumar V, Zhang MX, Swank MW, Kunz J, & Wu GY (2005) Regulation of dendritic morphogenesis by Ras-PI3K-Akt-mTOR and Ras-MAPK signaling pathways. *J Neurosci* 25(49):11288-11299.
76. Jaworski J, Spangler S, Seeburg DP, Hoogenraad CC, & Sheng M (2005) Control of dendritic arborization by the phosphoinositide-3'-kinase-Akt-mammalian target of rapamycin pathway. *J Neurosci* 25(49):11300-11312.
77. Lin WY, *et al.* (2015) The SLC36 transporter Pathetic is required for extreme dendrite growth in *Drosophila* sensory neurons. *Genes Dev* 29(11):1120-1135.
78. Salzberg Y, *et al.* (2013) Skin-derived cues control arborization of sensory dendrites in *Caenorhabditis elegans*. *Cell* 155(2):308-320.

79. Liang X, Dong X, Moerman DG, Shen K, & Wang X (2015) Sarcomeres Pattern Proprioceptive Sensory Dendritic Endings through UNC-52/Perlecan in *C. elegans*. *Dev Cell* 33(4):388-400.
80. Zou W, *et al.* (2016) A multi-protein receptor-ligand complex underlies combinatorial dendrite guidance choices in *C. elegans*. *Elife* 5.
81. Zou W, *et al.* (2018) A Dendritic Guidance Receptor Complex Brings Together Distinct Actin Regulators to Drive Efficient F-Actin Assembly and Branching. *Dev Cell* 45(3):362-375 e363.
82. Johnson KG, *et al.* (2006) The HSPGs Syndecan and Dallylike bind the receptor phosphatase LAR and exert distinct effects on synaptic development. *Neuron* 49(4):517-531.
83. Coles CH, *et al.* (2011) Proteoglycan-specific molecular switch for RPTPsigma clustering and neuronal extension. *Science* 332(6028):484-488.
84. Matthews BJ & Grueber WB (2011) Dscam1-mediated self-avoidance counters netrin-dependent targeting of dendrites in *Drosophila*. *Curr Biol* 21(17):1480-1487.
85. Dimitrova S, Reissaus A, & Tavosanis G (2008) Slit and Robo regulate dendrite branching and elongation of space-filling neurons in *Drosophila*. *Dev Biol* 324(1):18-30.
86. Soba P, *et al.* (2015) The Ret receptor regulates sensory neuron dendrite growth and integrin mediated adhesion. *Elife* 4.
87. Mavor LM, *et al.* (2016) Rab8 directs furrow ingression and membrane addition during epithelial formation in *Drosophila melanogaster*. *Development* 143(5):892-903.
88. Hoyer N, *et al.* (2018) Ret and Substrate-Derived TGF-beta Maverick Regulate Space-Filling Dendrite Growth in *Drosophila* Sensory Neurons. *Cell Rep* 24(9):2261-2272 e2265.
89. Jiang N, Soba P, Parker E, Kim CC, & Parrish JZ (2014) The microRNA bantam regulates a developmental transition in epithelial cells that restricts sensory dendrite growth. *Development* 141(13):2657-2668.
90. Cheng LY, *et al.* (2011) Anaplastic lymphoma kinase spares organ growth during nutrient restriction in *Drosophila*. *Cell* 146(3):435-447.
91. Duffy JB (2002) GAL4 system in *Drosophila*: a fly geneticist's Swiss army knife. *Genesis* 34(1-2):1-15.
92. McGuire SE, Mao Z, & Davis RL (2004) Spatiotemporal gene expression targeting with the TARGET and gene-switch systems in *Drosophila*. *Sci STKE* 2004(220):pl6.
93. Golic KG & Lindquist S (1989) The FLP recombinase of yeast catalyzes site-specific recombination in the *Drosophila* genome. *Cell* 59(3):499-509.
94. Xu T & Rubin GM (1993) Analysis of genetic mosaics in developing and adult *Drosophila* tissues. *Development* 117(4):1223-1237.
95. Duffy JB, Harrison DA, & Perrimon N (1998) Identifying loci required for follicular patterning using directed mosaics. *Development* 125(12):2263-2271.
96. Yu HH, Chen CH, Shi L, Huang Y, & Lee T (2009) Twin-spot MARCM to reveal the developmental origin and identity of neurons. *Nat Neurosci* 12(7):947-953.
97. Mohr SE, Smith JA, Shamu CE, Neumuller RA, & Perrimon N (2014) RNAi screening comes of age: improved techniques and complementary approaches. *Nat Rev Mol Cell Biol* 15(9):591-600.

98. Dietzl G, *et al.* (2007) A genome-wide transgenic RNAi library for conditional gene inactivation in *Drosophila*. *Nature* 448(7150):151-156.
99. Ni JQ, *et al.* (2011) A genome-scale shRNA resource for transgenic RNAi in *Drosophila*. *Nat Methods* 8(5):405-407.
100. Ma Y, Creanga A, Lum L, & Beachy PA (2006) Prevalence of off-target effects in *Drosophila* RNA interference screens. *Nature* 443(7109):359-363.
101. Agrotis A & Ketteler R (2015) A new age in functional genomics using CRISPR/Cas9 in arrayed library screening. *Front Genet* 6:300.
102. Jinek M, *et al.* (2012) A programmable dual-RNA-guided DNA endonuclease in adaptive bacterial immunity. *Science* 337(6096):816-821.
103. Bassett AR, Tibbit C, Ponting CP, & Liu JL (2013) Highly efficient targeted mutagenesis of *Drosophila* with the CRISPR/Cas9 system. *Cell Rep* 4(1):220-228.
104. Kondo S & Ueda R (2013) Highly improved gene targeting by germline-specific Cas9 expression in *Drosophila*. *Genetics* 195(3):715-721.
105. Ren X, *et al.* (2013) Optimized gene editing technology for *Drosophila melanogaster* using germ line-specific Cas9. *Proc Natl Acad Sci U S A* 110(47):19012-19017.
106. Gratz SJ, *et al.* (2013) Genome engineering of *Drosophila* with the CRISPR RNA-guided Cas9 nuclease. *Genetics* 194(4):1029-1035.
107. Yu Z, *et al.* (2013) Highly efficient genome modifications mediated by CRISPR/Cas9 in *Drosophila*. *Genetics* 195(1):289-291.
108. Sebo ZL, Lee HB, Peng Y, & Guo Y (2014) A simplified and efficient germline-specific CRISPR/Cas9 system for *Drosophila* genomic engineering. *Fly (Austin)* 8(1):52-57.
109. Port F, Chen HM, Lee T, & Bullock SL (2014) Optimized CRISPR/Cas tools for efficient germline and somatic genome engineering in *Drosophila*. *Proc Natl Acad Sci U S A* 111(29):E2967-2976.
110. Ren X, *et al.* (2014) Enhanced specificity and efficiency of the CRISPR/Cas9 system with optimized sgRNA parameters in *Drosophila*. *Cell Rep* 9(3):1151-1162.
111. Xie K, Minkenberg B, & Yang Y (2015) Boosting CRISPR/Cas9 multiplex editing capability with the endogenous tRNA-processing system. *Proc Natl Acad Sci U S A* 112(11):3570-3575.
112. Port F & Bullock SL (2016) Augmenting CRISPR applications in *Drosophila* with tRNA-flanked sgRNAs. *Nat Methods* 13(10):852-854.
113. Xue Z, *et al.* (2014) Efficient gene knock-out and knock-in with transgenic Cas9 in *Drosophila*. *G3 (Bethesda)* 4(5):925-929.
114. Ghosh S, Tibbit C, & Liu JL (2016) Effective knockdown of *Drosophila* long non-coding RNAs by CRISPR interference. *Nucleic Acids Res* 44(9):e84.
115. Ewen-Campen B, *et al.* (2017) Optimized strategy for in vivo Cas9-activation in *Drosophila*. *Proc Natl Acad Sci U S A* 114(35):9409-9414.
116. Xue Z, *et al.* (2014) CRISPR/Cas9 mediates efficient conditional mutagenesis in *Drosophila*. *G3 (Bethesda)* 4(11):2167-2173.
117. Jiang W, Brueggeman AJ, Horken KM, Plucinak TM, & Weeks DP (2014) Successful transient expression of Cas9 and single guide RNA genes in *Chlamydomonas reinhardtii*. *Eukaryot Cell* 13(11):1465-1469.

CHAPTER 2

Dendritic space-filling requires a neuronal type-specific extracellular permissive signal in

*Drosophila*¹

INTRODUCTION

The sensory or synaptic input of a neuron is greatly influenced by the morphological characteristics of its dendritic arbor. Different neurons in the same tissue and extracellular microenvironment can develop drastically different dendrite morphologies. While some neurons grow simple dendritic trees with sparse and stereotypic branches, some others are capable of completely and adaptively occupying large receptive fields with a high density of dendrites. The phenomenon of a neuron filling its receptive field with dendrites, sometimes referred to as dendritic space-filling, depends on two intrinsic properties of the neuron: (1) a capacity to grow copious high-order dendrites, and (2) repulsions among homotypic dendrites to keep neighboring branches at an optimal distance. Notable examples of space-filling neurons include cerebellar Purkinje cells (1), retinal ganglion cells (RGCs) and amacrine cells that innervate the inner plexiform layer of the vertebrate retina (2, 3), zebrafish somatosensory neurons that innervate the skin (4), and class IV dendritic arborization (C4da) neurons on the *Drosophila* larval body wall (5). By completely and evenly covering their two-dimensional (2D) target domains, these neurons are able to uniformly sample sensory or synaptic information across the receptive fields (6).

¹ This chapter was previously published as Poe, A.R.*, Tang, L.*, Wang, B., Li, Y., Sapar, M.L., Han, C. (2017). Dendritic space-filling requires a neuronal type-specific extracellular permissive signal in *Drosophila*. *Proc Natl Acad Sci USA*. 114(38):E8062-E8071. *Equal contribution authors. <https://doi.org/10.1073/pnas.1707467114>. Live imaging and immunofluorescence was performed by Amy Poe. Time-lapse imaging was performed by Lingfeng Tang. Most quantifications (except where noted) were performed by Lingfeng Tang with statistical analysis performed by Maria Sapar. Laser ablations were performed by Maria Sapar. Data contributed by Lingfeng Tang, Maria Sapar, & Bei Wang are denoted in the figure legends.

The developmental regulation of space-filling likely relies on both intrinsic properties of a neuron and the extrinsic environment in which it grows. Indeed, a number of neuronal intrinsic factors have been identified that specifically regulate space-filling of neurons. These factors include transcription factors that collectively determine the neuronal identity and bestow upon neurons the capacity to elaborate exuberant neurites (7, 8), motor proteins and components of the secretory pathway that control the number and position of high-order dendrites (9-12), and an amino acid transporter that allows neurons to grow total dendritic length beyond a certain threshold (13). In contrast to intrinsic control of dendritic growth, extracellular regulation of space-filling is more mysterious. Although guidance cues are known to target neurites of some space-filling neurons to the correct spatial domains (14, 15), how neurites interact with the extracellular microenvironment to fill the receptive field once there is more elusive. In particular, whether dendritic space-filling requires unique extracellular permissive signals is currently unknown.

Heparan sulfate proteoglycans (HSPGs) are good candidates for extracellular regulation of space-filling, because they are required for the functions of a large number of extracellular signaling molecules and because HSPGs are ligands for neuronal receptors. HSPGs are membrane and extracellular glycoproteins that contain heparan sulfate (HS) glycosaminoglycan (GAG) chains attached to the protein core (16). With the negatively charged HS chains serving as binding sites for many secreted ligands such as growth factors, morphogens, and axonal guiding molecules, HSPGs are required for the extracellular transport and full biological activities of these ligands (17). In addition, HSPGs are ligands for leukocyte antigen-related (LAR) members of the receptor protein tyrosine phosphatase (RPTP) family. HS chains can bind the immunoglobulin (Ig) ectodomains of LAR and induce LAR clustering (18). In the nervous

system, HSPGs and LAR together regulate axon guidance, synaptogenesis, and axonal regeneration after injury (19, 20). In contrast to the known involvement of HSPGs in axon guidance and outgrowth (15, 18), the roles of HSPGs in dendrite morphogenesis is only beginning to be understood. In *C. elegans*, UNC-52/Perlecan, a secreted HSPG in the basement membrane, indirectly regulates dendritic growth and branching of PVD sensory neurons through patterning hypodermal-derived adhesion signal SAX-7/L1CAM (21). However, whether target tissue-derived HSPGs directly regulate dendritic patterns of specific neurons and how HSPGs affect the cytoskeletal and membrane trafficking machinery in neurite growth and guidance remain to be answered.

Drosophila C4da neurons are a good model system for investigating mechanisms of space-filling. C4da neurons extend dendrites mostly between the basal surface of epidermal cells and the ECM (22, 23). Distinct from other non-space-filling da neurons, larval C4da neurons have a high capacity for growing dynamic, high-order dendritic branches (5, 24). This capacity is essential for C4da neurons to fill the space on the rapidly expanding larval body wall during development (25), or to invade empty receptive fields caused by the loss of neighboring neurons (5, 26). Here we identify epidermis-derived HSPGs as a permissive signal uniquely required for dendritic growth and maintenance of space-filling C4da neurons. This neuronal type-specific permissive role is carried out redundantly by two distinct classes of HSPGs, the Syndecan and the glypican Dally. Using a novel long-term time-lapse live imaging method, we found that HSPGs are not required for extension or branching of high-order dendrites, but rather stabilize dynamic dendritic branches by promoting microtubule stabilization. Furthermore, we present evidence that this HSPG-dependent dendritic growth is not mediated by extracellular ligands diffusing along the epidermal sheet or by potential HSPG receptors in the RPTP family. Our

results therefore reveal novel, critical mechanisms by which the extracellular microenvironment specifically regulates dendritic growth of space-filling neurons.

RESULTS

C4da neurons require epidermis-derived HSPGs for local dendritic growth

To determine whether the space-filling property of C4da neurons is regulated by extracellular signals, we first asked whether target tissue-derived HSPGs contribute to the dendritic growth of C4da neurons by disrupting enzymes that are specifically required for the biosynthesis of HS GAG chains (16). Among these enzymes are HS-glucosamine N-sulfotransferase Sulfateless (*Sfl*), HS polymerase Brother of tout-velu (*Botv*), and two HS copolymerases Tout-velu (*Ttv*) and Sister of tout-velu (*Sotv* or *Ext2*). Because C4da dendrites innervate epidermal cells, we knocked down *sotv* (Figure 2.1B), *ttv* (Figure 2.S1B), and *sfl* (Figure 2.S1C) by RNA interference (RNAi) using a pan-epidermal driver *Gal4^{A58}*. Compared to the control (Figure 2.1A), all of these manipulations resulted in drastic reductions of C4da dendrites within the intrasegmental area at late 3rd instar (96 hours after egg laying (AEL)) as measured by the dendrite density (defined as dendritic length per unit area) (Figure 2.S1D). The reductions are most evident in high-order dendrites, as reflected by the significant decreases of the terminal dendrite density (Figure 2.S1E) and the terminal dendrite number per unit area (referred to as terminal dendrite number hereafter) (Figure 2.S1F). Also associated with these manipulations are more dendrites around tendon cells at the anterior and posterior borders of each segment (outlined by red dots in Figure 2.1B). Tendon cells are muscle attachment sites and express very low levels of Gal4 in *Gal4^{A58}*. The dendrite phenotypes were consistent for all three C4da neurons in each hemisegment, but for simplicity, we focused on the dorsal ddaC neuron in

this study. These data demonstrate that the dendritic growth of C4da neurons requires substrate-derived HSPGs.

HSPGs could promote dendritic growth by modulating global gene transcription in neurons or by regulating local dendritic sprouting. To distinguish between these possibilities, we knocked down *sfl*, *ttv*, *sotv*, and *botv* using *Gal4^{hh}* which is expressed in a stripe of epidermal cells located at the posterior side of each segment (Figure 2.1D-G). We predict that if HSPGs regulate transcription in neurons, knockdown in the *hh*-expressing cells should have no or global effects on dendritic growth in the entire dendritic field. However, if HSPGs promote dendritic growth locally, the effect on dendrite growth should be restricted to the *hh* domain. Strikingly, knockdown of each of the four genes in *hh* epidermal cells led to a more dramatic reduction of dendrites (Figure 2.1H) compared to pan-epidermal knockdowns (Figure 2.S1D). In particular, *sfl* RNAi, *ttv* RNAi, and *sotv* RNAi almost completely eliminated high-order dendrites from the *hh* domain (Figure 2.1I, J). In these domains, only ‘naked’ primary dendritic branches persisted (Figure 2.1D-F). Importantly, the dendrite reductions were only observed in the *hh* domain. These results strongly suggest that epidermis-derived HSPGs locally and post-transcriptionally promote the innervation of receptive fields by C4da dendrites.

Two additional lines of evidence further suggest that the dendrite reductions were due to defects of HS, rather than RNAi off-target effects. First, *ttv* RNAi in the *hh* domain caused a reduction of HS staining (Figure 2.S1G-H’). Second, using mosaic analysis with a repressible cell marker (MARCM) (27) in which *ttv⁶³* homozygous mutant epidermal cells were generated in an otherwise *ttv⁶³* heterozygous background, we observed a cell-autonomous loss of terminal dendrites on *ttv⁶³* mutant epidermal cells (Figure 2.1L-N) when compared to wildtype epidermal clones (Figure 2.1K, K’, and N). *ttv⁶³* clones in tendon cells also inhibited dendritic growth

locally (arrow in Figure 2.1M, M'), suggesting that dendritic innervation at the muscle attachment sites (MAS) requires HSPGs too.

As HSPGs play important roles in epidermal cell patterning and differentiation during embryogenesis, one concern of our experiments is that the lack of dendrites on HSPG-deficient cells may be due to defects of epidermal cells. We examined the morphological characteristics of epidermal cells including adherens junctions, septate junctions, focal adhesions, and the ECM. Knockdown of *ttv* or *sotv* by *Gal4^{hh}* did not alter the expression levels or subcellular localizations of the adherens junction marker E-cad (28) (Figure 2.S1I, I'), the septate junction marker Nrg (29) (Figure 2.S1J, J'), the focal adhesion maker Mys (30) (Figure 2.S1K, K'), and an ECM component Vkg (23) (Figure 2.S1L, L'), suggesting that the above genetic manipulations did not cause obvious morphological defects of epidermal cells.

We further asked whether C4da dendrite innervation depends on the modification state of HS chains. HS activity requires sulfation of its disaccharide units at 2-*O* and 6-*O* positions (31). A secreted endosulfatase Sulf1 can effectively remove 6-*O* sulfate from extracellular HSPGs (32). We over-expressed a membrane-tethered Sulf1 (33) in *hh* cells and observed a nearly complete loss of high-order dendrites on the expressing cells (Figure 2.1O, O', and H-J). This dendrite reduction is as strong as in the knockdown of HS synthesis genes, suggesting that HS mediates most, if not all, of the activity of HSPGs. However, we noticed a distinction between Sulf1 over-expression and knockdown of HS synthesis genes in a one-cell-diameter wide area anterior and adjacent to the *hh* domain (outlined in red dots in Figure 2.1O). In these areas, the total dendrite density was increased in knockdown of HS synthesis genes such as *ttv* but reduced in Sulf1-over-expressing animals (Figure 2.1O-P). The cell-autonomous loss of dendritic coverage on *ttv* RNAi-expressing epidermal cells is consistent with the idea that HS synthesis is

only affected in the RNAi-expressing cells (Figure 2.1Q). In contrast, plasma membrane-located Sulf1 on *hh*-expressing cells can potentially act on the wildtype cells directly contacting Sulf1-expressing cells (Figure 2.1Q) and cause non-autonomous dendrite reduction. Together, our results indicate that HS on the epidermal surface is required for local innervation of epidermal cells by space-filling C4da dendrites.

Figure 2.1. Epidermis-derived HSPGs are required for local growth of C4da dendrites.

(A and B) DdaC neurons in the *Gal4^{A58}* control (A) and an animal expressing *Gal4^{A58}*-driven *sotv RNAi* (B). Red dots outline the muscle attachment sites (MAS). (C-G') DdaC neurons in the *Gal4^{hh}* control (C and C') and animals expressing *sfl RNAi* (D and D'), *ttv RNAi* (E and E'), *sotv RNAi* (F and F'), and *botv RNAi* (G and G') in the *hh* domain. Blue dots outline *hh* domains (upper panels). Lower panels show *hh* domains (green) and C4da dendrites (magenta). (H-J) Quantification of total dendrite density (H), terminal dendrite density (I), and terminal dendrite number (J) in *hh* domains. *** $p \leq 0.001$; ANOVA and Tukey's HSD test. (K-M') Epidermal MARCM clones of wildtype (K, K') and *ttv⁶³* (L-M'). Arrows point to a *ttv⁶³* epidermal clone at the MAS (M, M'). Merge panels show epidermal clones in green and C4da dendrites in magenta. (N) Quantification of terminal dendrite density in epidermal MARCM clones. *** $p \leq 0.001$; Student's t-test. (O and O') A ddaC neuron in an animal expressing membrane-tethered DSulf1 in the *hh* domain. Blue dots outline the *hh* domain and red dots outline a one-cell-diameter-wide area anterior to the *hh* domain (O). *Gal4^{hh}*-expressing cells are in green and C4da dendrites are in magenta (O'). (P) Quantification of total dendrite density in the one-cell-diameter-wide area anterior to the *hh* domain. *** $p \leq 0.001$; ANOVA and Tukey's HSD test. (Q) A diagram showing the effects of expressing *ttv RNAi* and membrane-tethered DSulf1 on epidermal HSPGs. Knockdown of *ttv* leads to the loss of HSPG GAG chains only on RNAi expressing cells (dark blue), while membrane-tethered DSulf1 removes 6-O-sulfates of HSPG GAG chains on both DSulf1-expressing cells and cells directly contacting them (light blue). For all quantifications, each circle represents a neuron. The numbers of neurons are indicated. Black bar: mean; red bars: SD. Scale bars represent 50 μm . Imaging was performed by Amy Poe. Quantifications were performed by Lingfeng Tang and Maria Sapar.

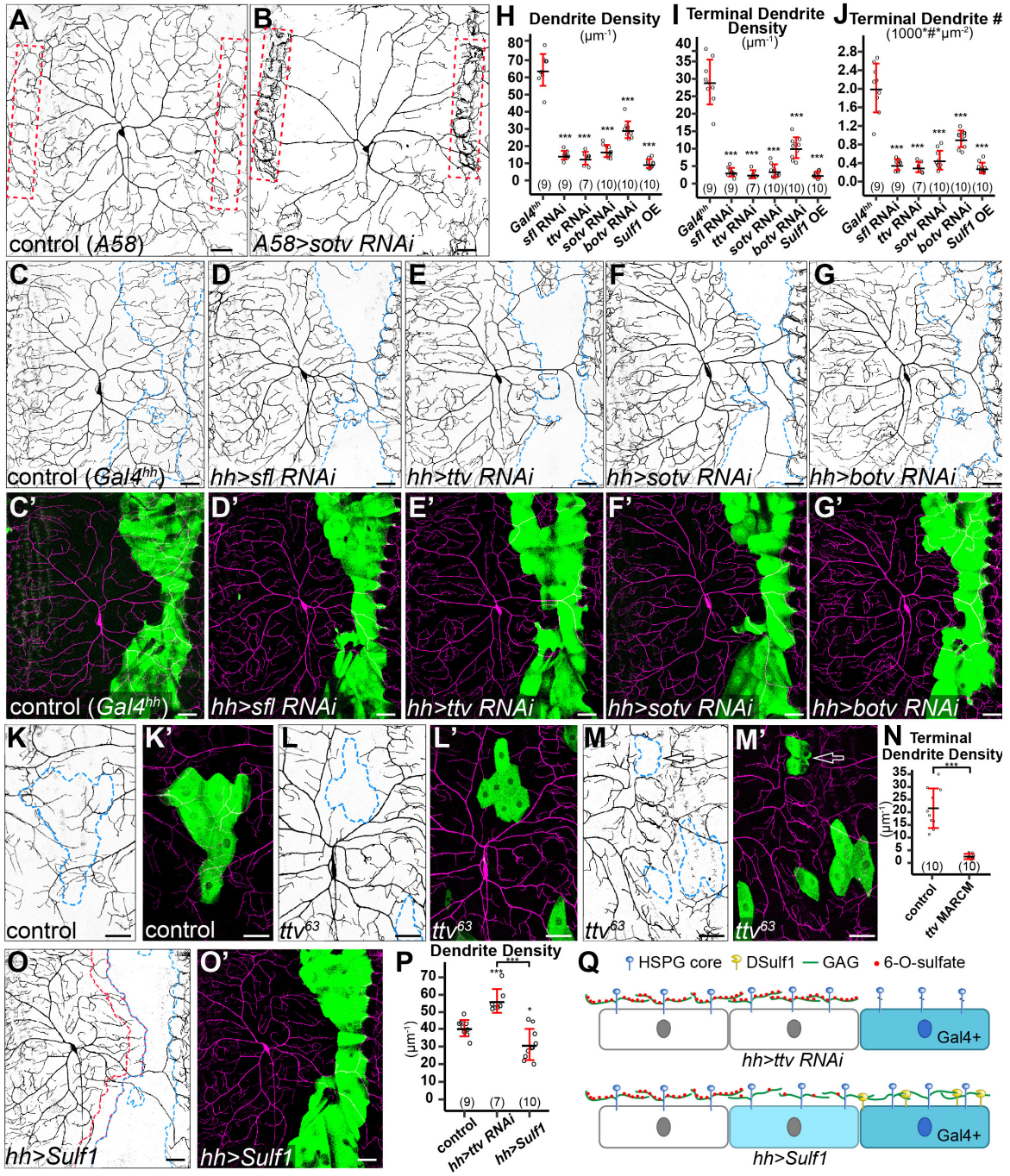
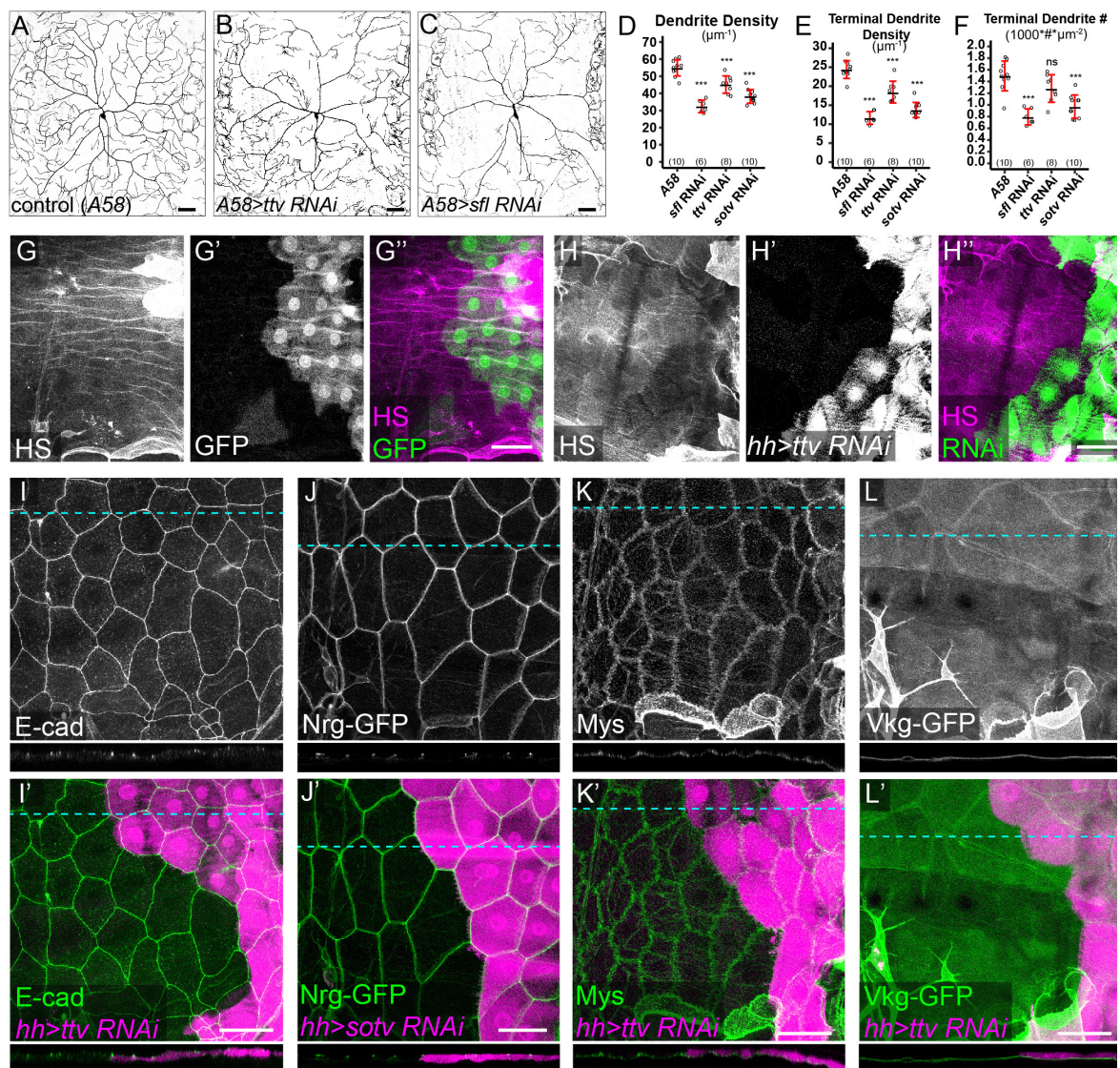


Figure 2.S1. Effects of knockdown of HS synthesis genes on dendrite morphology, HS level, and epithelial morphology.

(A-C) DdaC dendritic fields of a *Gal4^{A58}* control animal (A) and animals expressing *Gal4^{A58}>ttv RNAi* (B) and *Gal4^{A58}>sfl RNAi* (C). (D-F) Quantification of total dendrite density (D), terminal dendrite density (E), and terminal dendrite number (F) of control and RNAi animals. *** $p \leq 0.001$; ns, not significant; one-way analysis of variance and Tukey's HSD test. For all quantifications, each circle represents an individual neuron. The number of neurons for each genotype is indicated. The black bars represent the mean and the red bars represent the standard deviation. (G-H'') Immunostaining of heparan sulfate (HS) in a *Gal4^{hh}>GFP* control animal (G-G'') and an animal expressing *Gal4^{hh}>ttv RNAi* (H-H''). HS was stained with the antibody 3G10 which recognizes heparinase III-digested HS. (I-L') Expression of E-Cad (I and I'), Nrg-GFP (J and J'), Mys (K and K'), and Vkg-GFP (L and L') in animals expressing *Gal4^{hh}>ttv RNAi* (I, I', K, K', L, and L') and *Gal4^{hh}>sotv RNAi* (J and J'). E-Cad and Mys expressions were detected by antibody staining and Nrg-GFP and Vkg-GFP expressions were detected using GFP trap lines. A cross-section for each marker is shown below each 2D projection image. Blue dotted lines indicate locations of cross-sections. Scale bars represent 50 μm . Imaging was performed by Amy Poe. Quantifications were performed by Lingfeng Tang and Maria Sapar.



HSPGs are specifically required for the dendritic growth and maintenance of space-filling sensory neurons

The dendrite reduction associated with HSPG deficiency observed at the late 3rd instar larval stage could be due to a lack of dendritic growth or a failure to maintain existing dendrites. To distinguish between these two possibilities, we examined control and *Gal4^{hh}>ttv RNAi* animals at younger larval stages, including the beginning of the first instar (24 hr AEL), the beginning of the second instar (48 hr AEL), and early third instar (72 hr AEL). Compared to the control (Figure 2.2A-C), *ttv* RNAi (Figure 2.2D-F) caused dendritic reduction as early as 24 hr AEL. The reduction became more severe at 48 hr AEL and 72 hr AEL (Figure 2.2G, H). These data demonstrate that HSPGs are required for dendrite growth of C4da neurons.

To determine if HSPGs are continuously required to maintain dendrites, we investigated the effects of late removal of HSPGs by controlling *Sulf1* over-expression using temperature sensitive *Gal80* (*Gal80^{ts}*) (34). Animals were allowed to develop at 18°C to suppress *Gal4* activity until early third instar and then shifted to 28°C to induce *Sulf1* expression in the *hh* domain for 24 hours. Although dendritic patterns were indistinguishable between the control and *hh>Sulf1* before the temperature shift, *Sulf1* induction caused dramatic dendrite reduction (Figure 2.2I-L). The *Sulf1*-expressing regions contained few high-order dendrites, suggesting that HSPG removal caused regression of earlier high-order dendrites. However, late induction of *Sulf1* led to a relatively weaker dendrite reduction (i.e. more low order dendrites) compared to that caused by early and persistent *Sulf1* expression (Figure 2.2K, L). This result suggests that some dendritic branches had been stabilized before *Sulf1* induction and they persisted with late HSPG removal. Together, these data suggest that HSPGs are required to maintain high-order dendrite branches but not those that are already stabilized.

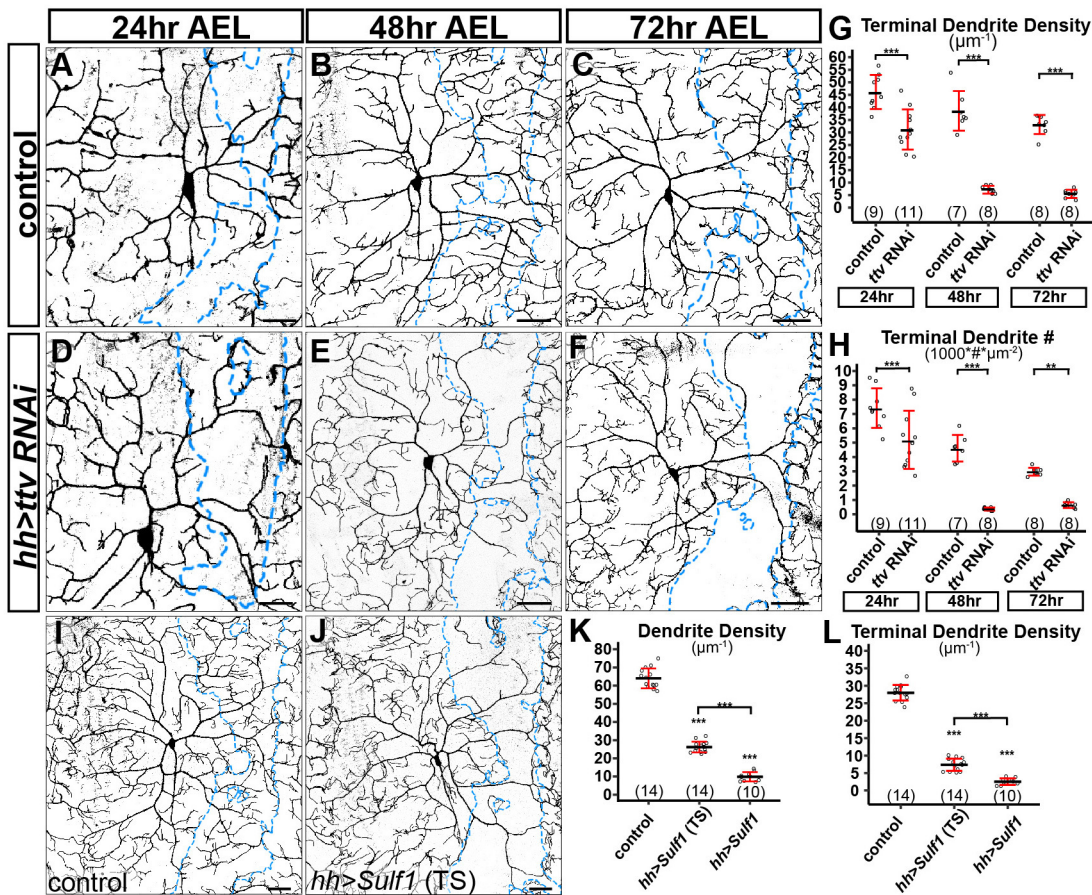


Figure 2.2. HSPGs are specifically required for dendrite development of C4da neurons.

(A-F) DdaC in the *Gal4^{hh}* control (A-C) and *Gal4^{hh}*-driven *ttv RNAi* (D-F) at three developmental stages. (G and H) Quantification of terminal dendrite density (G) and terminal dendrite number (H) in *hh* domains. ** $p \leq 0.01$; *** $p \leq 0.001$; Student's t-test. (I and J) DdaC in the control (*tubP-Gal80^{ts}; Gal4^{hh}*) (I) and an *Sulf1*-expressing animal (*tubP-Gal80^{ts}; hh>Sulf1*) in which *Sulf1* expression was induced by temperature shift (TS) (J). Both genotypes were subjected to TS. (K and L) Quantification of dendrite density (K) and terminal dendrite density (L) in *hh* domains of *Gal4^{hh}* control, *hh>Sulf1* (TS), and *hh>Sulf1* (constant expression). *** $p \leq 0.001$; ns, not significant; ANOVA and Tukey's HSD test. For all quantifications, each circle represents a neuron. The numbers of neurons are indicated. Black bar: mean; red bars: SD. Scale bars represent 10 μm in (A) and (D), 35 μm in (B) and (E), and 50 μm in the rest of panels. Imaging was performed by Amy Poe. Quantifications for G & H were performed by Lingfeng Tang and Maria Sapar. Quantifications for K & L were performed by Amy Poe.

The *Drosophila* peripheral nervous system (PNS) has four classes of da sensory neurons with overlapping dendritic fields (35), with C4da as the only space-filling neurons. We wondered whether HSPGs are required for the arborization of the other three classes. We examined the dendritic patterns of dorsal class I da neurons ddaD and ddaE (Figure 2.S2A-C), the ventral class II da neuron ddaB (Figure 2.S2D-F), and dorsal class III da neurons ddaA and ddaF (Figure 2.S2G-K) in epidermal knockdown of *ttv*. Pan-epidermal knockdown of *ttv* caused a slight reduction of class I ddaD dendrites and a slight increase of class I ddaE dendrites (Figure 2.S2C). Pan-epidermal knockdown of *ttv* also caused a mild increase of class II ddaB dendrites (Figure 2.S2F). For C3da neurons, knockdown of *ttv* in the *hh* domain did not affect the dendrites of ddaF but mildly reduced the total dendritic length, terminal dendritic length, and total terminal dendrite number of ddaA within the *hh* domain (Figure 2.S2I-K). These data demonstrate that although HSPGs can mildly influence the dendrites of class I-III, the dendritic growth of these neurons during larval development does not rely on HSPGs. Therefore, HSPGs are specifically required for the dendritic development of space-filling C4da neurons.

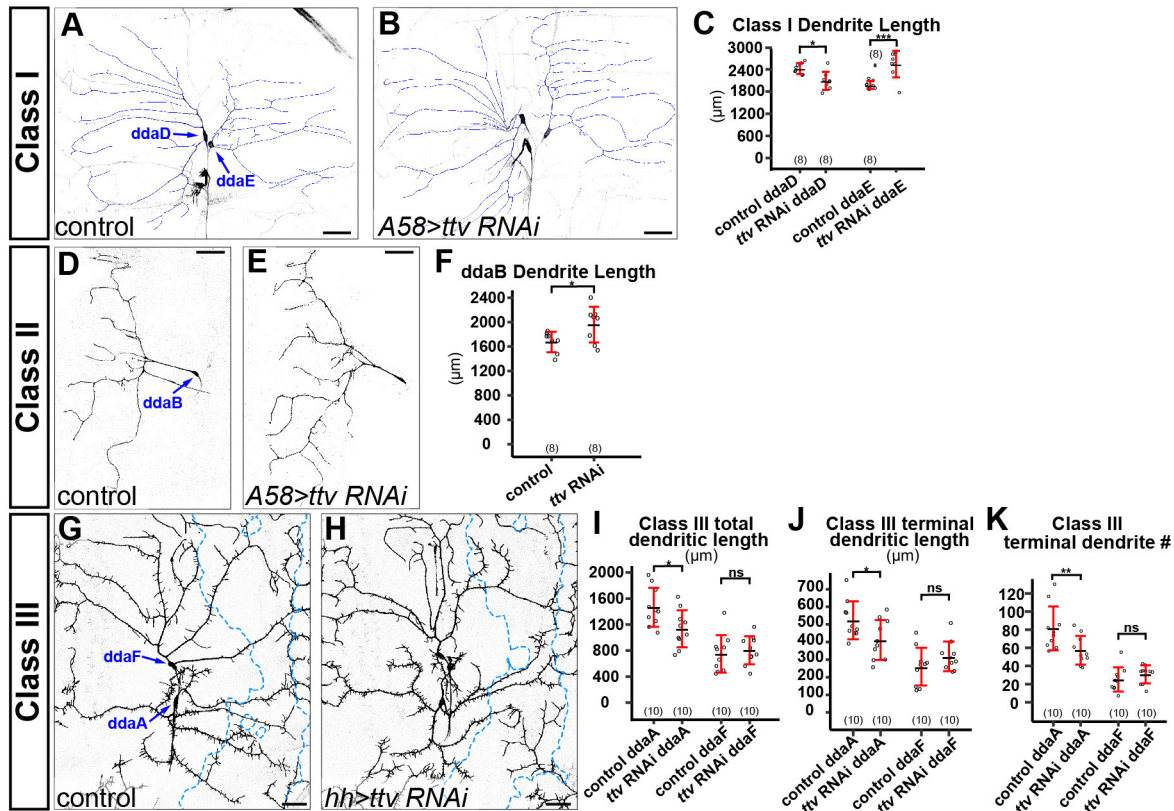


Figure 2.S2. HSPGs are not required for dendrite growth of other classes of da neurons.

(A and B) Dendritic fields of class I *ddaD* and *ddaE* neurons in a *Gal4^{A58}* control animal (A) and an animal expressing *Gal4^{A58}*-driven *ttv RNAi* (B). The dendrites are overlaid with blue lines. (C) Quantification of class I total dendrite length of control and *ttv RNAi* animals. * $p \leq 0.05$; *** $p \leq 0.001$; Student's t-test. (D and E) Dendritic fields of class II *ddaB* neurons in a *Gal4^{A58}* control animal (D) and an animal expressing *Gal4^{A58}*-driven *ttv RNAi* (E). (F) Quantification of *ddaB* total dendrite length of control and *ttv RNAi* animals. * $p \leq 0.05$; Student's t-test. (G and H) Dendritic fields of class III *ddaF* and *ddaA* neurons in a *Gal4^{hh}* control animal (G) and an animal expressing *Gal4^{hh}*-driven *ttv RNAi* (H). Blue dots outline *hh* domains. (I-K) Quantification of total dendrite density (I), terminal dendrite density (J), and terminal dendrite numbers (K) in *hh* domains of control and *ttv RNAi* animals. * $p \leq 0.05$; ** $p \leq 0.01$; ns, not significant; Student's t-test. For all quantifications, each circle represents an individual neuron. The number of neurons for each genotype is indicated. The black bars represent the mean and the red bars represent the standard deviation. Scale bars represent 50 μm . Imaging was performed by Amy Poe. Reagents for these experiments were contributed by Bei Wang. Quantifications in C, F, and I-K were performed by Lingfeng Tang.

Sdc and Dally play partially redundant roles in promoting C4da dendritic growth

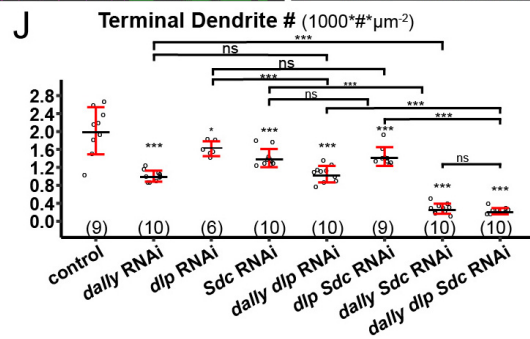
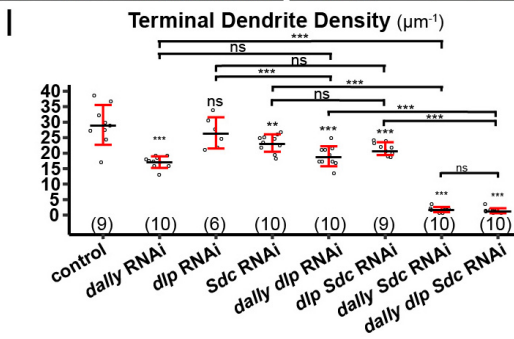
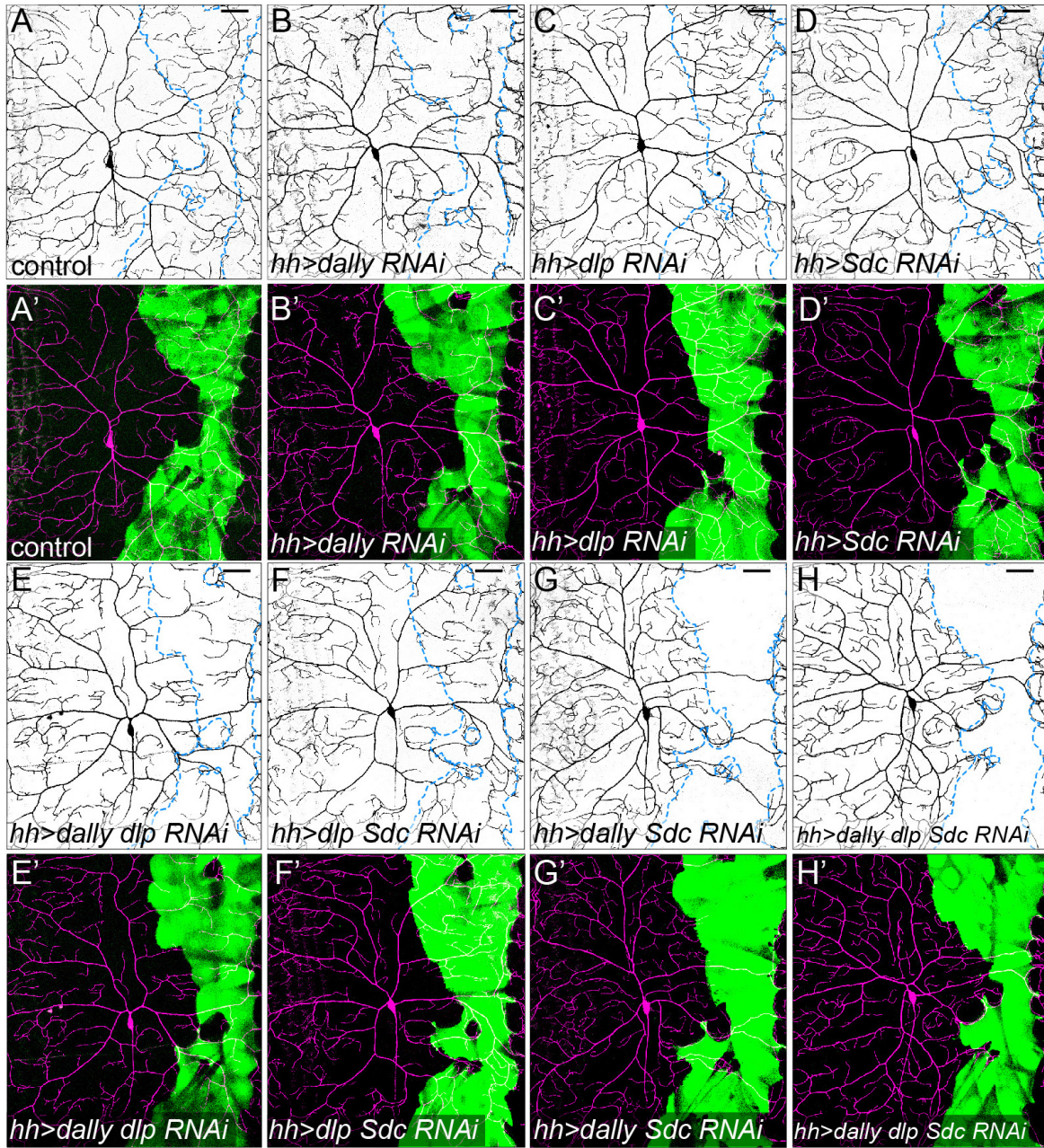
Drosophila has four HSPG core proteins, including two GPI-anchored glypicans, Division abnormally delayed (Dally) and Dally-like (Dlp), one transmembrane syndecan (Sdc), and one secreted perlecan, Trol (16). We next asked which HSPG core proteins are necessary for C4da dendritic growth. We focused on glypicans and the syndecan, as they are more commonly involved in signaling than perlecans (17). Knockdown of either *dally* (Figure 2.3B, B') or *Sdc* (Figure 2.3D, D') caused a mild dendrite reduction (Figure 3I, J), while *dlp* knockdown had little effect (Figure 2.3C, C', I, J). Knockdown of *trol* did not produce obvious dendritic defects either. The lack of strong phenotypes in these experiments may be due to poor knockdown efficiency or functional redundancy among HSPGs. To evaluate these possibilities, we first tested the efficiency of RNAi in knocking down endogenous or overexpressed HSPGs in epidermal cells. Imaging of protein trap lines *Sdc-GFP* (Figure 2.S3A, A'), *dally-YFP* (Figure 2.S3D, E), and *dlp-YFP* (Figure 2.S3F) showed that larval epidermal cells express all three HSPGs with the expected membrane localization. *Sdc-GFP* (Figure 2.S3A, A') and *Dally-YFP* (Figure 2.S3D) were efficiently knocked down in cells expressing their corresponding RNAi constructs. For *dlp*, we co-expressed *UAS-dlp-GFP* with either *UAS-dally-RNAi* (as a negative control) (Figure 2.S3B, B') or *UAS-dlp-RNAi* (Figure 2.S3C, C') in the *hh* domain. *Dlp-GFP* was strongly expressed in the presence of *dally RNAi* but is absent when co-expressed with *dlp RNAi*. While *dlp RNAi* is effective in suppressing *Dlp-GFP* expression, it had no detectable effect on *Dally-YFP* expression (Figure 2.S3E). These data demonstrate that HSPG knockdowns are effective and RNAi constructs for *dally* and *dlp* are specific.

We next tested whether HSPGs act redundantly to promote C4da dendritic growth by knocking down *dally*, *dlp*, and *Sdc* in all possible combinations. Knockdown of both *dally* and

Sdc in epidermal cells (Figure 2.3G, G') almost completely blocked high-order dendritic growth (Figure 2.3I, J), mirroring the phenotypes of *sfl*, *ttv*, and *sotv* knockdown (Figure 2.1). In contrast, the additional knockdown of *dlp* did not enhance the dendritic reduction in *dally* RNAi (Figure 2.3E, E'), *Sdc* RNAi (Figure 2.3F, F'), or *dally Sdc* RNAi (Figure 2.3H, H'), indicating that Dlp does not play a significant role in C4da dendritic growth. Together, these results demonstrate that Dally and Sdc play partially redundant roles in promoting C4da dendrite development.

Figure 2.3. *Sdc* and *dally* play partially redundant roles in promoting dendritic growth of C4da neurons.

(A-H') DdaC in the *Gal4^{hh}* control (A and A'), and animals expressing *dally RNAi* (B and B'), *dlp RNAi* (C and C'), *Sdc RNAi* (D and D'), *dally dlp RNAi* (E and E'), *dlp Sdc RNAi* (F and F'), *dally Sdc RNAi* (G and G'), and *dally dlp Sdc RNAi* (H and H') in the *hh* domain. Blue dots outline *hh* domains (upper panels). Lower panels show *Gal4^{hh}*-expressing cells in green and C4da dendrites in magenta. (I and J) Quantification of terminal dendrite density (I) and terminal dendrite number (J) in *hh* domains. * $p \leq 0.05$; ** $p \leq 0.01$; *** $p \leq 0.001$; ns, not significant; ANOVA and Tukey's HSD test. For all quantifications, each circle represents a neuron. The numbers of neurons are indicated. Black bar: mean; red bars: SD. Scale bars represent 50 μm . Imaging was performed by Amy Poe. Quantifications were performed by Lingfeng Tang and Maria Sapar.



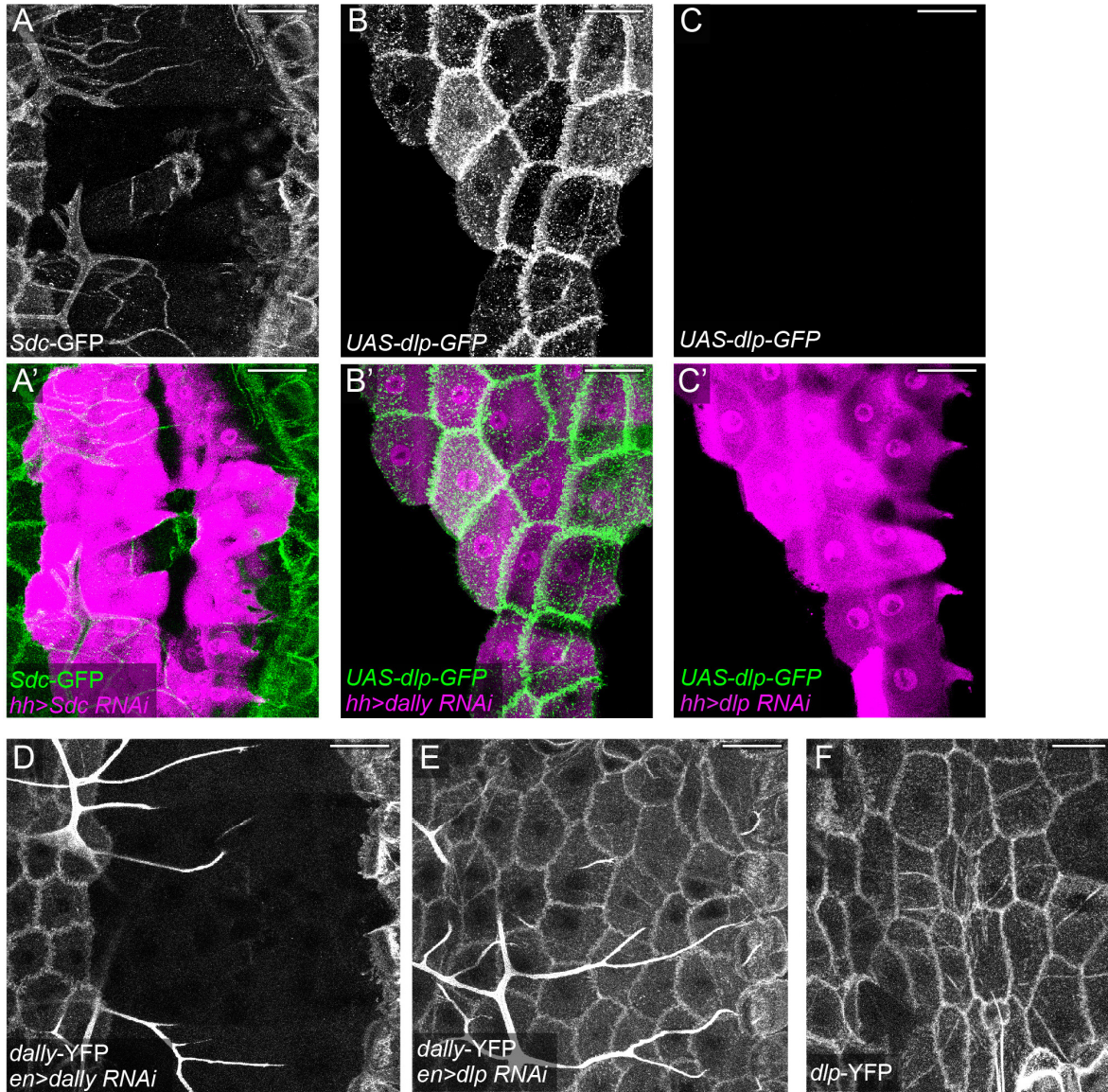


Figure 2.S3. Effectiveness and specificity of HSPG RNAi.

(A and A') *Sdc-GFP* protein trap expression in an animal expressing *Gal4^{hh}>Sdc RNAi*. Lower panel shows RNAi-expressing cells in magenta and *Sdc-GFP* in green. (B-C') An animal expressing *Gal4^{hh} UAS-dlp-GFP UAS-dally RNAi* (B and B') and an animal expressing *Gal4^{hh} UAS-dlp-GFP UAS-dlp RNAi* (C and C'). Lower panels show RNAi-expressing cells in magenta and *Dlp-GFP* expression in green. (D and E) *dally-YFP* protein trap expression in an animal expressing *Gal4^{en}>dally RNAi* (D) and an animal expressing *Gal4^{en}>dlp RNAi* (E). (F) *dlp-YFP* protein trap expression in the epidermis. All animals are 96 hr AEL larvae. Scale bars represent 50 μm. Imaging was performed by Amy Poe.

HSPGs stabilize high-order C4da dendrites at least partially by promoting microtubule stabilization

C4da neurons are unique among da neurons in that they continuously sprout new branches to innervate unoccupied epidermal space during development. To understand the molecular mechanism and neuronal specificity of HSPG-dependent dendritic growth, we first investigated how growing C4da dendrites behave when encountering HS-deficient epidermal cells. Addressing this question required long-term live imaging of C4da dendrites. However, common methods for immobilizing and mounting *Drosophila* larvae generally cause animal lethality within 30 minutes, and thus do not permit live imaging long enough for capturing both short-term dendrite dynamics and long-term changes of dendritic patterns. Therefore, we developed a method of long-term time-lapse imaging for *Drosophila* larvae (see Methods). This method allows for continuous live imaging of da neurons in partially immobilized larvae for longer than 10 hours. Using this method, we examined the dendrite dynamics of C4da neurons in animals expressing *ttv RNAi* in *hh* epidermal cells between 72 hr AEL and 84 hr AEL. Our time-lapse analyses show that the high-order C4da dendrites are highly dynamic at the border of HS-deficient zones (Figure 2.4A and [Movie 2.S1](#)). Instead of halting at the border, growing dendritic tips could extend tens of microns into the HS-deficient zone. In addition, the primary dendrites that persisted in the HS-deficient zone also sprouted many new branches during the course of the time-lapse. The presence of high-order dendrites in the HS-deficient zone during the time-lapse imaging is also demonstrated by plotting the locations of dendrite endings in all frames (Figure 2.4A'). However, high-order dendrites in the HS-deficient zone were transient and there was no obvious net increase of the total dendrite length or the terminal dendrite number during the imaging (Figure 2.4A''). We imaged 55 neurons and observed consistent results.

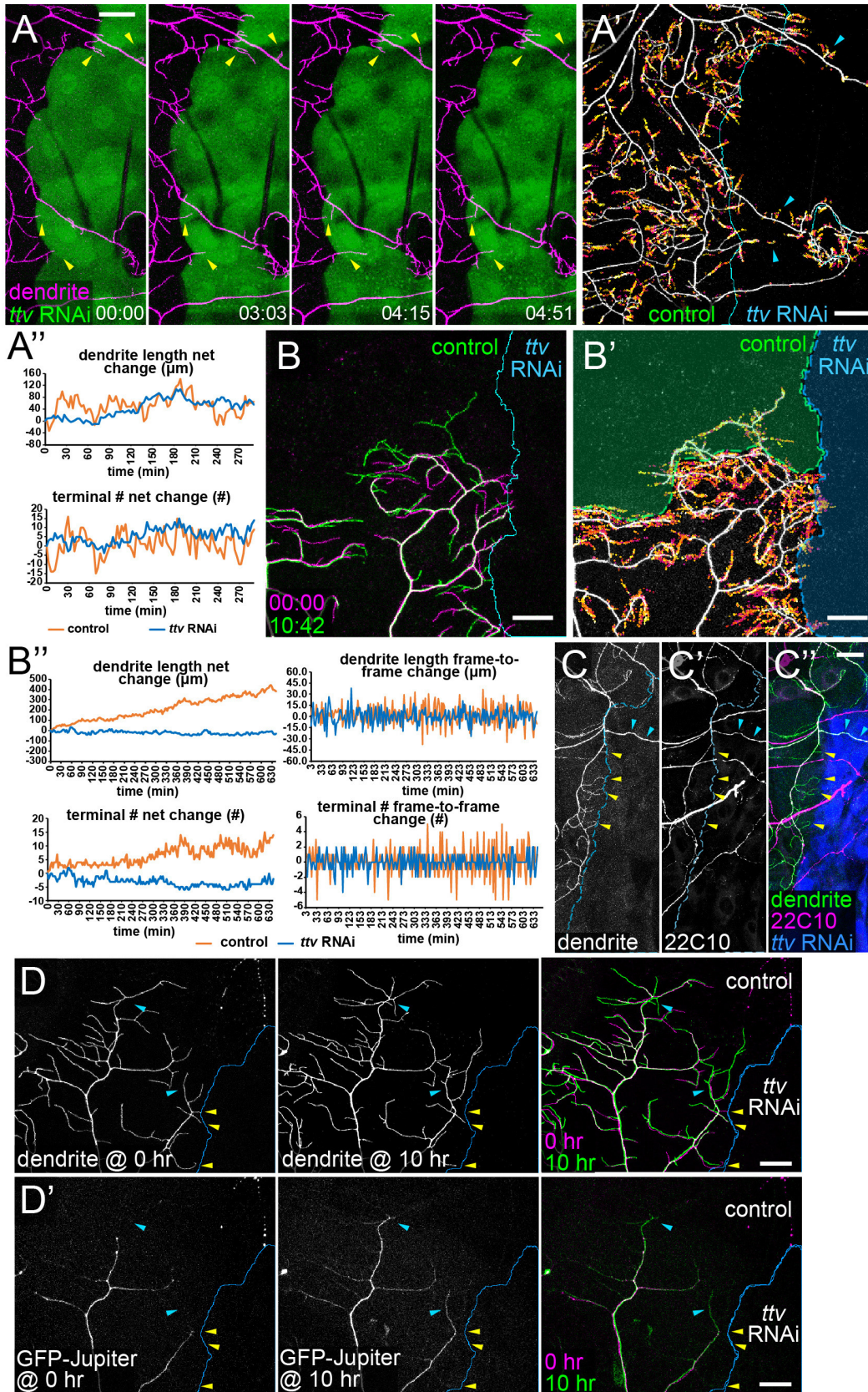
C4da dendrites are known to be dynamic during early third instar (24). Indeed, our time-lapse data revealed that high-order C4da dendrites in the control region were active in exploratory behaviors including extension, retraction, turning, and branching ([Movie 2.S1](#)). Dendrite-dense control regions often did not exhibit robust net dendrite growth within a few hours (Figure 2.4A’), likely due to the inhibitory effect of homotypic dendritic repulsion (26, 35). To rule out the possibility that high-order C4da dendrites are intrinsically unstable and therefore cannot permanently invade empty spaces at this stage, we did similar time-lapse experiments, except that we additionally laser-ablated the ddaC neurons on the right side of the larva between 48-60 AEL. The ablation presented the ddaC neurons on the left side with an empty, but otherwise wildtype, territory at the dorsal midline. Such HS-positive empty territory does not impose homotypic repulsion onto dendrites and therefore is a better internal control for the HS-deficient zone. In these experiments, although high-order dendrites at the dorsal midline were still very dynamic, dendritic arbors gradually expanded into the empty wildtype spaces (Figure 2.4B-B’, and [Movie 2.S2](#)). In contrast, there was no net growth of dendrites into HS-deficient zones in the same experiments, even though high order dendrites in wildtype empty zones and HS-deficient zones were similarly dynamic from frame to frame (Figure 2.4B’). We imaged 16 neurons and observed consistent results. These data strongly suggest that HSPGs are not required for short-term dynamics of C4da dendrites, but are necessary to stabilize growing dendrites.

An important mechanism of dendrite stabilization is microtubule stabilization and bundling by microtubule-associated proteins (MAPs) (36). A hallmark of stabilized microtubules in da dendrites is the presence of Futsch, the *Drosophila* MAP1, which is restricted to stable neuronal microtubule bundles (37). To further investigate how HSPGs stabilize growing

dendrites, we examined the distribution of Futsch in C4da dendrites using the antibody 22C10 (37). Futsch was detected in the primary dendrites that persisted in the HS-deficient zone (cyan arrowheads in Figure 2.4C-C’), consistent with these dendrites being stabilized. In contrast, the high-order C4da dendrites at the border of the HS-deficient zone lacked detectable Futsch staining (yellow arrowheads in Figure 2.4C-C’). The correlation between epidermal HS-deficiency and the lack of bundled microtubules in high-order C4da dendrites supports the idea that HS may stabilize growing dendrites by promoting microtubule stabilization and bundling. To further investigate the dynamics of bundled microtubules in C4da neurons, we expressed GFP-Jupiter in C4da neurons and simultaneously knocked down *ttv* in *hh*-expressing epidermal cells. Jupiter is a *Drosophila* MAP (38) and its distribution upon exogenous expression in da neurons matches that of Futsch. In this experiment, we ablated ddaC neurons on one side of the larva so as to induce long-term dendritic growth of the remaining ddaC neurons. Over the course of 10 hours, we indeed observed gradual appearance of GFP-Jupiter in newly stabilized dendritic branches at the border of the empty, wildtype space (cyan arrowheads in Figure 2.4D, D’) (100%, n=10). In contrast, GFP-Jupiter was never detected in the high-order dendrites that straddled the border of the HS-deficient zone (yellow arrowheads in Figure 2.4D, D’). Together, these data suggest that HSPGs promote C4da dendritic growth at least partially by stabilizing newly formed dendrites through microtubule stabilization and bundling.

Figure 2.4. HSPGs stabilize high-order C4da dendrites by promoting microtubule bundling.

(A) Selected frames from a time-lapse series showing ddaC dendrites (magenta) at the border of *ttv RNAi*-expressing epidermal cells (green). Yellow arrows indicate terminal branches temporarily invading the HS-deficient zone. Times (HH:MM) are relative to the first frame. (A') Projection of dendrite endings over time with ending locations in each frame temporally color-coded (early: magenta; late: yellow). The blue line indicates borders of HS-deficient regions. Arrowheads point to dendrite endings in the HS-deficient region. (A'') Net changes in dendrite length and terminal dendrite numbers (relative to the first frame) in HS-positive ("control", orange lines) and HS-deficient ("*ttv RNAi*", blue lines) regions at each time point. (B-B'') Time-lapse imaging of ddaC dendrites next to an HS-deficient region (*Gal4^{hh}>ttv RNAi*) on the right and an empty wildtype epidermal region on the top. (B) Dendritic patterns of the first frame (magenta) and the last frame (green). Times (HH:MM) are relative to the first frame. (B') Projection of dendritic endings over time. The dendritic pattern and the border are from the last frame. The green overlay indicates a wildtype epidermal region ("control"), which was empty in the first frame, and the blue overlay indicates the HS-deficient region ("*ttv RNAi*"). (B'') Dendrite dynamics in control (orange lines) and *ttv RNAi* (blue lines) regions at each time point. Graphs on the left show net changes in dendrite length and terminal dendrite numbers relative to the first frame. Graphs on the right show frame-to-frame changes in dendrite length and terminal dendrite numbers. The control and *ttv RNAi* regions show similar sizes of frame-to-frame changes in the early part of the time-lapse, but later the control region displays greater frame-to-frame changes due to the more dendrites accumulated in the control region. (C-C'') Immunostaining of 22C10 in *Gal4^{hh}>ttv RNAi*. Yellow arrowheads point to 22C10-negative terminal dendrites at the border of the HS-deficient zone. Blue arrowheads point to 22C10-positive primary branches within the HS-deficient zone. The merge (C'') shows *hh*-expressing cells in blue, 22C10 staining in magenta, and C4da dendrites in green. (D and D') Time-lapse snapshots of ddaC dendrites that are next to an HS-deficient region (*Gal4^{hh}>ttv RNAi*) on the right and an empty wildtype region on the top. Times 0 hr and 10 hr are shown in separate and merged panels. (D) shows dendritic patterns and (D') shows GFP-Jupiter that labels bundled microtubules in the dendrites. Yellow arrowheads point to GFP-Jupiter-negative terminal dendrites at the border of the HS-deficient zone. Blue arrowheads point to newly stabilized high-order dendrites that are invaded by GFP-Jupiter at 10 hr. Scale bars represent 25 μ m. Reagents for these experiments were contributed by Bei Wang. Time-lapse imaging in panels A, B, and D was performed by Lingfeng Tang. Laser ablations in panels B and D were performed by Maria Sapar and Amy Poe. Antibody staining was performed by Amy Poe. Quantifications of time-lapse movies in panels A'' and B'' were performed by Chun Han.



To further understand the impact of HS deficiency on microtubule dynamics in C4da neurons, we also examined microtubule growth behaviors using EB1-GFP (39), which binds growing microtubule plus ends. As EB1-GFP is difficult to detect in terminal dendrites, we mainly focused on the primary dendritic branches in the HS-deficient zone (Figure 2.S4A, B). We noticed a slightly more variable and decreased speed of EB1-GFP comets (Figure 2.S4C) and a mild increase of the fraction of anterograde comets (Figure 2.S4D) in HS deficiency, but no difference in comet frequency (Figure 2.S4E) or duration (Figure 2.S4F). These weak effects suggest that changes in microtubule growth dynamics probably are not a major cause of the dendritic reduction in HS deficiency.

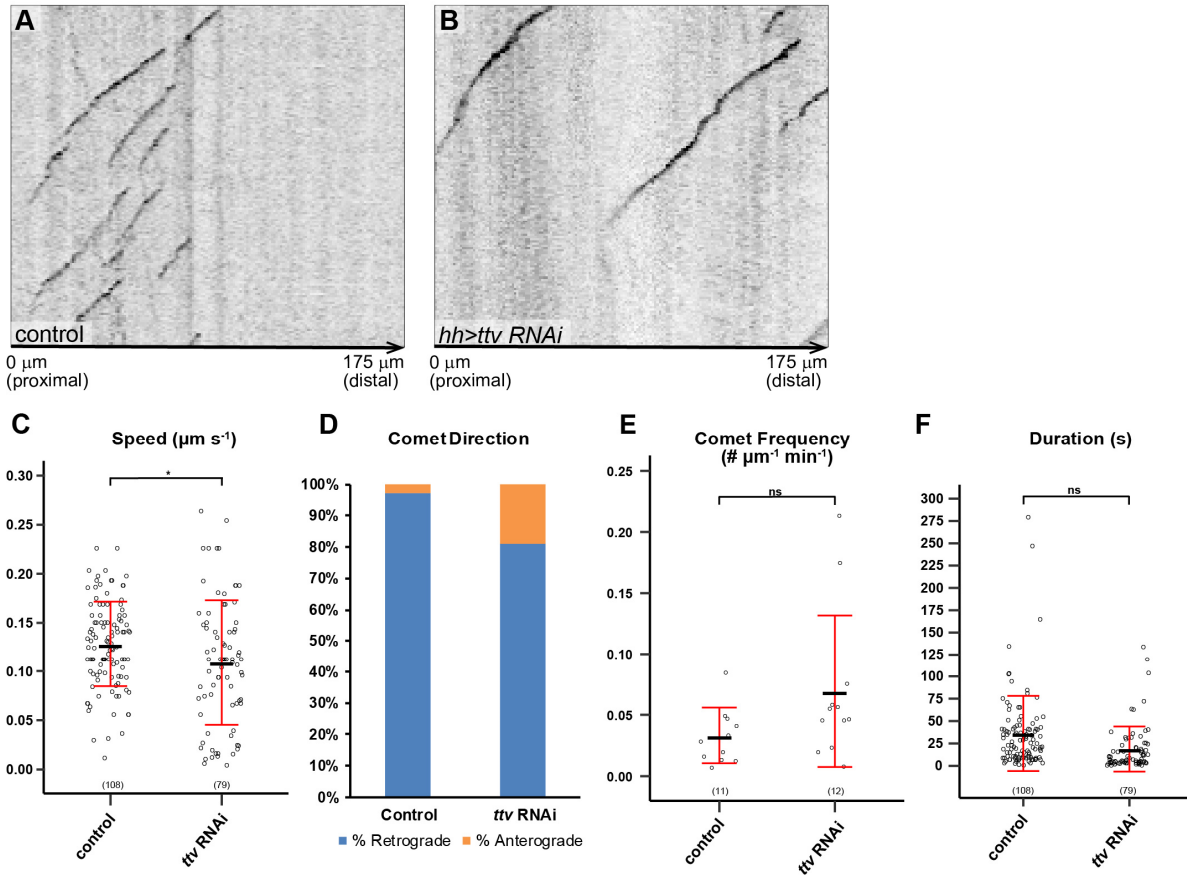


Figure 2.S4. Dynamics of EB1-GFP in *ttv* knockdown.

(A and B) Example kymographs of EB1-GFP comets in primary branches in the *hh* domain in a wildtype (A) and a *Gal4^{hh}>ttv RNAi* (B) animal. The left edge of each kymograph marks the left border of the *hh* domain. The proximal-distal orientation of the dendrite and the distance from the border of the *hh* domain are labeled at the bottom of each panel. (C-F) Quantification of EB1-GFP comet speed ($\mu\text{m/s}$) (C), comet direction (D), comet frequency ($\# \cdot \text{min}^{-1} \cdot \mu\text{m}^{-1}$) (E), and comet duration (s) (F) in wildtype and *Gal4^{hh}>ttv RNAi* animals. For comet direction, the percentage of retrograde comets is shown in blue and the percentage of anterograde comets is shown in orange. * $p \leq 0.05$; ns, not significant; Student's t-test. For all quantifications, each circle represents a single EB1-GFP comet. The number of comets for each genotype is indicated. The black bars represent the mean and the red bars represent the standard deviation. This work was contributed by Lingfeng Tang. Quantifications were performed by Lingfeng Tang and Amy Poe.

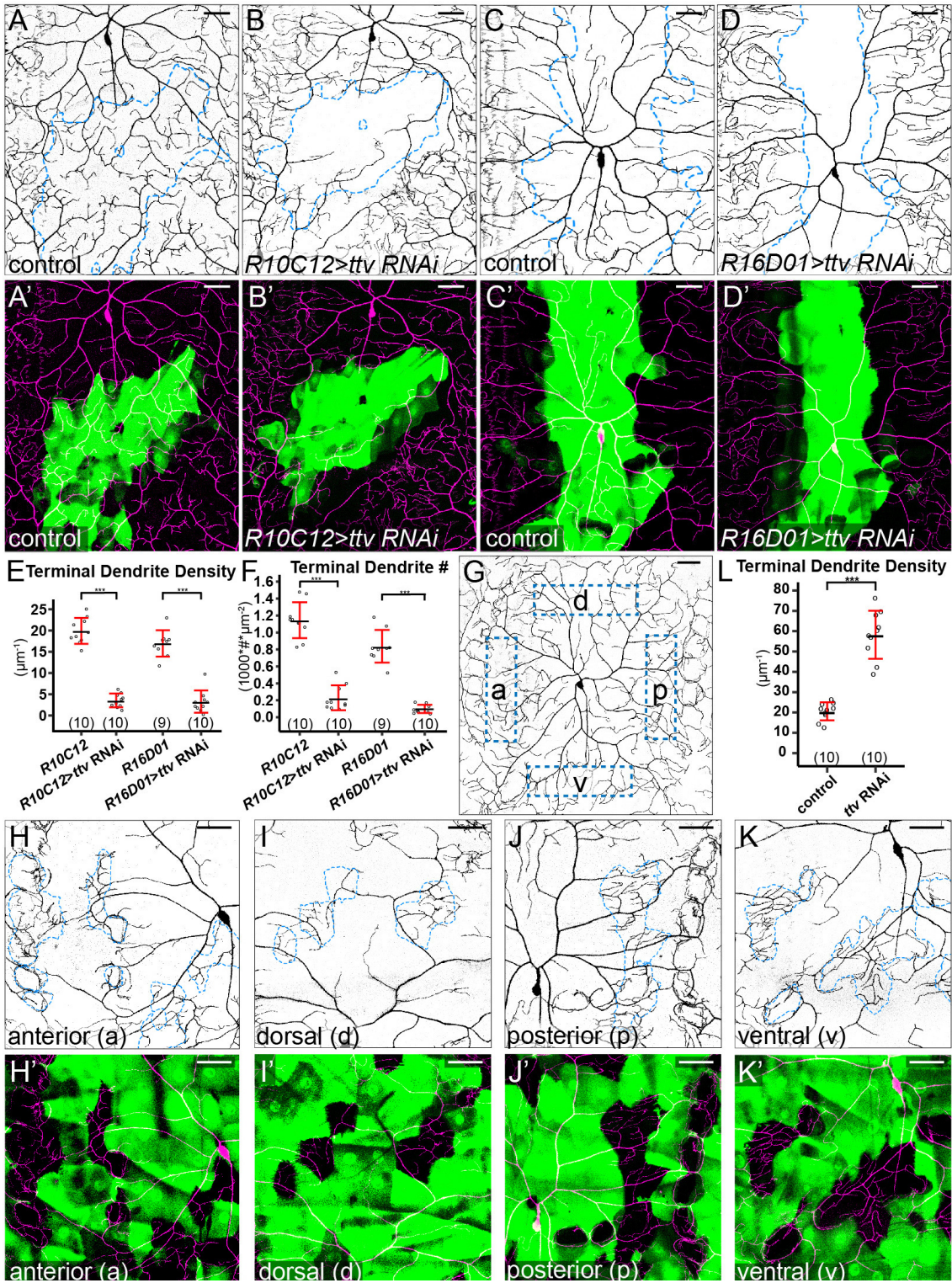
Dendritic growth of C4da neurons does not involve HSPG-mediated transport of diffusible signaling molecules

HSPGs regulate activities of many growth factors and formation of morphogen gradients (16, 17). In particular, HSPGs are necessary for the restricted diffusion of extracellular signaling molecules from signal-producing cells to signal-receiving cells (40-42). Therefore, a plausible model for the role of HSPGs in dendritic growth is that they mediate the action of a signaling molecule that is secreted by a subset of epidermal cells and diffuses along the epithelial sheet. This model has at least two predictions. First, the location of HSPG knockdown relative to the source of the signal should influence the severity of the dendritic growth defect. For example, HSPG knockdown in signal-producing cells should block spreading of the signal and reduce dendritic growth in surrounding wildtype regions. Second, a patch of wildtype epidermal cells completely surrounded by HS-deficient epidermal cells should not receive the signal and hence show reduction of high-order dendrites. To test the first prediction, we knocked down *ttv* in two additional domains in the dendritic field (Figure 2.5A-D'). *R10C12-Gal4* drives expression in a patch of epidermal cells on the lateral body wall that overlaps with the border of *ddaC* and lateral C4da v'ada (Figure 2.5A, A'). *R16D01-Gal4* drives expression in a stripe of epidermal cells in the middle of the segment (Figure 2.5C, C'). Knockdown with either driver caused a strong reduction of terminal dendrites in the RNAi-expressing domains (Figure 2.5E, F) but no apparent dendritic loss in neighboring wildtype regions. These results suggest that the action of the presumptive HSPG-mediated signal is not location-dependent.

To test the second prediction, we generated random epidermal clones that expressed *ttv RNAi* using the 'Flp-out' technique (43). We made a highly efficient epidermal Flipase (Flp) that turns on expression in most epidermal cells and leaves islands of wildtype epidermal cells

completely surrounded by RNAi-expressing cells (Figure 2.5H-K') at various locations in the dendritic field (Figure 2.5G). Surprisingly, terminal dendritic densities significantly increased, rather than decreased, in all wildtype clones surrounded by *ttv RNAi*-expressing cells when compared to similar clones surrounded by wildtype cells (Figure 2.5L). The lack of dendritic reduction in clones surrounded by HS-deficiency strongly suggests that the dendrites do not receive the growth-promoting signal through HSPG-mediated extracellular diffusion. Instead, similar to membrane HSPGs, this signal is likely produced by and associated with every epidermal cell.

Figure 2.5. HSPGs do not promote dendritic growth by transporting diffusible signals. (A-B') DdaC in an *R10C12-Gal4* control (A and A') and an animal expressing *R10C12-Gal4*-driven *ttv RNAi* (B and B'). (C-D') DdaC in an *R16D01-Gal4* control animal (C and C') and an animal expressing *R16D01-Gal4*-driven *ttv RNAi* (D and D'). Blue dots in upper panels outline Gal4-expressing cells and lower panels show Gal4-expressing cells in green and C4da dendrites in magenta. (E and F) Quantification of terminal dendrite density (E) and terminal dendrite number (F). *** $p \leq 0.001$; Student's t-test. (G) DdaC in a control animal with anterior (a), dorsal (d), posterior (p), and ventral (v) locations in the dendritic field indicated. (H-K') DdaC dendrites in animals expressing *ttv RNAi* in random epidermal patches, showing wildtype epidermal cells surrounded by RNAi-expressing epidermal clones in anterior (H and H'), dorsal (I and I'), posterior (J and J'), and ventral (K and K') regions of the dendritic field. Blue dots in upper panels outline wild-type epidermal cells. Lower panels show RNAi-expressing cells in green and C4da dendrites in magenta. (L) Quantification of terminal dendrite density in wild-type epidermal cells surrounded by control and *ttv-RNAi*-expressing epidermal clones. *** $p \leq 0.001$; Student's t-test. For all quantifications, each circle represents a neuron. The numbers of neurons are indicated. Black bar: mean; red bars: SD. Scale bars represent 50 μm . Reagents for these experiments were contributed by Bei Wang. Imaging in A-D' was performed by Lingfeng Tang. Imaging in H-K' was performed by Amy Poe. Quantifications were performed by Lingfeng Tang and Maria Sapar.



Ptp69D but not Lar is required for dendritic growth of C4da neurons

The effects of HSPGs on axonal outgrowth and guidance are mediated by LAR members of the RPTP family in mice, zebrafish, and *Drosophila* (15, 18, 44). Both Sdc and Dlp are known ligands for *Drosophila* Lar (44, 45). We therefore wondered if HSPGs promote C4da dendritic growth by acting together with Lar on the neuronal membrane. Besides Lar, *Drosophila* has another Ig-containing RPTP, Ptp69D. Although Ptp69D belongs to a different class of RPTP from Lar (46), we also tested its role in C4da dendritic growth under the assumption that Ptp69D Ig domains may interact with HS in a similar way to those of Lar. We first examined *Lar* and *Ptp69D* expression by generating transcriptional reporters using the Trojan-exon Gal4 strategy (47). We converted MiMIC cassettes inserted between coding exons of Lar and Ptp69D into *2A-Gal4* insertions (Figure 2.S5A), which are predicted to be spliced into all isoforms and produce in-frame Gal4 proteins. In this way, we generated Gal4 drivers under the endogenous regulatory control of *Lar* and *Ptp69D* loci. Using a membrane marker *UAS-CD4-tdGFP* and a nuclear marker *UAS-RedStinger*, we found that *Lar* is expressed in a subset of epidermal cells and in all classes of da neurons (Figure 2.6A-A''). At the late third instar stage, *Ptp69D* is primarily expressed in C3da and C4da neurons but is also weakly and variably expressed in C1da and C2da neurons (Figure 2.6B-B''). At earlier larval stages, we only observed CD4-tdGFP labeling of C3da and C4da neurons (Figure 2.S5B-B''). The expression patterns of *Lar* and *Ptp69D* suggest that they could play a role in dendrite development of C4da neurons.

To determine if *Lar* and *Ptp69D* are important for dendritic growth of C4da neurons, we generated mutations for each of them using CRISPR/Cas9 (48) (Figure 2.S5A, C). *Lar³* and *Lar¹³* are large deletions that remove parts of the extracellular domain, the transmembrane domain, the first intracellular phosphatase domain, and parts of the second phosphatase domain, and are thus

predicted to be null alleles. *Ptp69D^{l0}* carries an indel that shifts the reading frame in the second phosphatase domain and therefore may behave as a hypomorph. *Ptp69D^{l4}* carries a reading frame-shifting indel in the first extracellular Ig domain and thus is predicted to be null. We generated MARCM clones for *Lar^{l3}* in C4da neurons (Figure 2.6D) but did not detect dendrite defects (Figure 2.6J, S5D, S5E) when compared to the control (Figure 2.6C). *Lar³/Lar^{l3}* trans-heterozygotes (Figure 2.6H) did not show defects in terminal dendrite density (Figure 2.6J) but exhibited slight increases in total dendrite density (Figure 2.S5D) and terminal dendrite numbers (Figure 2.S5E). In contrast, *Ptp69D^{l0}* and *Ptp69D^{l4}* C4da mutant neurons generated by MARCM (Figure 2.6E, F) showed strong reductions of the terminal dendrite density (Figure 2.6K). Trans-heterozygotes of *Ptp69D^{l4}* and *Df(3L)8ex34*, a deficiency that deletes the entire *Ptp69D* locus (49), showed more consistent dendrite reduction (Figure 2.6I, 6K, S5F, S5G). We did not detect statistically significant differences in the terminal dendrite number between wildtype and *Ptp69D* mutant neurons generated by the MARCM technique (Figure 2.S5G), possibly due to the more variable phenotypes of MARCM clones than neurons in the whole-animal mutant. Together, these data demonstrate that Ptp69D, but not Lar, is required for dendrite development of C4da neurons.

Figure 2.6. *Ptp69D* but not *Lar* is necessary for C4da dendritic growth.

(A-A'') *Lar*-expressing cells at 96 hr AEL labeled by *Lar-Gal4*-driven membrane marker CD4-tdGFP and nuclear marker RedStinger. (B-B'') *Ptp69D*-expressing cells at the wandering stage (120 hr AEL) labeled by *Ptp69D-Gal4*-driven CD4-tdGFP and RedStinger. *Ptp69D*-expressing neurons are labeled in (B) and (B'). (C-F) DdaC MARCM clones of wildtype (C) and *Lar^{l3}* (D), *Ptp69D^{l0}* (E), and *Ptp69D^{l4}* (F). Insets show MARCM clones labeled by tdTom (C, D) and mCD8-GFP (E, F). (G-I) DdaC in a control animal (G), a *Lar³/Lar^{l3}* transheterozygote animal (H), and a *Ptp69D^{l4}/Df(3L)8ex34* animal (I). (J and K) Quantification of terminal dendrite density in genotypes indicated. ns, not significant; *** $p \leq 0.001$; ANOVA and Tukey's HSD test. For all quantifications, each circle represents a neuron. The numbers of neurons are indicated. Black bar: mean; red bars: SD. Scale bars represent 50 μm . Molecular cloning of gRNAs was performed by Bei Wang. Imaging and quantifications were performed by Amy Poe.

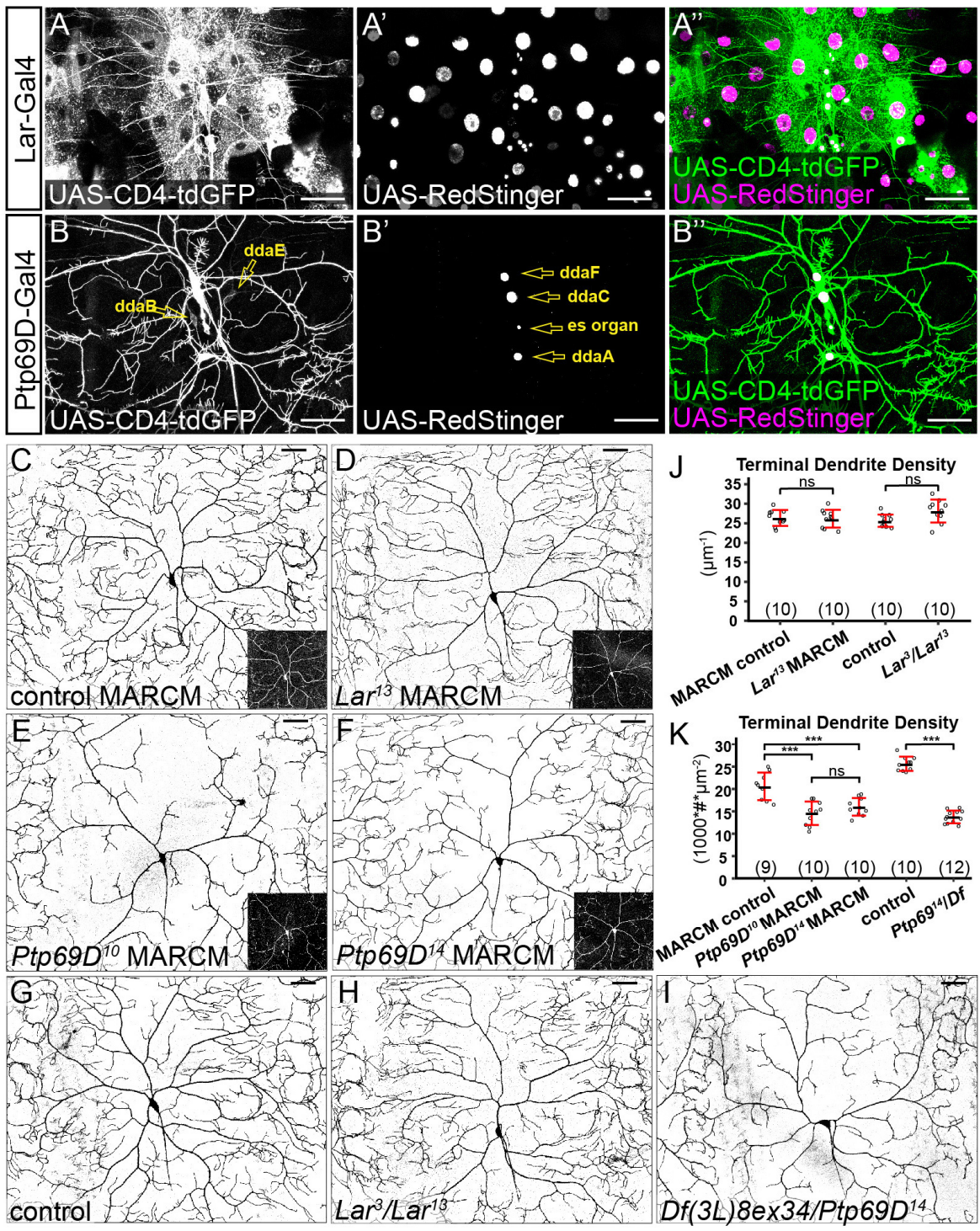
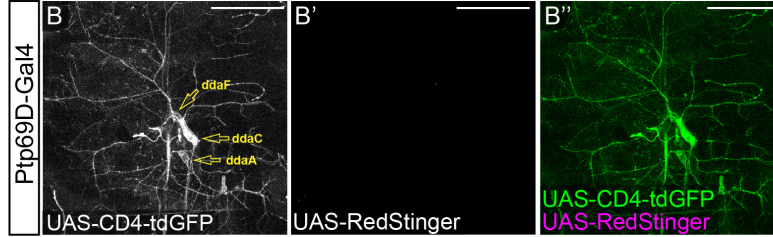
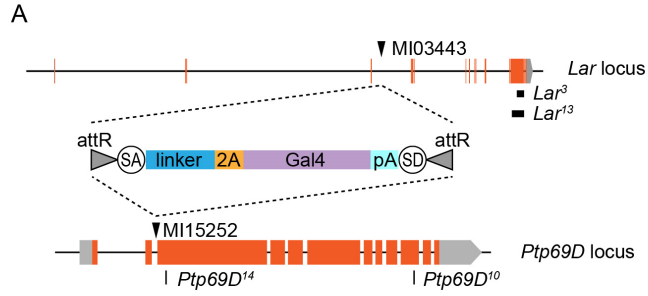


Figure 2.S5. *Lar* and *Ptp69D* reporters, mutations, expressions and LOF phenotypes.

(A) A diagram showing the Trojan Exon structure and MiMIC insertion sites in *Lar* and *Ptp69D* loci. Coding exons are in orange and untranslated regions are in light grey. The splice acceptor (SA) and splice donor (SD) sites allow incorporation of the transgene into the gene's mRNA. The T2A peptide allows two protein products to be made from a single mRNA transcript (63). The black boxes in the *Lar* locus show the locations of CRISPR-induced deletions and the black lines in the *Ptp69D* locus show the sites of the CRISPR-induced indels. (B-B'') Expression of CD4-tdGFP (B) and RedStinger (B') in a *Ptp69D-Gal4 UAS-CD4-tdGFP UAS-RedStinger* larva at 48 hr AEL. (B'') shows the merge of both markers. RedStinger was not expressed in CD4-tdGFP-labeled neurons most likely because the Gal4 expression is very low at this stage and *UAS-CD4-tdGFP* is much more responsive to Gal4 than *UAS-RedStinger* (59). Scale bars represent 50 μm . (C) Sequences of mutations induced by CRISPR/Cas9 in *Lar* and *Ptp69D* loci. The wildtype sequence is shown at the top with the gRNA target site in bold and the PAM sequence in green. The amino acid sequence and position are shown above the wildtype DNA sequence. Deleted residues are shown as dashes and inserted residues are shown in blue lowercase letters. (D and E) Quantification of total dendrite density (D) and terminal dendrite numbers (E) in wildtype, *Lar^{l3}* mutant neurons, and *Lar³/Lar^{l3}* mutant animals. ** $p \leq 0.01$; ns, not significant; one-way analysis of variance and Tukey's HSD test. (F and G) Quantification of total dendrite density (F) and terminal dendrite numbers (G) in wildtype, *Ptp69D^{l0}*, *Ptp69D^{l4}* mutant neurons, and *Ptp69D^{l4}/Df(3L)8ex34* mutant animals. *** $p \leq 0.001$; ns, not significant; one-way analysis of variance and Tukey's HSD test. For all quantifications, each circle represents an individual neuron. The number of neurons for each genotype is indicated. The black bars represent the mean and the red bars represent the standard deviation. Imaging, sequencing, & quantifications were performed by Amy Poe.



C

800 1083 1895 1904

WT S A A I V V K T P G G V P R F K N G L G N M P Q Y K L R E F

Lar¹³ GAGTGTGCGATTGTGGTGA~~AAACTCCTGGCGG~~GAGTACC / /GGTCAAGAACGGATTGGG / /ACATGCCGCAGTATAAGCTGCGTGAATTTA

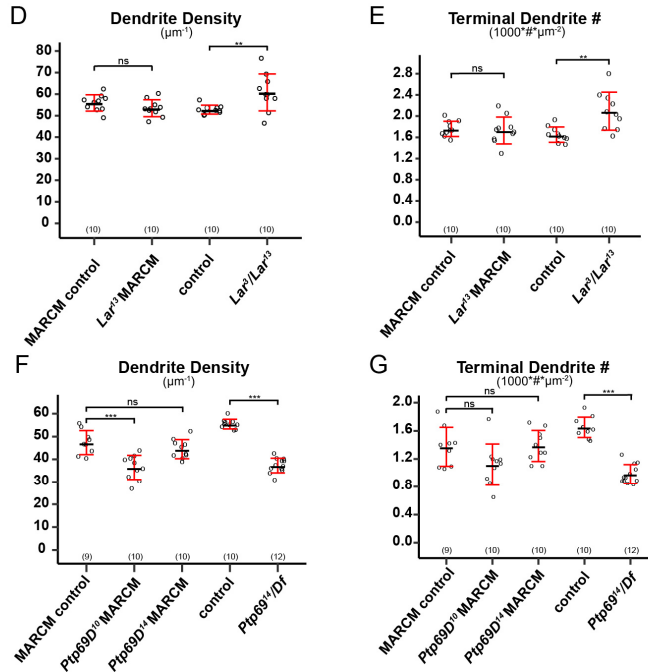
Lar³ GAGTGTGCGATTGTGGTGA----- / /----- / /-----CTGCGTGAATTTA

110 1353 1364

WT Y T C T A Q T G Q N H S T E F Q V D G E V P E V C R G I

Ptp69D⁰ CTACACATGCACAGCCAAACGGGGCAAACCATTCGACTGAATTCCAA / /GTGGACGGAGAAGTTCCTGAAGTCTGCCGTGGCATT

Ptp69D⁴ CTACACATGCACAGCCCAA-----AACCATTCGACTG**ta**tc~~ca~~AA / /GTGGACGGAGAAGTTCCTGAAGTCTGCCGTGGCATT



***Ptp69D* and HSPGs function in separate genetic pathways**

Because both *Ptp69D* and HSPGs are involved in dendrite development of C4da neurons, we next wanted to know whether they function in the same genetic pathway, and in particular, whether *Ptp69D* is the neuronal receptor for epidermal HSPGs in promoting dendritic growth. Because of the lack of a dominant active *Ptp69D* allele that can enhance dendritic growth when over-expressed and the difficulty to simultaneously knock down HSPGs in epidermal cells and express transgenes in C4da neurons, we investigated the epistatic relationship of HSPGs and *Ptp69D* by knocking down epidermal HSPGs in the *Ptp69D* mutant background. If *Ptp69D* is indeed the receptor for HSPGs, the combined loss of HSPGs and *Ptp69D* should be phenotypically similar to the loss of *Ptp69D* alone; but if HSPGs and *Ptp69D* function in separate pathways, loss of both of them should have combined effects. Pan-epidermal knockdown of *sotv* in *Df(3L)8ex34/Ptp69D¹⁴* trans-heterozygotes (Figure 2.7B) exhibited stronger dendrite reductions than either *sotv* RNAi (Figure 2.1B) or *Df(3L)8ex34/Ptp69D¹⁴* (Figure 2.6J) alone, as shown by further reduced terminal dendrite density (Figure 2.7D) and terminal dendrite number (Figure 2.7E). In addition, the average length of terminal dendrites further decreased in the loss of both *Ptp69D* and epidermal *sotv* (Figure 2.7C). Phenotypically, *Ptp69D* mutant neurons in epidermal knockdown of *sotv* exhibited characteristics of wildtype neurons in *sotv* knockdown, such as more crowded dendrites at the MAS (Figure 2.7B), which is not predicted to occur if the HSPG function depends on *Ptp69D*. Therefore, these data show that the loss of both HSPGs and *Ptp69D* has combined effects on dendrite development.

We then tested whether *Ptp69D* requires Ig domains for its function. As RPTPs are known to rely on their Ig domains to interact with HS (18), the Ig domains should be important for *Ptp69D* function if it is the receptor for HSPGs. We compared the ability of a full-length

Ptp69D and a version of *Ptp69D* lacking both Ig domains (50) (*Ptp69D^{ΔIg}*) to rescue C4da dendrite defects in the *Df(3L)8ex34/Ptp69D^{Δ4}* background (Figure 2.7F, G). Neuronal overexpression of *Ptp69D* completely rescued the total dendrite density (Figure 2.7H) and terminal dendrite density (Figure 2.7I), and largely rescued the terminal dendrite number (Figure 2.7J). Surprisingly, *Ptp69D^{ΔIg}* rescued *Ptp69D* mutant neurons as well as did the full-length version (Figure 2.7H-J). These data demonstrate that Ig domains are dispensable for the function of Ptp69D in regulating dendritic growth and are inconsistent with the idea that Ptp69D is a receptor for HSPGs.

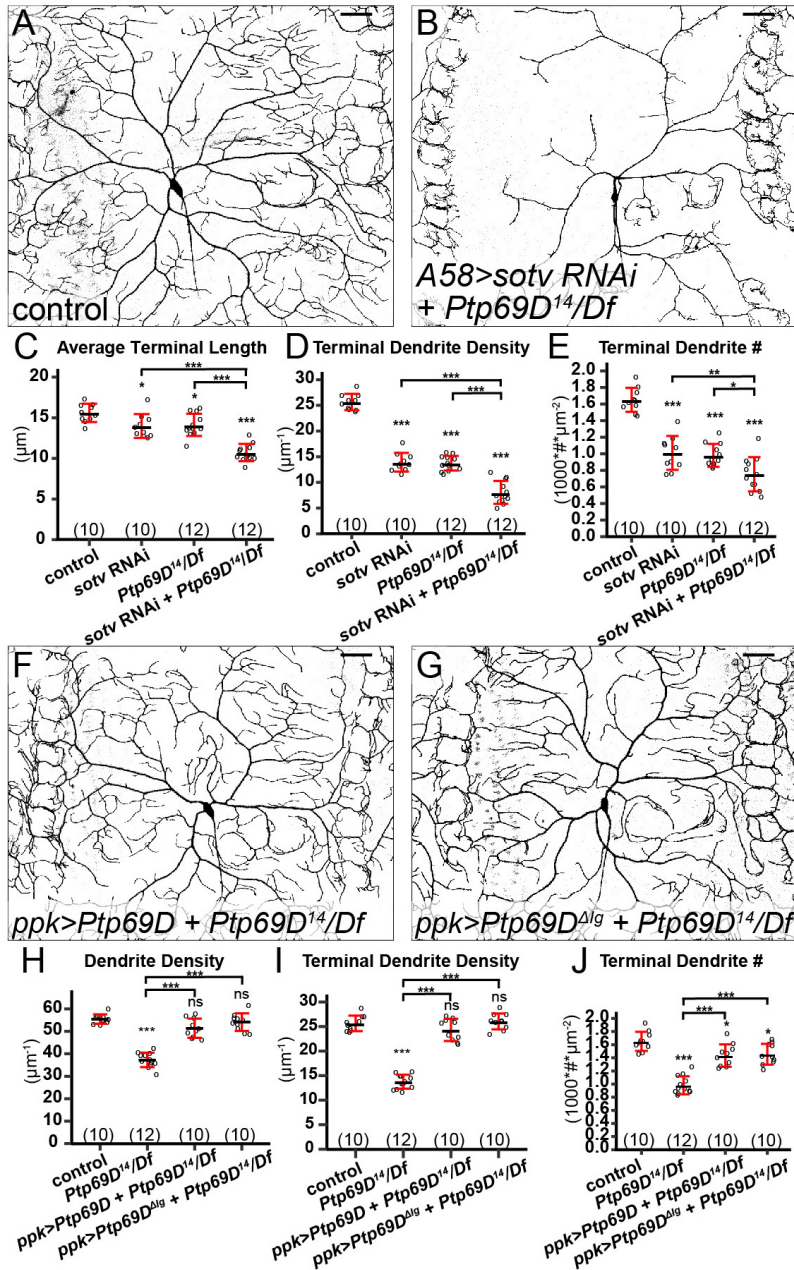


Figure 2.7. HSPGs and *Ptp69D* act in different genetic pathways.

(A and B) DdaC in a *Gal4⁴⁵⁸* control (A) and a *Ptp69D¹⁴/Df(3L)8ex34* animal expressing *Gal4⁴⁵⁸>sotv RNAi* (B). (C-E) Quantification of average terminal length (C), terminal dendrite density (D), and terminal dendrite number (E) in genotypes indicated. (F and G) DdaC in animals expressing *ppk>Ptp69D* (F) and *ppk>Ptp69D Δ Ig* (G) in the *Ptp69D¹⁴/Df(3L)8ex34* background. (H-J) Quantification of total dendrite density (H), terminal dendrite density (I), and terminal dendrite number (J) in genotypes indicated. For all quantifications, ns, not significant; * $p \leq 0.05$; ** $p \leq 0.01$; *** $p \leq 0.001$; ANOVA and Tukey's HSD test. Each circle represents a neuron. The numbers of neurons are indicated. Black bar: mean; red bars: SD. Scale bars represent 50 μm . Imaging and quantifications were performed by Amy Poe.

Finally, we investigated the possibility that Lar and Ptp69D may be redundant in mediating HSPG function. Such a possibility predicts a stronger phenotype in the loss of both *Lar* and *Ptp69D* than that of *Lar* or *Ptp69D* mutant alone. To examine C4da neurons lacking both Ptp69D and Lar, we knocked down *Ptp69D* in the *Lar³/Lar-Gal4* background. The Trojan-exon *Lar-Gal4* is predicted to truncate the *Lar* transcript (Figure 2.S5A) and therefore should behave as a null allele. *Lar³/Lar-Gal4* did not differ from the control, except showing a slight reduction in dendrite density (Figure 2.S6A, B, E-G). *Ptp69D* knockdown by *Lar-Gal4* (Figure 2.S6C, E-G) also mirrored the dendrite reduction phenotype of *Df(3L)8ex34/Ptp69D¹⁴* (Figure 2.7H-J). Importantly, removing *Lar* in addition to *Ptp69D* knockdown did not enhance the dendrite reduction (Figure 2.S6D-G). Combined with the HSPG-Ptp69D epistatic analysis and Ptp69D rescue experiments, these results demonstrate that neither Lar nor Ptp69D is a receptor for HSPGs and Ptp69D regulates C4da dendrite development in a pathway independent of HSPGs.

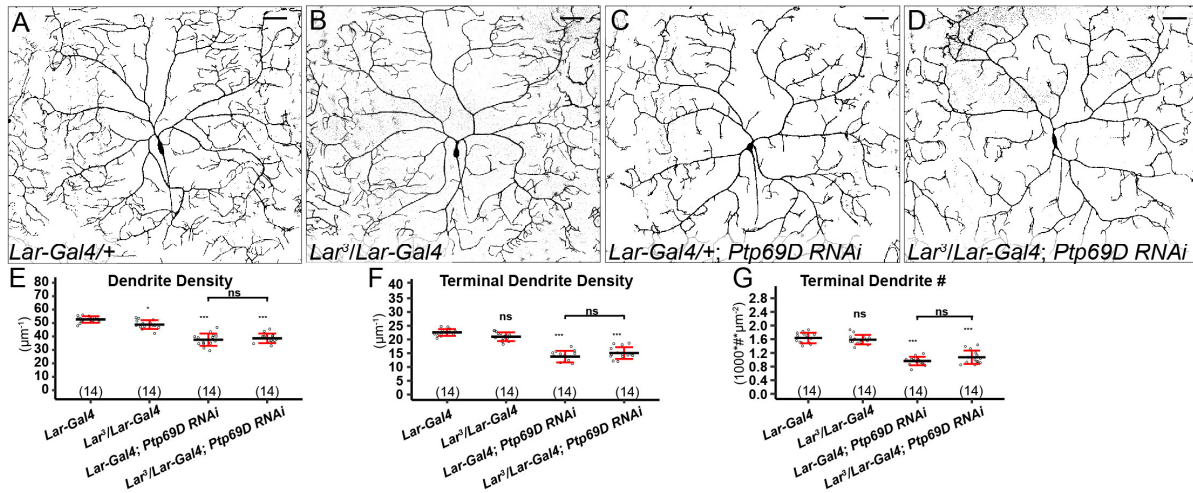


Figure 2.S6. *Lar* and *Ptp69D* do not play redundant roles in dendrite development of C4da neurons.

(A-D) DdaC dendritic fields of an animal expressing *Lar-Gal4* (K), a *Lar3/Lar-Gal4* transheterozygote animal (L), an animal expressing *Lar-Gal4>Ptp69D RNAi* (M), and a *Lar3/Lar-Gal4* transheterozygote expressing *Ptp69D RNAi* (N). (E-G) Quantification of total dendrite density (O), terminal dendrite density (P), and terminal dendrite number (Q) in *Lar-Gal4*, *Lar* mutant animals, *Ptp69D RNAi* animals, and *Lar* mutant animals expressing *Ptp69D RNAi*. *** $p \leq 0.001$; ns, not significant; one-way analysis of variance and Tukey's HSD test. For all quantifications, each circle represents an individual neuron. The number of neurons for each genotype is indicated. The black bars represent the mean and the red bars represent the standard deviation. Scale bars represent 50 μm. Imaging & quantifications were performed by Amy Poe.

DISCUSSION

How neurons interact with substrates to fill a receptive field is an unsolved problem. Previous studies have demonstrated the importance of dendrite spatial restriction and homotypic repulsion in spreading dendrites and preventing branch overlaps of the same neuron (self-avoidance) and neighboring like-neurons (tiling) (6, 23, 51). Although much has recently been learned about molecular mechanisms of dendritic spatial restriction and homotypic repulsion (52-54), the roles of the extracellular microenvironment in space-filling remain poorly understood. In particular, it is unknown whether dendritic innervation of target tissues by space-filling neurons in vivo requires neuronal type-specific extrinsic signals, even though earlier work suggested that RGCs have an intrinsic capacity for establishing space-filling patterns in vitro (3). Here we demonstrate that *Drosophila* space-filling C4da neurons rely on two HSPGs of distinct types, the Syndecan and the glypican Dally, as redundant local permissive signals for their innervation of the skin, while other somatosensory neurons do not require HSPGs for their dendritic growth. Consistent with the neuronal-type specificity, HSPGs stabilize dendritic microtubules and thus dynamic high-order dendritic branches of C4da neurons. Surprisingly, HSPGs promote C4da dendritic growth neither through transporting extracellular diffusible signals nor by interacting with Lar. Interestingly, another RPTP, Ptp69D, regulates the growth of C4da high-order dendrites through an HSPG-independent pathway. Our study, therefore, reveals a novel HSPG-dependent pathway specific for the dendritic growth of space-filling neurons.

A model for HSPG-dependent dendritic growth of spacing-filling neurons

Our results demonstrate that the HS chains of Dally and Sdc on the surface of epidermal cells serve as extracellular permissive signals for dendritic growth of C4da neurons. However, unlike many other contexts in which HSPGs regulate neural development, Lar is not required for

the HSPG-dependent dendritic growth. This observation raises the question whether HS is the sole permissive signal or if it functions together with other extracellular ligands. Our results strongly suggest that for the HSPG-dependent growth, dendrites do not receive morphogen-like molecules that diffuse from specific locations of the epidermis. Consistent with this conclusion, we have failed to rescue the loss of high-order dendrites in HSPG deficiency by epidermal overexpression of many secreted and HS-dependent ligands, including Slit and members of Wnt, BMP, and EGF families. Instead, the cell-autonomous loss of dendrite coverage on HS-deficient epidermal cells indicates that the dendritic growth-promoting signal is present and attached to each individual epidermal cell. Therefore, we propose two possible scenarios (Figure 2.8): (1) the HS chains of Dally and Sdc interact with and activate a novel receptor located on the dendritic membrane; or (2) HS activates a neuronal receptor by acting as a co-ligand for a membrane protein expressed by all epidermal cells or for a secreted molecule that tightly adheres to the epidermal surface by binding HS. In both scenarios, the activation of the neuronal receptor leads to downstream signaling events that stabilize microtubules. Ptp69D regulates dendritic growth in a separate pathway. This model does not exclude the possibility that there may be other diffusible growth factors that can influence the global pattern of the C4da dendritic arbor.

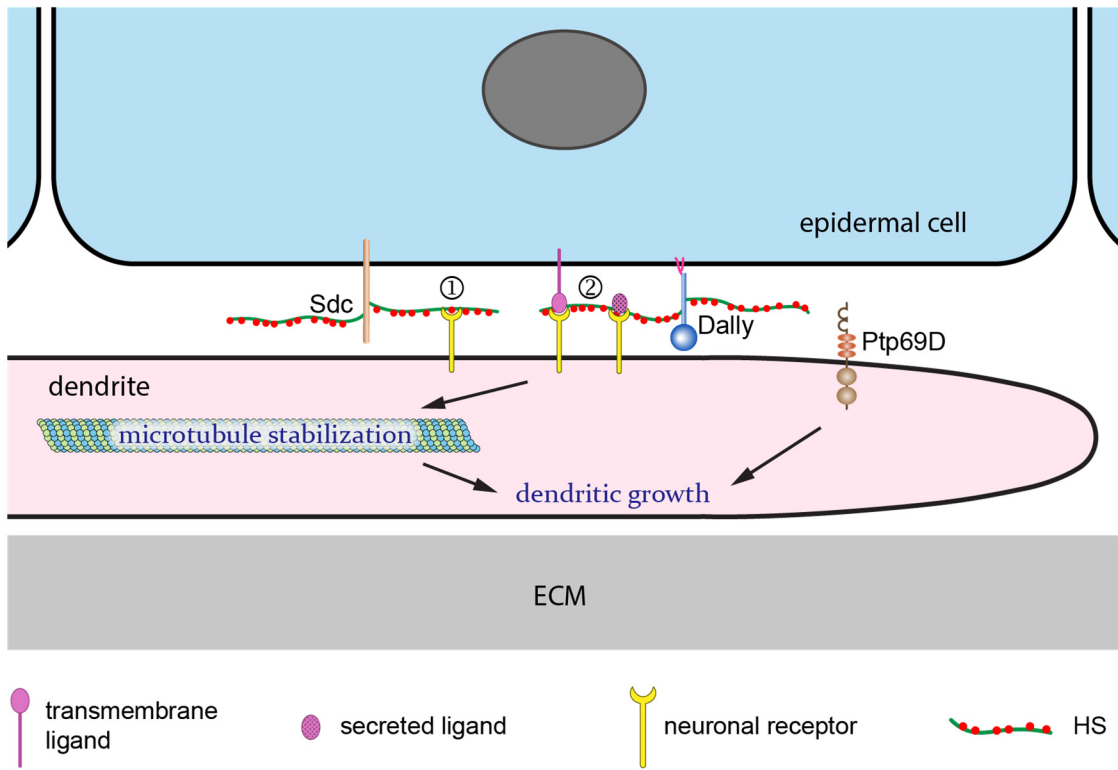


Figure 2.8. A model for the roles of HSPGs and Ptp69D in dendritic growth.

A diagram showing Dally and Sdc and their potential interactions with an unknown ligand and an unknown neuronal receptor. Ptp69D functions in a parallel pathway. See Discussion for details.

The mechanism of neuronal type-specific roles of HSPGs in regulating dendritic growth

An important finding of our study is that HSPGs are specifically required for dendritic growth of C4da neurons. As space-filling neurons, C4da neurons possess highly dynamic high-order dendrites that undergo constant branch turnover. Using a new live imaging method, for the first time we were able to continuously monitor the dynamics of larval da dendrites for more than 10 hours. This method revealed that HSPGs are not required for transient dendritic extension or branching. Instead, HSPGs stabilize newly formed and existing high-order branches and enhance long-term dendritic growth at least partially by promoting microtubule stabilization and bundling. The effects of HSPGs on microtubule bundling may be direct or indirect, and HSPGs may have additional effects on other molecular processes that regulate long-term growth of dendrites, such as actin cytoskeleton stability and vesicular trafficking. Nevertheless, our data suggest that for C4da neurons to expand the dendritic arbor or to fill a receptive field, dendrite stabilization is an essential step.

The *Drosophila* larva has four classes of multi-dendritic da neurons. Unlike C4da neurons, other da classes lack highly branched high-order dendrites and do not fill their receptive fields. During larval development, once the initial dendritic territory is established, the size of dendritic arbors of da neurons expands in proportion with the overall larval body size (25). For non-space filling da neurons, the dendritic arbor maintains its shape and expands mostly by elongating existing dendrites. However, space-filling neurons have to generate new branches to invade the space created during body expansion. Therefore, HSPG-dependent stabilization of newly formed dendrites not only serves as a mechanism for C4da neurons to sense and elaborate dendrites into the correct spatial domain, but may also underlie the neuronal type-specificity of HSPGs in regulating dendritic growth.

Coexistence of space-filling and non-space-filling neurons in the same tissue is also common in vertebrates. For example, basket cells grow sparse dendrites in the molecular layer of the cerebellum, the same tissue where Purkinje cells extend expansive and numerous branched dendritic arbors (55). It will be interesting to find out whether Purkinje cells also require neuronal type-specific permissive signals for arbor growth.

Cell non-autonomous increase of dendrites induced by HSPG deficiency

Our experiments also revealed an unexpected cell non-autonomous increase of dendrites induced by HSPG deficiency. Knockdown of *ttv* in the *hh* domain caused an increase of dendrites on epidermal cells anterior to the *hh* domain (Figure 2.1P). Similarly, wildtype epidermal clones completely surrounded by *ttv RNAi*-expressing epidermal cells showed higher terminal dendrite density than similar clones surrounded by wildtype epidermal cells (Figure 2.5L). In addition, pan-epidermal knockdowns of *sotv*, *ttv*, and *sfl* by *Gal4^{A58}* all led to increases of dendrites at muscle attachment sites (Figure 2.1B, S1B, S1C). These results demonstrate that when innervation in one spatial domain is blocked by HS loss, the dendrite density is increased in nearby permissive domains. A tantalizing interpretation is that C4da neurons may have an intrinsic ‘drive’ to elaborate a certain length of dendrites and the lack of dendrites in HS-deficient zones is compensated by dendrite increase in other areas. We found that neurons lacking dendrite coverage in the *hh* domain, or in the middle of the segment (driven by *R16D01-Gal4*), as a result of HS deficiency are similar to Gal4-only control neurons in total dendrite lengths, supporting this hypothesis. Two other possible mechanisms may also explain the results. In the first one, HS loss in one epidermal region may somehow increase the concentration of the dendrite growth-promoting signal on neighboring wildtype epidermal cells. In the second, HS-deficiency may trap intracellular dendrite growth-promoting organelles, such as Golgi outposts

(9), to dendrite segments covering nearby wildtype epidermal cells. It will be interesting to distinguish these possibilities in the future.

Conserved and diverse roles of HSPGs in insect and vertebrate space-filling neurons

C4da neurons are analogous to the trigeminal sensory neurons and Rohon-Beard neurons of zebrafish in that they are all space-filling somatosensory sensory neurons that innervate the skin (4, 14). Consistent with the conclusion that HSPGs play a permissive, but not instructive, role, C4da dendrites do not misroute to other areas in the absence of HSPGs. Instead, they can extend and branch into HS-deficient zones but fail to be stabilized. In contrast, HSPGs seem to play a different role in axonal morphogenesis of zebrafish space-filling neurons: they function as attractants to direct growing sensory axons of Rohon-Beard (RB) neurons to the skin, and loss of HS in the skin leads to misrouting of axons to internal tissues (15). This apparent difference may be related to zebrafish neurons having alternative but disfavored substrates (i.e. internal tissues), whereas *Drosophila* C4da neurons cannot innervate tissues other than the epidermis. To some extent, the increase of C4da dendrites outside the HS-deficient zone may be seen as resembling the misrouting phenotype of zebrafish RB neurons.

On the other hand, the pathways through which HSPGs regulate neurite outgrowth of *Drosophila* C4da neurons and zebrafish RB neurons are clearly distinct. Zebrafish RB neurons express two LAR homologs, PTPRFa and PTPRFb, which act as redundant receptors for HS to control the guidance of sensory axons (15). The interaction between these LAR proteins and extracellular HS is essential as mutations of the HS-interaction motif in the Ig domains of the LARs abolish their ability to respond to HS (15). In contrast, the *Drosophila* Lar does not play a detectable role in dendritic growth of C4da neurons. Although the Ig-containing RPTP Ptp69D is expressed in da neurons and is required for high-order dendritic growth of C4da neurons, it does

not function in the same pathway as HSPGs. Therefore, it appears that HSPGs can regulate neurite growth of different types of space-filling neurons through different downstream signaling pathways. These similarities and distinctions raise several interesting questions. First, does the HSPG-PTPRFa/PTPRFb pathway control axon guidance of RB neurons through stabilizing microtubules in selective branches? Second, do HSPGs regulate space filling independent of LAR proteins in other neuronal systems? Lastly, do HSPGs play any role in neurite growth of vertebrate non-space-filling neurons that exhibit dynamic branch turnover? Answering these questions will broaden our understanding of the roles the extracellular microenvironment plays in neuronal morphogenesis.

ACKNOWLEDGMENTS

We thank Xinhua Lin, Yuh Nung Jan, Hiroshi Nakato, Chi-Hon Lee, Kai Zinn, Benjamin White, Jill Wildonger, Bloomington Stock Center, Kyoto Stock Center, and Vienna *Drosophila* Resource Center (VDRC) for fly stocks; Developmental Studies Hybridoma Bank (DSHB) for antibodies; Gerald Rubin, Thomas Kornberg, Addgene for plasmids; Halocarbon Products Corporation for Halocarbon oils; Scott Emr, Mariana Wolfner, Joe Fetcho for critical reading and suggestions on the manuscript. This work was supported by a start-up fund from Cornell University and NIH grant (R01 NS099125) to C.H.

SI Movies (Available Online)

Movie S1. Long-term time-lapse imaging of C4da dendrites in the presence of an HS-deficient zone.

Long-term time-lapse imaging of C4da dendrites at the dorsal midline of an animal expressing *Gal4^{hh}>ttv RNAi* starting from 72 hr AEL. The time (HH:MM) relative to the first frame is indicated for each frame. The border between wildtype (left) and RNAi-expressing (right)

epidermal cells is indicated with a cyan line for each frame. This work was contributed by Lingfeng Tang.

Movie S2. Long-term time-lapse imaging of C4da dendrites in the presence of an HS-deficient zone and wildtype empty space.

Long-term time-lapse imaging of C4da dendrites at the dorsal midline of an animal expressing *Gal4^{hh}>ttv RNAi* starting from 72 hr AEL. The ddaC neuron from the right side (on the top in the frame) of the larva was ablated by laser at 60 hr AEL. The time (HH:MM) relative to the first frame is indicated for each frame. The border between wildtype (left) and RNAi-expressing (right) epidermal cells is indicated with a cyan line for each frame. This work was contributed by Lingfeng Tang.

METHODS

Live imaging

Snapshot live imaging of dendritic morphology of da neurons was performed as described previously (23). For long-term time-lapse imaging, larvae at the right stage were glued to a coverslip using a UV-sensitive glue (Norland NOA 61) and then mounted on a chamber constructed with aluminum. See SI Methods for details of fly stocks, molecular cloning, generation of CRISPR mutants and transcription reporters, MARCM, RNAi, immunohistochemistry, live imaging, image analysis and quantification.

Fly Stocks

Gal4^{hh} (41), *Gal4^{A58}* (56), *Gal4^{en}* (41), *ttv⁶³* (57), *Act5C>y⁺>Gal4* (42), *tubP-Gal80^{ts}* (34), *UAS-DSulf1-Golgi* (33), *UAS-dlp-GFP* (58), *UAS-CD4-tdGFP* (59), *UAS-dcr2* (23), *vkg-GFP* (23), *UAS-mCherry-Jupiter* (60), and *ppk-EB1-GFP* (39) have been described previously. *UAS-Sdc-RNAi* was a gift from Xinhua Lin. *UAS-mIFP-2A-HOI* was a gift from Yuh Nung Jan. *NompC-*

LexA::p65 (#52240), *Df(3L)8ex34* (50), *UAS-Ptp69D-myc* (50), *UAS-Ptp69D-ΔIg* (50), *UAS-RedStinger* (#8547), *Nrg-GFP* (#6844), *R10C12-Gal4* (#47841), *R16D01-Gal4* (#48722), *nos-Cas9* (#54591), *UAS-Ptp69D-RNAi* (#29462) were obtained from Bloomington Stock Center (BDSC). *UAS-ttv-RNAi* (v4871), *UAS-sotv-RNAi* (v4902), *UAS-botv-RNAi* (v37186), *UAS-sfl-RNAi* (v5070), *UAS-dally-RNAi* (v14136), and *UAS-dlp-RNAi* (v10298) were obtained from Vienna *Drosophila* Resource Center (VDRC). *Sdc-GFP* (#109775), *dally-YFP* (#115064), *Dlp-YFP* (#115031) were obtained from *Drosophila* Genomics and Genetic Resources Center (DGRC).

We used the following neuronal markers to label specific classes of da neurons: *ppk-CD4-tdGFP* (59) and *ppk-CD4-tdTom* (23) for C4da; *R10D05-CD4-tdTom* (this study) for C1da; *R20C11-CD4-tdGFP* (this study) for C2da; *NompC-LexA::p65 LexAop-CD4-tdTom* (this study) for C3da. To generate MARCM and Flp-out clones in the epidermis, we created *zk-Flp* which is active in epidermal progenitor cells. To monitor microtubule bundling in da neuron dendrites, we made *LexAop-GFP-Jupiter*.

Molecular cloning

R10D05-CD4-tdTom: The R10D05 enhancer was PCR amplified from R10D05-Gal4 (BDSC #48438) genomic DNA using primers

ggggACAAGTTTGTACAAAAAAGCAGGCTGCAACGGACCTCTTGTATATGGAC and

ggggACCACTTTGTACAAGAAAGCTGGGTGGTTTCGGATTGAAAGTAACCCTGG. The

resulting DNA fragment was used to create an entry vector through a Gateway BP reaction

(Thermo Fisher Scientific). The entry vector was then combined with pDEST-HemmarR (59) to

generate pR10D05-CD4-tdTom expression vector through a Gateway LR reaction.

R20C11-CD4-tdGFP: An entry vector containing R20C11 enhancer (a gift from Gerald Rubin) was combined with pDEST-HemmarG (59) to generate pR20C11-CD4-tdGFP expression vector through a Gateway LR reaction.

zk-Flp: An entry vector was first constructed to contain *zen* VR element (61) and two copies of *kr* AD1 element (62) in tandem. The *zen* VR element was amplified from *w¹¹¹⁸* genomic DNA using primers atatGGTACCCATACTTAGCCCATATTTCCGTC and aataGCTAGCGGATTCAGAGCTTGGTTTTCC; the *kr* AD1 element was amplified from *w¹¹¹⁸* genomic DNA using primers ttttctagaGTTTTTCCTATTGCACCACACTC and ttttGCTAGCTCCACGCCTTTTTGTTTCTG. A destination vector pDEST-APIC-Flp1 was then constructed by replacing CD4-tdTom (XhoI/XbaI) fragment in pDEST-HemmarR with Flp1 coding sequence. Flp1 was amplified by PCR from plasmid pJFRC150-20XUAS-IVS-Flp1::PEST (Addgene #32132) using primers TTATCCTTTACTTCAGGCGGC and aattTCTAGATTAAATACGGCGATTGATGTAGGAGC and then digested by XhoI and XbaI. The entry vector was then combined with pDEST-APIC-Flp1 to make *pzk-Flp1* expression vector through a Gateway LR reaction.

LexAOP-CD4-tdTom: A 13xLexAop2 fragment was released from pJFRC19-13XLexAop2-IVS-myr::GFP (Addgene #26224) by digesting with HindIII (blunted by T4 polymerase) and SpeI. It was then used to replace the KpnI (blunted by T4 polymerase)/NheI fragment of pDEST-APPHIH (59). The resulting plasmid was then digested by XhoI/PacI and re-ligated with the XhoI/PacI fragment (containing CD4-tdTom coding sequence) released from pDEST-HemmarR to make the final construct pAPLO-CD4-tdTom.

LexAOP-GFP-Jupiter: pAPLO-CD4-tdTom was digested with BglII and AscI and then re-ligated after blunting in order to remove an XbaI site 5' to 13X LexAop. The resulting plasmid

was digested by XhoI and XbaI and assembled with a superfolder GFP (sfGFP) PCR fragment and a Jupiter PCR fragment through 3-fragment Gibson Assembly (NEBuilder HiFi DNA Assembly kit). The sfGFP fragment was amplified from pBS-sfGFP (a gift from Thomas Kornberg) using primers cagttcaattacagctctcgagaaatcaaaATGTCCAAGGGCGAGGAGC and agagatcatCGAGCCACCACCGCCACT. The Jupiter fragment was amplified from *UAS-mCherry-Jupiter* (a gift from Chi-Hon Lee) genomic DNA using primers gtggctcgATGATCTCTAACTTTGATTGCACCG and ctggcttagttaattaattctagaTTACCACAGGCCCGACGA.

The above constructs were injected in-house or by Rainbow Transgenic Flies to transform flies through either P-element mediated transformation or ϕ C31 integrase-mediated transformation.

Generation of *Lar* and *Ptp69D* transcription reporters using Trojan exons

Gal4 transcriptional reporters were generated using the previously described *in vivo* Trojan-MiMIC system (47). Briefly, MiMIC lines for *Lar* (MI03443) and *Ptp69D* (MI15252) were crossed to flies with the triplet Trojan donor construct. The progeny of this cross were then crossed to females expressing Cre recombinase and Φ C31 integrase in the germline which allow the Trojan exons to replace the MiMIC attP cassettes. Progeny were then crossed to *UAS-GFP* for screening Gal4 expression by fluorescence microscopy. Adults positive for GFP expression were used to establish the line. The 2A-Gal4 insertions from established lines were sequenced to confirm the accuracy of the sites and reading frames.

Generation of *Lar* and *Ptp69D* mutations through CRISPR/Cas9

We first generated two transgenic fly strains each expressing two gRNAs driven by U6 promoters for targeting either *Lar* or *Ptp69D*. The transgenic gRNA constructs were similar to pCFD4-U6.1_U6.3 (48) except that the selection marker is mini-white. The targeting sequences

are AATTCACGCAGCTTATACTGCGG and ATTGTGGTGAAAACCTCCTGGCGG for *Lar* and ACACATGCACAGCCCAAACGGGG and GAAGTTCCTGAAGTCTGCCGTGG for *Ptp69D* (the PAM sequences are underlined). The constructs were injected by Rainbow Transgenic Flies to transform attP docker lines using ϕ C31 integrase-mediated transformation, with *gRNA-Lar* inserted to *attP^{VK19}* and *gRNA-Ptp69D* inserted to *attP^{VK27}*.

CRISPR-induced mutations were generated by crossing *gRNA-Lar* and *gRNA-Ptp69D* to *y nos-Cas9 w; FRT^{G13} FRT^{42D}; Tm2/Tm6B* and *y nos-Cas9 w; Sp/CyOweep; FRT^{2A} FRT^{80B}* females, respectively. Male progeny containing *nos-Cas9*, *gRNA*, and *FRT* sites were crossed to balancers to separate FRT chromosomes potentially carrying indel mutations. The progeny containing balanced FRT chromosomes were individually crossed to deficiencies uncovering *Lar* or *Ptp69D* to screen for noncomplements. The mutations recovered from the screens were then determined by sequencing. The sequences of both the *Lar* and *Ptp69D* mutant alleles are shown in Figure 2.S5C. *Lar³* carries a deletion of amino acids 1085 to 1899 and *Lar¹³* carries a deletion of amino acids 806 to 1901; *Ptp69D¹⁰* has a deletion of 2 nucleotides at amino acids 1360 and 1361 causing a frameshift mutation and *Ptp69D¹⁴* has a deletion of amino acids 116 to 118 and insertion of TATCCA at amino acids 123 and 124.

Generation of MARCM and Flp-out clones

MARCM analysis of *ttv⁶³* was performed by crossing *ttv⁶³ FRT^{G13}; zk-Flp ppk-CD4-tdTom* with *tub-Gal80 FRT^{G13}; tub-Gal4 UAS-CD8-GFP* to generate marked *ttv⁶³* epidermal clones.

MARCM analysis of *Lar¹³* was performed by crossing *Lar¹³ FRT^{G13}; ppk-CD4-tdGFP* males with *SOP-Flp; tub-Gal80 FRT^{G13}; n-syb-Gal4 UAS-tdTom* (a gift from Yuh Nung Jan) females to generate marked neurons mutant for *Lar*. MARCM analysis of *Ptp69D* mutations was performed by crossing *ppk-CD4-tdTom; Ptp69D¹⁰* (or *Ptp69D¹⁴*) *FRT^{2A}* flies with *Gal4^{elav} UAS-mCD8-GFP*

SOP-Flp; tubP-Gal80 FRT^{2A} (a gift from Yuh Nung Jan) flies to generate marked neurons mutant for *Ptp69D*. Wildtype MARCM clones in the epidermis or in da neurons were generated using wildtype FRT chromosomes.

Flp-out clones in the epidermis was generated by crossing *ppk-spGFP11-CD4-tdTom Act5c>y⁺>Gal4 UAS-EGFP; zk-Flp UAS-Dcr-2* flies with *UAS-ttv-RNAi* or *w¹¹¹⁸* (as the control).

RNAi

RNAi knockdown of *ttv*, *sotv*, *botv*, *sfl* in epidermal cells was carried out with *ppk-CD4-tdTom UAS-dcr2; Gal4^{hh} UAS-EGFP* and *ppk-CD4-tdTom UAS-dcr2; Gal4^{A58}*. RNAi knockdown of *ttv* in different epidermal domains was carried out with *ppk-CD4-tdTom UAS-dcr2; R10C12-Gal4 UAS-mIFP-2A-HO1* and *ppk-CD4-tdTom, UAS-dcr2; R16D01-Gal4 UAS-mIFP-2A-HO1*. *UAS-mIFP-2A-HO1* and *UAS-GFP* were used to label RNAi-expressing epidermal cells. *ppk-CD4-tdTom* was used to label C4da neurons. RNAi knockdown of *dally*, *dlp*, and *Sdc* (individually and in combination) was carried out with *ppk-CD4-tdTom UAS-dcr2; Gal4^{hh} UAS-EGFP*. The effectiveness of *dlp* RNAi was determined by crossing *UAS-dlp-GFP; UAS-dlp-RNAi* flies with *ppk-CD4-tdTom UAS-dcr2; Gal4^{hh} UAS-mIFP-2A-HO1* flies. The effectiveness of *dally* RNAi was determined by crossing *Gal4^{en}; dally-YFP* flies with *UAS-dally-RNAi* flies. The effectiveness of *Sdc* RNAi was determined by crossing *Sdc-GFP; UAS-Sdc-RNAi* flies with *ppk-CD4-tdTom UAS-dcr2; Gal4^{hh} UAS-mIFP-2A-HO1* flies. For RNAi knockdown of *Ptp69D*, either *UAS-Ptp69D-RNAi* or *Lar³/CyOweep; UAS-Ptp69D-RNAi/Tm6B* was crossed to *Lar-Gal4; ppk-CD4-tdTom UAS-dcr2*.

For C1da and C2da neurons, we use *UAS-dcr2; Gal4^{A58}* for pan-epidermal expression of *ttv* RNAi and use *R10D05-CD4-tdTom* and *R20C11-CD4-tdGFP* to label C1da and C2da

neurons, respectively. For C3da neurons, we used *NompC-LexA::p65 LexAOP-CD4-tdTom* to label C3da neurons and *Gal4^{hh} UAS-mIFP-2A-HOI* to express *ttv* RNAi.

Immunohistochemistry

Antibodies used in this study are mouse anti-Mys (DSHB CF.6G11, 1:100), mouse anti-Futsch (DSHB 22C10, 1:100), and mouse anti-heparan sulfate mAb F69-3G10 (Amsbio, 1:100).

Secondary antibodies conjugated to DyLight dyes (Jackson ImmunoResearch) were used at 1:400 dilution. Immunostaining of *Drosophila* larvae was performed as previously described (23). Briefly, 3rd instar larvae were dissected in cold PBS, fixed in 4% formaldehyde/PBS for 30 min at room temperature, and stained with the proper primary antibodies and subsequent secondary antibodies, each for 2 hr at room temperature. HS staining was performed as described previously (57). Briefly, larval fillets were incubated with 500 mU/ml heparinase III (Sigma) in 50 mM Tris-HCl (pH 7.2), 100 mM NaCl, 1 mM CaCl₂, 0.1% Triton-X100, 5 mg/ml BSA for 6 hours at 37°C. Then, larval fillets were stained with primary (F69-3G10) and secondary antibodies.

Long-term time-lapse live imaging

Larvae at appropriate age were anesthetized by isoflurane for 2min. Each larva was then placed on a PDMS block. The PDMS block is 2mm wide, 8mm long, 2mm thick, with a groove in the center (2mm wide, 0.1-0.3mm thick, depending on the size of larvae). Six larvae/PDMS were mounted per coverslip. A small amount of UV glue (Norland glue NOA61) was then added to the two sides of PDMS (about 0.2ul) and the dorsal side of larvae (0.05-0.1ul). After that, a coverslip was placed on top of the PDMS and larvae. The coverslip was pressed slightly, so that the PDMS provide a weak pressure to keep larvae in place. Then, glue was cured by UV light (a modified version of WorkStar® 2003 NDT 365nm UV-A Inspection Light) at Hi setting for 4-

6min when the larvae were 5cm away from the UV light. Next, the coverslip with PDMS and larvae was placed on and glued to a home-made aluminum chamber which was used for providing ventilation and maintaining moisture. The chamber has two holes drilled on the side and contained a small piece of Kimwipe soaked with water during the imaging. Time-lapse imaging was performed on a Leica SP8 confocal at different time intervals. For ablation experiments, da neurons in the A2, A4, and A6 segments on the right dorsal side of larvae at 48-60 hr AEL with appropriate genotypes were ablated using a two-photon laser on a Zeiss 880 confocal microscope. The larvae were then recovered on grape agar plates for 8hrs before mounting and imaging on the chamber. For imaging short-term dynamics of dendrites, 3-min time intervals were used. For neurons expressing GFP-Jupiter, 5-hr time intervals were used to minimize phototoxicity.

For time-lapse imaging of EB1-GFP, primary dendrites in the *hh*-domain were imaged with a 40x NA1.3 oil objective at digital zoom 2.5. Each time-lapse series lasted 5 min with a 2 sec time interval. 10 and 12 positions from 8 larvae were imaged for control and RNAi-expressing animals, respectively.

Image analysis and quantification

For tracing and measuring C4da and C3da dendrites in Fiji/ImageJ, images of dendrites (1024 x 1024 px) taken with a 20X objective were first processed by Gaussian Blur (Sigma: 0.8) and then Auto Local Threshold (Phansalkar method, radius: 50). Isolated particles below the size of 120 pixels were removed by the Particles4 plugin (<http://www.mecourse.com/landinig/software/software.html>). The dendrites were then converted to single-pixel-width skeletons using the Skeletonize (2D/3D) plugin and processed using Analyze Skeleton (2D/3D) plugin. The length of skeletons was calculated based on pixel

distance; terminal dendrites in the dendritic field or regions of interest were counted based on the endings of terminal dendrites. Skeletons of terminal dendrites in regions of interest were isolated using the Strahler Analysis plugin (http://imagej.net/Strahler_Analysis). Dendrite density was calculated using the formula: $1000 \times \text{dendritic length } (\mu\text{m}) / \text{dendritic area } (\mu\text{m}^2)$; normalized terminal dendrite number was calculated using the formula: $1000 \times \text{terminal dendrite number} / \text{dendritic area } (\mu\text{m}^2)$. For C1da and C2da neurons, dendrite tracing and measuring were done using the Simple Neurite Tracer plugin and the total dendritic lengths were presented. The dynamics of EB1-GFP comets were analyzed using the KymographBuilder plugin. Comet speed was defined as distance the comet moved (μm) per second. Comet speed was calculated using the formula: $\text{total number of comets} / (\text{length of the dendrite } (\mu\text{m}) \times \text{imaging time (5 min)})$. R was used to conduct statistical analyses and generate graphs.

Dendrite endings in time-lapse images were identified using the OpenCV library and a custom-written Python script. Each still frame was first processed by Gaussian Blur (ksize: 5) and then Binary Threshold (thresh: 30). Feature points were subsequently identified using Shi-Tomasi Corner-Detection (maxCorners: 500, qualityLevel: 0.1, minDistance: 4, useHarrisDetector: False) and the endings were determined by examining the local topology in the vicinity of each feature point. To follow the movements of the endings, Lucas-Kanade Optical Flow analysis (winSize: 5x5, maxLevel: 0, maxCount: 10, epsilon: 0.03) was conducted and a distance threshold of 5 pixels was used to merge the displaced endings in each frame with the endings in the subsequent frame.

REFERENCES

1. Fujishima K, Horie R, Mochizuki A, & Kengaku M (2012) Principles of branch dynamics governing shape characteristics of cerebellar Purkinje cell dendrites. *Development* 139(18):3442-3455.

2. Panico J & Sterling P (1995) Retinal neurons and vessels are not fractal but space-filling. *J Comp Neurol* 361(3):479-490.
3. Montague PR & Friedlander MJ (1989) Expression of an intrinsic growth strategy by mammalian retinal neurons. *Proc Natl Acad Sci U S A* 86(18):7223-7227.
4. Sagasti A, Guido MR, Raible DW, & Schier AF (2005) Repulsive interactions shape the morphologies and functional arrangement of zebrafish peripheral sensory arbors. *Curr Biol* 15(9):804-814.
5. Grueber WB, Ye B, Moore AW, Jan LY, & Jan YN (2003) Dendrites of distinct classes of Drosophila sensory neurons show different capacities for homotypic repulsion. *Curr Biol* 13(8):618-626.
6. Grueber WB & Sagasti A (2010) Self-avoidance and tiling: Mechanisms of dendrite and axon spacing. *Cold Spring Harb Perspect Biol* 2(9):a001750.
7. Grueber WB, Jan LY, & Jan YN (2003) Different levels of the homeodomain protein cut regulate distinct dendrite branching patterns of Drosophila multidendritic neurons. *Cell* 112(6):805-818.
8. Jinushi-Nakao S, *et al.* (2007) Knot/Collier and cut control different aspects of dendrite cytoskeleton and synergize to define final arbor shape. *Neuron* 56(6):963-978.
9. Ye B, *et al.* (2007) Growing dendrites and axons differ in their reliance on the secretory pathway. *Cell* 130(4):717-729.
10. Satoh D, *et al.* (2008) Spatial control of branching within dendritic arbors by dynein-dependent transport of Rab5-endosomes. *Nat Cell Biol* 10(10):1164-1171.
11. Zheng Y, *et al.* (2008) Dynein is required for polarized dendritic transport and uniform microtubule orientation in axons. *Nat Cell Biol* 10(10):1172-1180.
12. Peng Y, *et al.* (2015) Regulation of dendrite growth and maintenance by exocytosis. *J Cell Sci* 128(23):4279-4292.
13. Lin WY, *et al.* (2015) The SLC36 transporter Pathetic is required for extreme dendrite growth in Drosophila sensory neurons. *Genes Dev* 29(11):1120-1135.
14. Dong X, Shen K, & Bulow HE (2015) Intrinsic and extrinsic mechanisms of dendritic morphogenesis. *Annu Rev Physiol* 77:271-300.
15. Wang F, Wolfson SN, Gharib A, & Sagasti A (2012) LAR receptor tyrosine phosphatases and HSPGs guide peripheral sensory axons to the skin. *Curr Biol* 22(5):373-382.
16. Lin X (2004) Functions of heparan sulfate proteoglycans in cell signaling during development. *Development* 131(24):6009-6021.
17. Sarrazin S, Lamanna WC, & Esko JD (2011) Heparan sulfate proteoglycans. *Cold Spring Harb Perspect Biol* 3(7).
18. Coles CH, *et al.* (2011) Proteoglycan-specific molecular switch for RPTPsigma clustering and neuronal extension. *Science* 332(6028):484-488.
19. Stoker AW (2015) RPTPs in axons, synapses and neurology. *Semin Cell Dev Biol* 37:90-97.
20. Van Vactor D, Wall DP, & Johnson KG (2006) Heparan sulfate proteoglycans and the emergence of neuronal connectivity. *Curr Opin Neurobiol* 16(1):40-51.
21. Liang X, Dong X, Moerman DG, Shen K, & Wang X (2015) Sarcomeres Pattern Proprioceptive Sensory Dendritic Endings through UNC-52/Perlecan in *C. elegans*. *Dev Cell* 33(4):388-400.

22. Kim ME, Shrestha BR, Blazeski R, Mason CA, & Grueber WB (2012) Integrins establish dendrite-substrate relationships that promote dendritic self-avoidance and patterning in drosophila sensory neurons. *Neuron* 73(1):79-91.
23. Han C, *et al.* (2012) Integrins regulate repulsion-mediated dendritic patterning of drosophila sensory neurons by restricting dendrites in a 2D space. *Neuron* 73(1):64-78.
24. Parrish JZ, Emoto K, Jan LY, & Jan YN (2007) Polycomb genes interact with the tumor suppressor genes hippo and warts in the maintenance of Drosophila sensory neuron dendrites. *Genes Dev* 21(8):956-972.
25. Parrish JZ, Xu P, Kim CC, Jan LY, & Jan YN (2009) The microRNA bantam functions in epithelial cells to regulate scaling growth of dendrite arbors in drosophila sensory neurons. *Neuron* 63(6):788-802.
26. Sugimura K, *et al.* (2003) Distinct developmental modes and lesion-induced reactions of dendrites of two classes of Drosophila sensory neurons. *J Neurosci* 23(9):3752-3760.
27. Lee T & Luo L (1999) Mosaic analysis with a repressible cell marker for studies of gene function in neuronal morphogenesis. *Neuron* 22(3):451-461.
28. Oda H, Uemura T, Harada Y, Iwai Y, & Takeichi M (1994) A Drosophila homolog of cadherin associated with armadillo and essential for embryonic cell-cell adhesion. *Dev Biol* 165(2):716-726.
29. Genova JL & Fehon RG (2003) Neuroglian, Gliotactin, and the Na⁺/K⁺ ATPase are essential for septate junction function in Drosophila. *J Cell Biol* 161(5):979-989.
30. Delon I & Brown NH (2009) The integrin adhesion complex changes its composition and function during morphogenesis of an epithelium. *J Cell Sci* 122(Pt 23):4363-4374.
31. Kamimura K, *et al.* (2006) Specific and flexible roles of heparan sulfate modifications in Drosophila FGF signaling. *J Cell Biol* 174(6):773-778.
32. Dhoot GK, *et al.* (2001) Regulation of Wnt signaling and embryo patterning by an extracellular sulfatase. *Science* 293(5535):1663-1666.
33. Kleinschmit A, *et al.* (2010) Drosophila heparan sulfate 6-O endosulfatase regulates Wingless morphogen gradient formation. *Dev Biol* 345(2):204-214.
34. McGuire SE, Le PT, Osborn AJ, Matsumoto K, & Davis RL (2003) Spatiotemporal rescue of memory dysfunction in Drosophila. *Science* 302(5651):1765-1768.
35. Grueber WB, Jan LY, & Jan YN (2002) Tiling of the Drosophila epidermis by multidendritic sensory neurons. *Development* 129(12):2867-2878.
36. Farah CA & Leclerc N (2008) HMWMAP2: new perspectives on a pathway to dendritic identity. *Cell Motil Cytoskeleton* 65(7):515-527.
37. Hummel T, Krukkert K, Roos J, Davis G, & Klambt C (2000) Drosophila Futsch/22C10 is a MAP1B-like protein required for dendritic and axonal development. *Neuron* 26(2):357-370.
38. Karpova N, Bobinnec Y, Fouix S, Huitorel P, & Debec A (2006) Jupiter, a new Drosophila protein associated with microtubules. *Cell Motil Cytoskeleton* 63(5):301-312.
39. Arthur AL, Yang SZ, Abellaneda AM, & Wildonger J (2015) Dendrite arborization requires the dynein cofactor NudE. *J Cell Sci* 128(11):2191-2201.
40. Belenkaya TY, *et al.* (2004) Drosophila Dpp morphogen movement is independent of dynamin-mediated endocytosis but regulated by the glypican members of heparan sulfate proteoglycans. *Cell* 119(2):231-244.

41. Han C, Belenkaya TY, Wang B, & Lin X (2004) Drosophila glypicans control the cell-to-cell movement of Hedgehog by a dynamin-independent process. *Development* 131(3):601-611.
42. Han C, Yan D, Belenkaya TY, & Lin X (2005) Drosophila glypicans Dally and Dally-like shape the extracellular Wingless morphogen gradient in the wing disc. *Development* 132(4):667-679.
43. Struhl G & Basler K (1993) Organizing activity of wingless protein in Drosophila. *Cell* 72(4):527-540.
44. Fox AN & Zinn K (2005) The heparan sulfate proteoglycan syndecan is an in vivo ligand for the Drosophila LAR receptor tyrosine phosphatase. *Curr Biol* 15(19):1701-1711.
45. Johnson KG, *et al.* (2006) The HSPGs Syndecan and Dallylike bind the receptor phosphatase LAR and exert distinct effects on synaptic development. *Neuron* 49(4):517-531.
46. Andersen JN, *et al.* (2005) Computational analysis of protein tyrosine phosphatases: practical guide to bioinformatics and data resources. *Methods* 35(1):90-114.
47. Diao F, *et al.* (2015) Plug-and-play genetic access to drosophila cell types using exchangeable exon cassettes. *Cell Rep* 10(8):1410-1421.
48. Port F, Chen HM, Lee T, & Bullock SL (2014) Optimized CRISPR/Cas tools for efficient germline and somatic genome engineering in Drosophila. *Proc Natl Acad Sci U S A* 111(29):E2967-2976.
49. Desai CJ, Gindhart JG, Jr., Goldstein LS, & Zinn K (1996) Receptor tyrosine phosphatases are required for motor axon guidance in the Drosophila embryo. *Cell* 84(4):599-609.
50. Garrity PA, *et al.* (1999) Retinal axon target selection in Drosophila is regulated by a receptor protein tyrosine phosphatase. *Neuron* 22(4):707-717.
51. Matthews BJ, *et al.* (2007) Dendrite self-avoidance is controlled by Dscam. *Cell* 129(3):593-604.
52. Zipursky SL & Grueber WB (2013) The molecular basis of self-avoidance. *Annu Rev Neurosci* 36:547-568.
53. Soba P, *et al.* (2015) The Ret receptor regulates sensory neuron dendrite growth and integrin mediated adhesion. *Elife* 4.
54. Meltzer S, *et al.* (2016) Epidermis-Derived Semaphorin Promotes Dendrite Self-Avoidance by Regulating Dendrite-Substrate Adhesion in Drosophila Sensory Neurons. *Neuron* 89(4):741-755.
55. Markram H, *et al.* (2004) Interneurons of the neocortical inhibitory system. *Nat Rev Neurosci* 5(10):793-807.
56. Han C, *et al.* (2014) Epidermal cells are the primary phagocytes in the fragmentation and clearance of degenerating dendrites in Drosophila. *Neuron* 81(3):544-560.
57. Han C, *et al.* (2004) Distinct and collaborative roles of Drosophila EXT family proteins in morphogen signalling and gradient formation. *Development* 131(7):1563-1575.
58. Yan D, Wu Y, Feng Y, Lin SC, & Lin X (2009) The core protein of glypican Dally-like determines its biphasic activity in wingless morphogen signaling. *Dev Cell* 17(4):470-481.
59. Han C, Jan LY, & Jan YN (2011) Enhancer-driven membrane markers for analysis of nonautonomous mechanisms reveal neuron-glia interactions in Drosophila. *Proc Natl Acad Sci U S A* 108(23):9673-9678.

60. McDonald JA, Khodyakova A, Aranjuez G, Dudley C, & Montell DJ (2008) PAR-1 kinase regulates epithelial detachment and directional protrusion of migrating border cells. *Curr Biol* 18(21):1659-1667.
61. Doyle HJ, Kraut R, & Levine M (1989) Spatial regulation of *zerknüllt*: a dorsal-ventral patterning gene in *Drosophila*. *Genes Dev* 3(10):1518-1533.
62. Hoch M, Schroder C, Seifert E, & Jackle H (1990) cis-acting control elements for Kruppel expression in the *Drosophila* embryo. *EMBO J* 9(8):2587-2595.
63. Szymczak AL, *et al.* (2004) Correction of multi-gene deficiency in vivo using a single 'self-cleaving' 2A peptide-based retroviral vector. *Nat Biotechnol* 22(5):589-594.

CHAPTER 3

Robust CRISPR/Cas9-mediated tissue specific mutagenesis reveals gene redundancy and perdurance in *Drosophila*²

INTRODUCTION

Tissue-specific loss-of-function (LOF) analysis is instrumental for elucidating the developmental roles of essential genes, determining cell autonomy, and dissecting cell-cell interactions.

Conventional methods for studying tissue-specific gene function in *Drosophila*, such as mosaic analysis with a repressible cell marker (MARCM) (1) and tissue-specific RNA interference (RNAi) (2, 3), are powerful approaches for genetic screens and LOF analysis. However, these techniques present several disadvantages. RNAi is prone to off-target effects (5) and gene knockdown is rarely complete (2) because this technique only targets mRNAs for degradation or translational suppression. MARCM produces more reliable LOF of genes of interest, but the process can be labor intensive and requires multiple components to be combined in the same animal.

The CRISPR/Cas9 system (6) has the potential to surpass the current methods of tissue-specific LOF in *Drosophila* due to its simplicity and efficiency in creating gene disruption (7-12). In this system, Cas9 endonuclease cleaves genomic DNA at a site determined by the protospacer sequence (or target sequence) of a chimeric guide RNA (gRNA) (6). Cas9-mediated double-stranded breaks (DSBs) are then repaired through either nonhomologous end joining (NHEJ) or homology-directed repair (HDR) (13). Imprecise repair through NHEJ can result in

² This chapter was submitted to Genetics as Poe, A.R., Wang, B., Sapar, M.L., Ji, H., et. al. Highly efficient CRISPR/Cas9-mediated tissue specific mutagenesis in *Drosophila*. Molecular cloning of gRNAs and tissue-specific Cas9s was performed by Bei Wang. Initial screening, evaluation, and establishment of Cas9 insertions and gRNAs was performed by Amy Poe, Maria Sapar, Hui Ji, Kailyn Li, Tirenolu Onabajo, Rushaniya Fazliyeva, Mary Gibbs, and Yue Qiu. All live imaging was performed by Amy Poe.

small insertions or deletions (indels) at each target site (7) or deletions of DNA fragments between two target sites (10, 11). CRISPR/Cas9 has been successfully used in *Drosophila* and other organisms to create heritable mutations (7-9), to edit genomic sequences precisely (14, 15), and to control gene expression (16, 17).

Tissue-specific mutagenesis of genes has been achieved in *Drosophila* by combining the CRISPR/Cas9 system with the Gal4/UAS system (18-20). In this approach, tissue-specific Gal4 drives *UAS-Cas9* expression, while gRNAs are expressed either from ubiquitous promoters (18, 19) or by UAS (20). Transgenic constructs expressing multiple gRNAs increase mutagenesis efficiency and allow simultaneous mutagenesis of more than one gene (18-20). Despite these initial successes, Gal4-driven Cas9 and transgenic gRNAs have not been widely used to study tissue-specific gene function due to uncertainties and limitations associated with this method. For example, gRNAs can vary greatly in their mutagenic efficiency, and it is difficult to know whether a transgenic gRNA reliably causes mutations in the tissue of interest. These concerns worsen when a multiplex gRNA construct is used to knock out two or more genes simultaneously. Gal4-driven Cas9 has several additional potential drawbacks that could limit its applications in developmental studies. First, the intermediate Gal4 expression step can delay Cas9 expression, making it difficult to study early gene functions in specific tissues. Second, the Gal4/UAS system often results in excessive levels of Cas9 expression which can be toxic (21). Finally, using Gal4-driven Cas9 makes the Gal4/UAS system unavailable for other genetic manipulations in the same animal. Thus, a simpler and more robust method of tissue-specific mutagenesis via CRISPR/Cas9 is desirable.

One way to improve tissue-specific mutagenesis efficiency is through optimization of transgenic gRNAs. Previous studies in *Drosophila* exploring choices of the gRNA promoter, the

length and sequence composition of the target sequence, and methods of producing multiple gRNAs from a single construct have identified several parameters for making efficient gRNAs (18-20, 22). However, the goal of most of these studies was to increase the frequency of heritable mutations, leaving room for optimization of transgenic gRNA design for mutagenesis in somatic cells. In particular, specific modifications of the gRNA scaffold improve Cas9 targeting to DNA in human cells (23), but these modifications have not been tested to date in *Drosophila*. Thus, there is a compelling need for optimized transgenic gRNAs coupled with tissue-specific control of Cas9 efficacy.

Here, we have developed a new CRISPR/Cas9 toolkit that achieves highly efficient knockout of one or multiple *Drosophila* genes in a tissue-specific manner. Our method of CRISPR-mediated tissue-restricted mutagenesis (CRISPR-TRiM) combines a transgenic Cas9 driven by a tissue specific enhancer with a transgenic construct that ubiquitously expresses multiple gRNAs. By targeting every gene of interest with two gRNAs, this system mutates all target genes tissue-specifically through indels or large DNA deletions. To build the most efficient reagents, we have generated convenient tools for making and evaluating enhancer-driven Cas9 transgenes, identified a multi-gRNA design that is superior to previous options, and established an *in vivo* assay for testing gRNA efficiency in causing DSBs. We investigated how the frequency of DNA deletion in individual somatic cells is impacted by the distance between two target sites and we further found that enhancer-driven Cas9 is more effective in causing LOF and less cytotoxic than Gal4-driven Cas9 in *Drosophila* sensory neurons. Using genes in the SNARE (soluble *N*-ethylmaleimide-sensitive factor attachment protein receptor) pathway as examples, we demonstrate that CRISPR-TRiM can efficiently knock out multiple genes simultaneously in the same neurons and reveal their redundant functions in neuronal

morphogenesis. Our results also underscore the importance of mutagenesis timing for uncovering tissue-specific gene functions: Post-mitotic knockout of neuronal type-specific genes, such as the receptor protein tyrosine phosphatase *Ptp69D*, is sufficient and effective for removing gene functions; while housekeeping genes, such as those encoding NSF and SNAP proteins, require mutagenesis earlier in the cell lineage to unmask their LOF phenotypes.

RESULTS

Generation and evaluation of tissue-specific Cas9 lines

Our CRISPR-TRiM strategy relies on the availability of efficient tissue-specific Cas9 transgenes. To simplify the generation of tissue-specific Cas9 lines, we developed a Cas9 Gateway destination vector pDEST-APIC-Cas9 using the pAPIC (attB P-element insulated CaSpeR) backbone optimized for enhancer-driven transgene expression (24) (Figure 3.1A). Tissue-specific enhancers can be conveniently swapped into this vector through the Gateway LR reaction to generate Cas9-expression constructs. This cloning strategy is compatible with over 14,000 FlyLight (25) and VT (26) enhancers whose expression profiles for multiple developmental stages and tissues in *Drosophila* are publicly available.

An ideal tissue-specific Cas9 should be consistently and robustly expressed in the tissue of interest but not in unintended tissues. In practice, the insertion site in the genome often modifies the expression pattern, timing, and level of a transgene (27). This position effect could impact the tissue specificity and mutagenesis efficiency. To evaluate Cas9 transgenes, we developed a series of tester lines, with the positive tester positively labeling Cas9-expressing cells and negative testers negatively labeling Cas9-expressing cells (Table 3.S1). The positive tester ubiquitously expresses Gal80, Gal4, and two gRNAs targeting Gal80; and it also contains a UAS-driven GFP (Figure 3.1B). In cells that do not express Cas9, Gal80 suppresses Gal4

activity, thereby inhibiting GFP expression. In contrast, in Cas9-expressing cells, the gRNAs induce mutations in Gal80 and thus allow Gal4-driven GFP expression. As examples, we generated random insertions of *ppk-Cas9* and *hh-Cas9* and evaluated their tissue specificities using the positive tester. The *ppk* enhancer is specific to class IV dendritic arborization (C4da) sensory neurons growing on the larval body wall (28), while the R28E04 enhancer of *hh* drives epidermal expression in the posterior half of every hemisegment (<http://flweb.janelia.org>). The positive tester allowed us to identify the *ppk-Cas9* and *hh-Cas9* insertions that most resemble the expected patterns (Figures 3.1C and 3.1D).

Negative testers help further evaluate the efficiency of Cas9 transgenes in inducing mutations. A negative tester contains a ubiquitous or tissue-specific Gal4, a UAS-driven cytosolic or membrane GFP, a UAS-driven nuclear RFP, and two ubiquitous gRNAs targeting GFP (Figure 3.1B). With a negative tester, cells that do not express Cas9 are dually labeled by both GFP and the nuclear RFP. In contrast, Cas9-expressing cells are only labeled by the nuclear RFP, due to GFP mutagenesis. When crossed to negative testers ubiquitously expressing Gal4, *hh-Cas9* as expected caused loss of GFP in the posterior compartments of larval epidermal segments (Figure 3.1E) and imaginal discs (Figure 3.1F). A neuronal negative tester expressing the membrane marker CD8-GFP in all da neurons (NT3) showed that *ppk-Cas9* specifically knocked out GFP in C4da neurons (Figure 3.1G). Negative testers are particularly useful for comparing the efficiency of Cas9 lines in mutagenesis: Lower persistent GFP signals likely reflect earlier-acting Cas9. Using NT3, we detected small but consistent differences among three efficient *ppk-Cas9* insertions (Figure 3.1I), with two insertions (*ppk-Cas9^{1B}* and *ppk-Cas9^{7D}*) outperforming the third one (*ppk-Cas9^{8B}*). In comparison, Cas9 driven by a pan-da *RluA1*

enhancer is less efficient in mutating GFP (Figure 3.1H), leading to higher and variable levels of remaining GFP in C4da neurons (Figure 3.1I).

The Cas9 Gateway cloning vector and the Cas9 tester lines together provide a convenient toolbox for generating and identifying Cas9 transgenes that are most efficient for CRISPR-TRiM.

Figure 3.1. Generation and evaluation of tissue-specific Cas9 lines. See also Table 3.S1.

(A) Diagram of Gateway cloning and transgenesis of Cas9 expression vectors. In, Gypsy insulator; cp, core promoter; 3'P and 5'P, P-element sequences. (B) Diagrams of positive tester (PT) and negative tester (NT), illustrating how Cas9-expressing cells are visualized by each type of tester. In PT, two ubiquitous gRNAs target Gal80. In NT, two ubiquitous gRNAs target GFP. Full genotypes of Cas9 testers are in Table S1. (C and D) Patterns of Cas9 activity in *ppk-Cas9^{7D}* (C) and *hh-Cas9* (D) as visualized by PT. (E and F) Patterns of *hh-Cas9* activity in the larval epidermis as visualized by NT1 (E) and in wing, haltere, and leg imaginal discs as visualized by NT2 (F). The positions of body wall segmental borders (muscle attachment sites) are indicated by yellow broken lines in (D) and (E). *ppk-Cas9* is predicted to be active in C4da neurons, including ddaC. *hh-Cas9* is predicted to be active in the posterior compartments of epidermal segments and imaginal discs. (G and H) Patterns of Cas9 activity in *ppk-Cas9^{7D}* (G) and *RluA1-Cas9* (H) as visualized by NT3. The cell bodies of ddaC neurons are indicated. (I) Quantification of ddaC GFP brightness in NT3 crosses using control (no Cas9) and various da neuron-specific Cas9 lines. *** $p \leq 0.001$; one-way ANOVA and Dunnett's test. n= 16 neurons for each genotype. Black bar, mean; red bars, SD. (Scale bars, 50 μm). Molecular cloning of Cas9 lines was performed by Bei Wang and Yuzhao Hu. Initial screening, evaluation, and establishment of Cas9 insertions was performed by Amy Poe, Maria Sapar, Hui Ji, Kailyn Li, Tirenolu Onabajo, Rushaniya Fazliyeva, Mary Gibbs, and Yue Qiu. Live imaging was performed by Amy Poe.

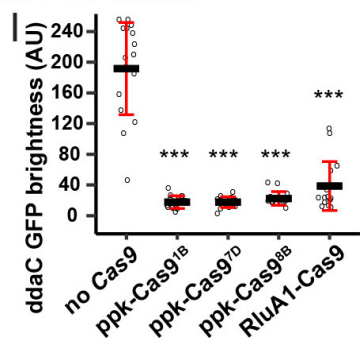
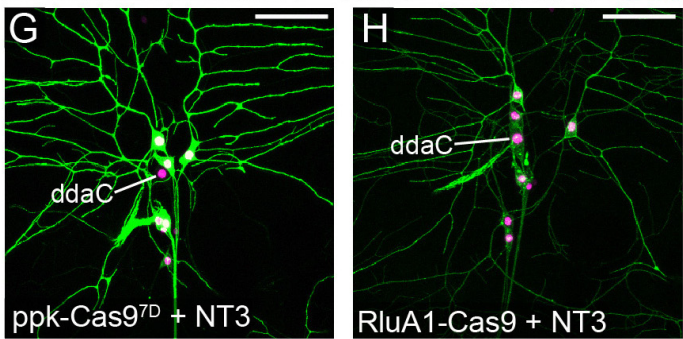
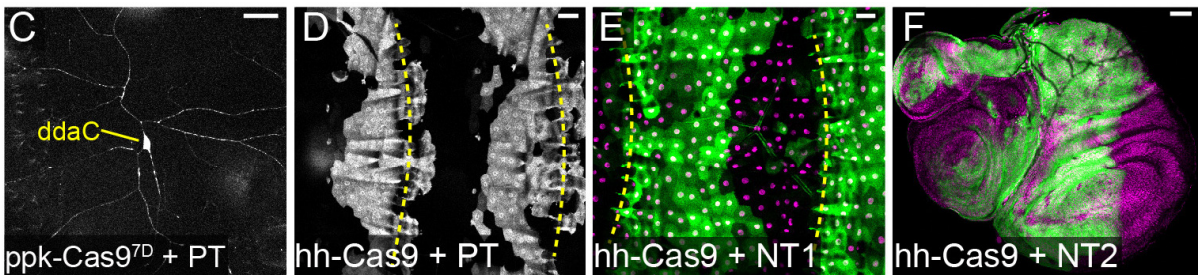
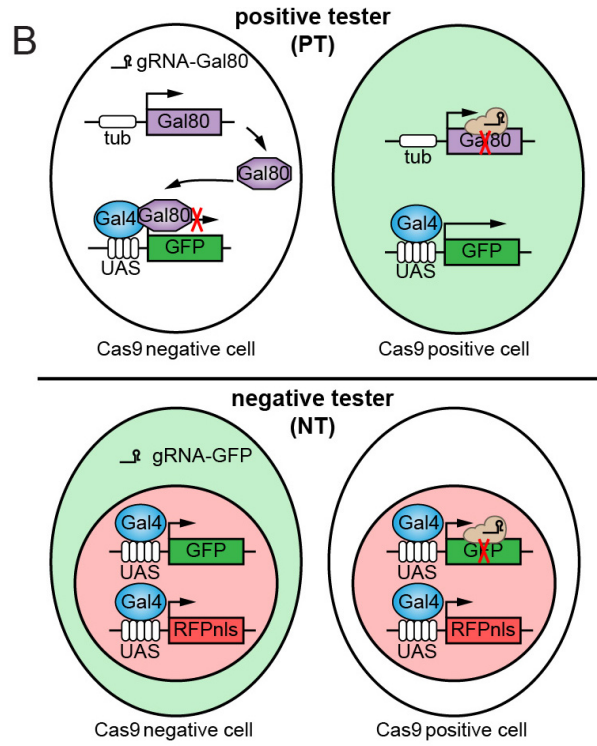
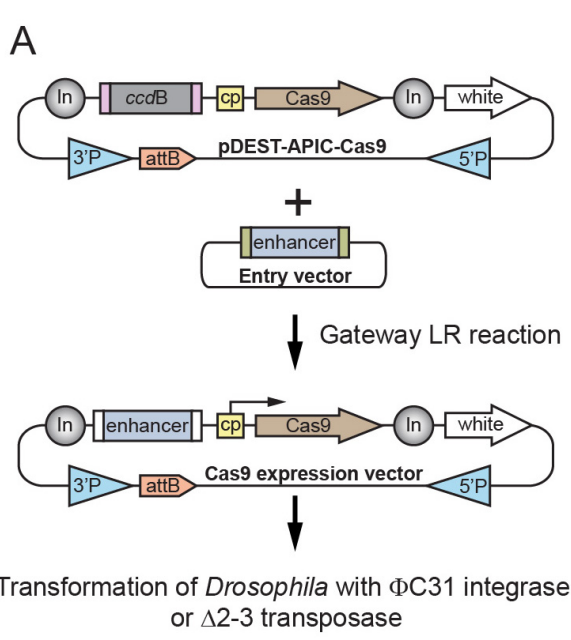


Table 3.S1. List of positive and negative tester lines, related to Figure 3.1.

Tester	Genotype	Comment
Positive Tester (PT)	<i>Act-Gal4 UAS-GFP; tub-Gal80 gRNA-Gal80</i>	ubiquitous tester*
Negative Tester 1 (NT1)	<i>gRNA-GFP UAS-mCherryNLS; Act-Gal4 UAS-GFP</i>	ubiquitous tester**
Negative Tester 2 (NT2)	<i>gRNA-GFP UAS-mCherryNLS; tubP-Gal4 UAS-CD8-GFP</i>	ubiquitous tester
Negative Tester 3 (NT3)	<i>21-7 UAS-CD4-tdGFP; gRNA-GFP UAS-RedStinger</i>	PNS tester
Negative Tester 4 (NT4)	<i>gRNA-GFP UAS-mCherryNLS; nsyb-Gal4 UAS-CD4-tdGFP</i>	pan-neuronal tester

* PT shows Cas9-independent expression in the gut.

** The Gal4 is not active in imaginal discs.

Optimization of multi-gRNA design for tissue-specific gene knockout in *Drosophila*

Being able to express multiple gRNAs from a single transgenic construct is desirable for CRISPR-TRiM, as more gRNAs can increase the chance of LOF in a single gene and also enable simultaneous mutagenesis of multiple genes (18-20). A common strategy for making multiplex gRNA constructs in *Drosophila* is to use two or three ubiquitous U6 promoters in tandem, each driving a gRNA separately (19). For this purpose, U6:1 and U6:3 promoters have been found to drive high gRNA expression (19). Alternatively, polycistronic gRNA designs with intervening tRNA sequences have also been reported to be effective in expressing multiple gRNAs in plants and *Drosophila* (20, 29). We wished to optimize the multi-gRNA strategy to achieve the greatest mutagenic efficiency in somatic cells. We thus compared four dual-gRNA designs that carry the same two targeting sequences for EGFP and GFP (Figure 3.2A). These constructs were made with a P-element/attB dual transformation vector that uses *mini-white* as the selection marker. Three of them (forward, reverse, and insulated) are variants of a U6:1-gRNA-U6:3-gRNA strategy described previously (19), with differences in the orientation of the gRNA cassette and the use of an insulator to separate *mini-white* and the gRNAs. The fourth design (tgFE) builds upon the tRNA-gRNA strategy (20) and introduces an A-U base pair flip and an extension of the Cas9-binding hairpin (F+E modifications) in the gRNA scaffold (23), which have been shown to greatly improve the targeting of Cas9 to the genomic DNA.

To compare these constructs, we used the larval PNS to evaluate the efficiency of GFP knockout in individual neurons. The dorsal cluster of sensory neurons in every abdominal segment contains 6 da neurons belonging to 4 classes (30) (Figure 3.2B), allowing for accurate measurement of fluorescence intensity at single cell resolutions. To detect sensitively differences in gRNA efficiency, we used the relatively ineffective *RluA1-Cas9* (Figures 3.1H, I) to knock

out *UAS-CD8-GFP* driven by pan-neural *nsyb-Gal4* (31). We found that the performance of gRNAs based on U6:1-gRNA-U6:3-gRNA varied depending on the neuronal identity and that none of these designs were efficient enough to remove GFP in all neurons (Figure 3.2C). In contrast, the tgFE design led to near complete elimination of GFP signals in almost all neurons examined (Figure 3.2C). Therefore, tgFE is a more efficient multiplex gRNA design for tissue-specific mutagenesis. An additional benefit of the tgFE strategy is the convenient cloning of 2-6 gRNAs in a single step.

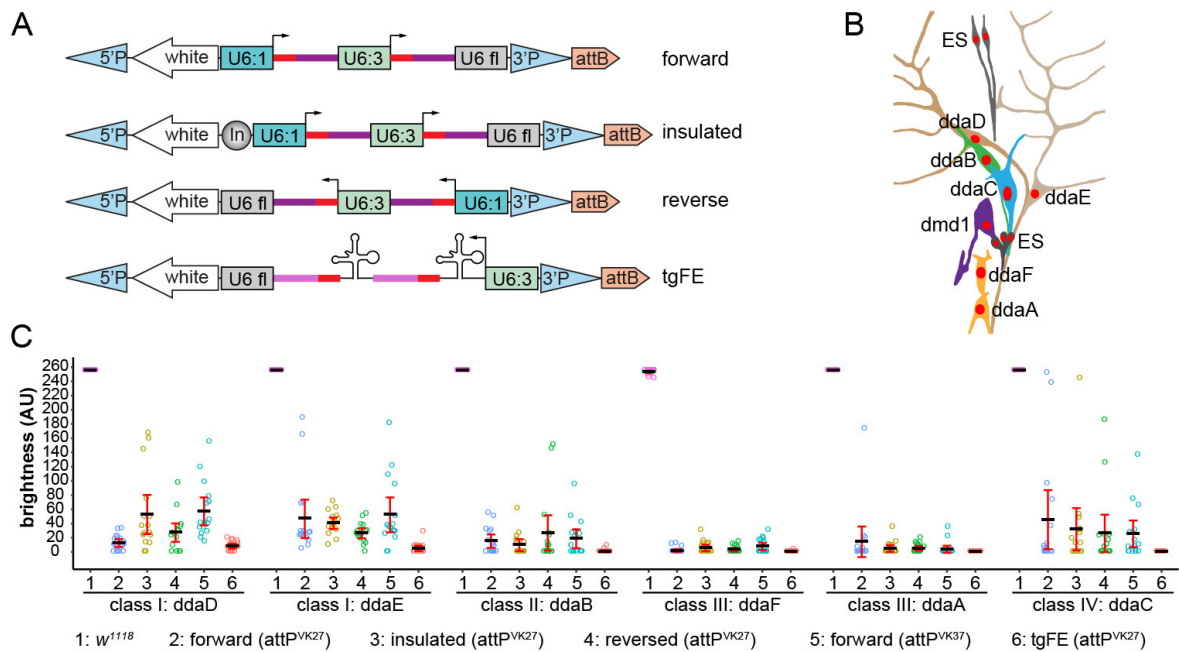


Figure 3.2. Optimization of multi-gRNA design for tissue-specific gene knockout in *Drosophila*.

(A) Four designs of multi-gRNA transgenic vectors. U6:1 and U6:3, U6 promoters; U6 fl, U6 3' flanking sequence; In, Gypsy insulator. Red bars, gRNA targeting sequence; dark magenta bars, original gRNA scaffold; light magenta bars, E+F gRNA scaffold. (B) Diagram of the dorsal cluster of larval peripheral sensory neurons. (C) Comparison of a control (1) and various gRNA-GFP lines in eliminating GFP signal in each dorsal da neuron using *RluA1-Cas9*. Da neurons express *UAS-CD8-GFP* driven by *nsyb-Gal4*. The integration site for each gRNA line is indicated in the parenthesis. The GFP signals in most control neurons are saturated under the setting used. Each circle represents an individual neuron (n=16 for each column). Black bar, mean; red bars, SD. Molecular cloning of multi-gRNA transgenic vectors was performed by Bei Wang. Live imaging and quantifications were performed by Amy Poe.

Efficiency of dual gRNA-mediated DNA deletion at the single cell level

When using two gRNAs to target the same gene, Cas9-mediated DSBs can result in indels at both target sites, or large DNA deletions between the two target sites (10). Deletion of a larger piece of DNA is more likely to generate a null allele. To investigate the frequency of large deletions caused by two gRNAs in individual cells, we constructed a reporter *nSyb-tdGFP* (“td” standing for tandem dimer) (Figure 3.3A) that labels all 12 neurons in the dorsal cluster of PNS sensory neurons (Figures 3.2B, 3.3B). In addition, we designed 7 gRNAs (0 to 6) targeting different sites in the non-coding sequence of this reporter, with site 0 located before the nSyb enhancer, site 1 immediately after the enhancer, and the remaining sites at various distances downstream of the tdGFP coding sequence (Figure 3.3A). We reasoned that small indels at any of these target sites would be unlikely to abolish GFP expression, but large deletions between site 0 and any of the other targeting sites would (Figure 3.3C). As a control, we included a gRNA pair that targets two sites in the tdGFP coding sequence (gRNA-GFP) and therefore is predicted to remove GFP expression by either indels or large deletions.

Using a ubiquitously expressed *Act-Cas9* (19), we tested the efficiencies of these gRNA pairs in eliminating GFP expression in individual neurons with two different *nSyb-tdGFP* insertions. In all animals examined, *gRNA-GFP* completely abolished GFP expression as expected (Figures 3.3D, E), demonstrating the efficiency of DSB-mediated mutagenesis. Unexpectedly, gRNA 0 alone reduced numbers of labeled neurons in some animals (reduction mean \pm SD: 19.8% \pm 15.7% for attP^{VK37} and 14.6% \pm 13.1% for attP^{VK33}) (Figures 3.3D, E), likely due to deletions extending into regulatory elements in the nSyb enhancer. Pairing gRNA 0 with gRNAs 1-6 further reduced the number of labeled neurons (the range of reduction mean \pm SD for all pairs: 21.4% \pm 13.3% to 59.4% \pm 13.2% for attP^{VK37} and 24.0% \pm 16.1% to 43.8% \pm 17.1% for

attP^{VK33}), with a tendency for gRNA pairs positioned closer more often generating fewer GFP positive neurons (Figures 3.3C-E). These data suggest that large deletions occur in random somatic cells and that an inverse correlation appears to exist between deletion frequency and gRNA distance. Importantly, our results suggest that large deletions do not occur frequently enough to remove gene function in every cell such that indels in the coding region are more reliable for causing LOF.

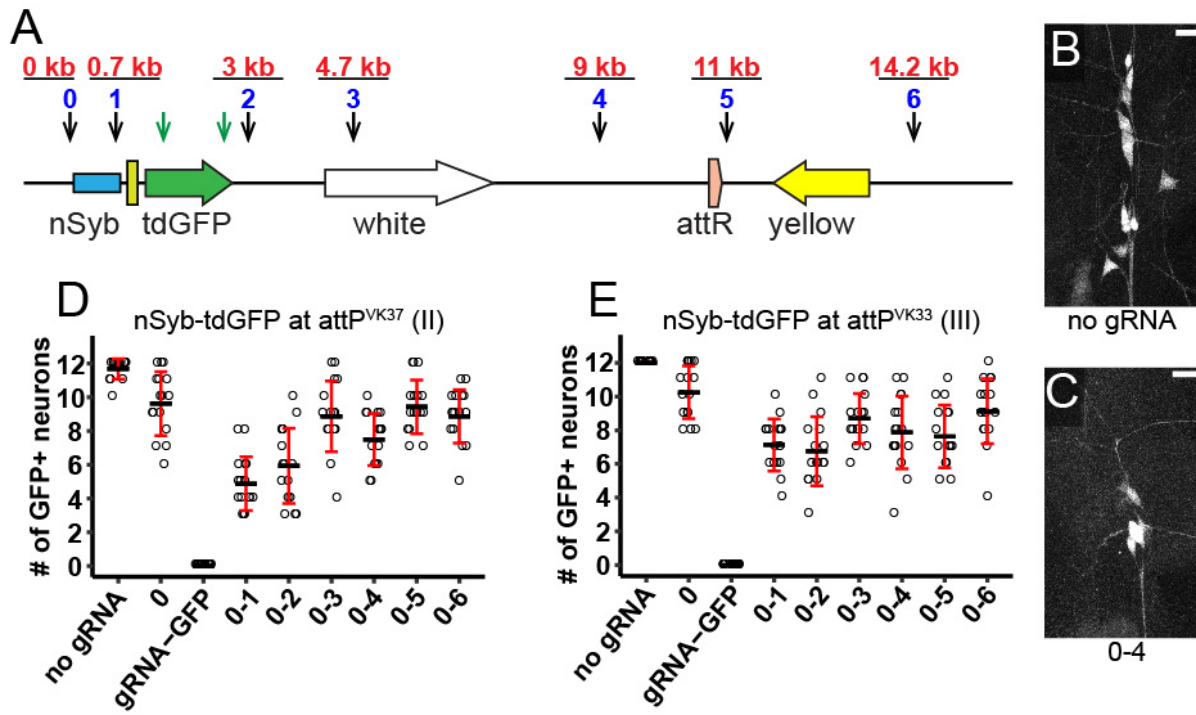


Figure 3.3. Efficiency of dual gRNA-mediated DNA deletion at the single cell level.

(A) Diagram showing the *nSyb-tdGFP* reporter integrated in the genome and gRNA target sites. Each blue number and the black arrow below it indicate a gRNA targeting non-coding sequence of the reporter. The distance of each gRNA from gRNA 0 is indicated in red above the gRNA. The two green arrows indicate two gRNAs targeting the coding sequence of *tdGFP*. (B and C) Dorsal clusters of PNS neurons labeled by the reporter in a control animal (B) and an animal expressing gRNAs 0 and 4 (C). (D and E) Quantification of the number of GFP-positive neurons for each gRNA pair using *nSyb-tdGFP* inserted at *attP^{VK37}* (D) and *attP^{VK33}* (E) sites. Each circle represents an individual neuron (n=16 neurons for each genotype). Black bar, mean; red bars, SD. (Scale bars, 25 μ m). Molecular cloning of gRNAs was performed by Bei Wang. Live imaging and quantifications were performed by Amy Poe.

Enhancer-driven Cas9 is advantageous over Gal4-driven Cas9 for studying neural development

Conditional mutagenesis can be achieved in *Drosophila* somatic cells using Gal4-driven Cas9 (18-20), but this method requires an intermediate transcription step that could potentially delay Cas9 expression. Consistent with this assumption, *ppk-CD4-tdGFP* is expressed at least 8 hours earlier than *UAS-CD8-GFP* driven by *ppk-Gal4* in the embryo (24). Thus, we predict that enhancer-driven Cas9 will result in earlier Cas9 action, thereby reducing perdurance of wildtype mRNA or protein products of the target gene made prior to mutation induction. We tested this hypothesis by comparing the effectiveness of enhancer-driven Cas9 and Gal4-driven Cas9 in knocking out CD4-tdGFP expression in C4da neurons (Figure 3.4A). We observed more consistent and stronger reduction of GFP with *ppk-Cas9* insertions compared to *ppk-Gal4 UAS-Cas9* (*ppk>Cas9*) (Figure 3.4B), although these differences were not statistically significant with our sample sizes. To ask whether even earlier Cas9 expression could lead to further GFP reduction, we made an enhancer-driven Cas9 that is expressed in sensory organ precursors (SOPs), the progenitor cells of da neurons (32). Indeed, *SOP-Cas9* resulted in complete loss of GFP fluorescence in most animals (Figure 3.4B).

High levels of Cas9 have been reported to be cytotoxic (21). Consistent with our supposition that Gal4-driven Cas9 generally produces more Cas9 protein than enhancer-fusion versions, we found that *ppk>Cas9* caused obvious dendrite reduction in C4da neurons even in the absence of gRNAs while *ppk-Cas9* lines had much weaker impacts on dendrite morphology (Figures 3.4C-E, G). These data suggest that high levels of Cas9 in post-mitotic neurons are not desirable for studying neuronal morphogenesis and that enhancer-driven Cas9 could alleviate this concern.

We also compared the effects of RNAi-mediated suppression of GFP expression and CRISPR/Cas9-induced GFP mutagenesis. CD4-tdGFP was knocked down with a publicly available *UAS-GFP-RNAi* line (33) driven by *ppk-Gal4*. We also co-expressed Dicer-2 (Dcr-2) in C4da neurons to enhance double strand RNA (dsRNA)-mediated mRNA knockdown (2). RNAi was found to be less efficient in eliminating GFP than CRISPR-mediated mutagenesis by either enhancer-driven Cas9 or Gal4-driven Cas9 (Figure 3.4B). In addition, we found that Dcr-2 overexpression, which is commonly employed in *Drosophila* RNAi experiments, caused a strong dendrite reduction (Figures 3.2F, G), indicating that Dcr-2 also has cytotoxicity in neurons.

Our results suggest that, at least in larval sensory neurons, enhancer-driven Cas9 outperforms Gal4-driven Cas9 in tissue-specific mutagenesis and that the CRISPR-TRiM method is more effective than RNAi in LOF studies.

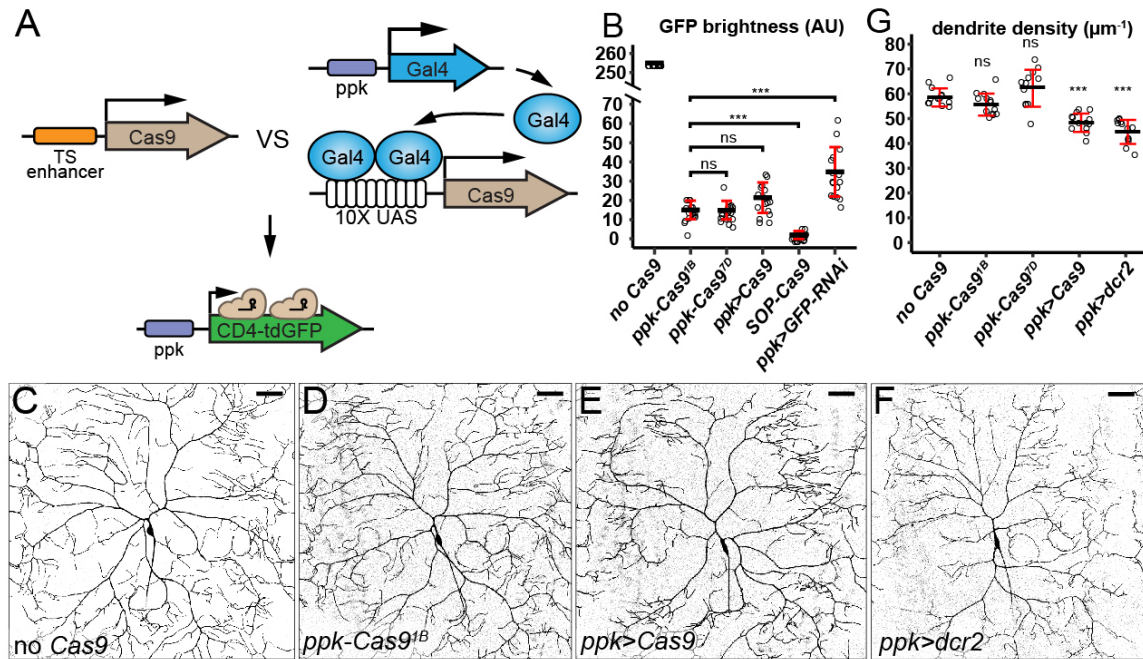


Figure 3.4. Enhancer-driven Cas9 is advantageous over Gal4-driven Cas9 in studying neural development.

(A) Diagram showing the comparison of tissue-specific (TS) enhancer-driven Cas9 and Gal4-driven Cas9 in knocking out *ppk-CD4-tdGFP*. (B) Quantification of GFP brightness in C4da neurons in the control, Cas9-expressing animals, and GFP knockdown animals. GFP signals in the control (no Cas9) are saturated. *** $p \leq 0.001$; ns, not significant; one-way ANOVA and Tukey's HSD test. (C-F) DdaC neurons in the control (C) and animals expressing *ppk-Cas9^{1B}* (D), *ppk-Gal4*-driven Cas9 (E), and *ppk-Gal4*-driven *dcr2* (F). (G) Quantification of dendrite density in genotypes indicated. *** $p \leq 0.001$; ns, not significant; one-way ANOVA and Dunnett's test. Each circle represents an individual neuron. $n=16$ for genotypes in (B) and $n=13$ for genotypes in (G). Black bar, mean; red bars, SD. (Scale bars, 50 μm). Molecular cloning of *gRNA-GFP* was performed by Bei Wang. Live imaging and quantifications were performed by Amy Poe.

Post-mitotic knockout of *Ptp69D* reveals its function in C4da neurons

To validate the effectiveness of CRISPR-TRiM in studying neuronal morphogenesis, we knocked out the receptor protein tyrosine phosphatase *Ptp69D* in C4da neurons. Using hemizygous *Ptp69D* mutants and MARCM, we previously found that loss of *Ptp69D* in C4da neurons caused dendritic reduction with shortened terminal dendrites (4). As hemizygous mutants completely lack zygotic transcription and MARCM removes the *Ptp69D* gene before the birth of neurons, it is unclear from our previous results whether mutagenesis after the birth of neurons (post-mitotic mutagenesis) would be sufficient to remove *Ptp69D* function. We thus made a *gRNA-Ptp69D* line expressing three gRNAs, each targeting a distinct site in the *Ptp69D* coding sequence.

To validate the efficiency of *gRNA-Ptp69D*, we established a “Cas9-LEThAL” (for Cas9-induced lethal effect through the absence of Lig4) assay (Figure 3.S2) that was adapted from a previously described method for assessing injection-based gRNA efficiency (34). Efficient gRNAs for non-essential genes, such as a published gRNA for *e* (19) (Table 3.S2), cause male-specific lethality in pupal stages when males carrying gRNAs are crossed to *Act-Cas9 lig4* homozygous females. But if the target gene is essential, in the same cross, efficient gRNAs should cause lethality of both males and females similar to homozygous mutants. *gRNA-Ptp69D* caused all animals to die at late pupal stages in this assay, indicating that this gRNA line is efficient (Table 3.S2).

We knocked out *Ptp69D* in C4da neurons using both *ppk-Cas9* and *SOP-Cas9*. As the *ppk* enhancer only becomes active in stage-16 embryos after the birth of C4da neurons (28), *ppk-Cas9* would only induce mutations post-mitotically. In contrast, the *SOP* enhancer turns on in sensory organ precursors (35) that divide twice to give rise to da neurons (36), enabling *SOP-*

Cas9 to act before the neuronal birth. We found that both *ppk-Cas9* and *SOP-Cas9* caused consistent and similar degrees of dendritic reduction in C4da neurons in late 3rd instar larvae (Figures 3.5A-D). In both cases, the extent of dendrite reduction caused by CRISPR-TRiM were also similar to that in *Ptp69D¹⁴/Df(3L)8ex34* hemizygous null mutant larvae (4) (Figures 3.5E, F). These data suggest that post-mitotic mutagenesis is sufficient to remove *Ptp69D* gene function, which is consistent with Ptp69D being a neuronal type-specific gene (4, 37). Our results demonstrate that CRISPR-TRiM can efficiently eliminate gene function in a tissue-specific manner.

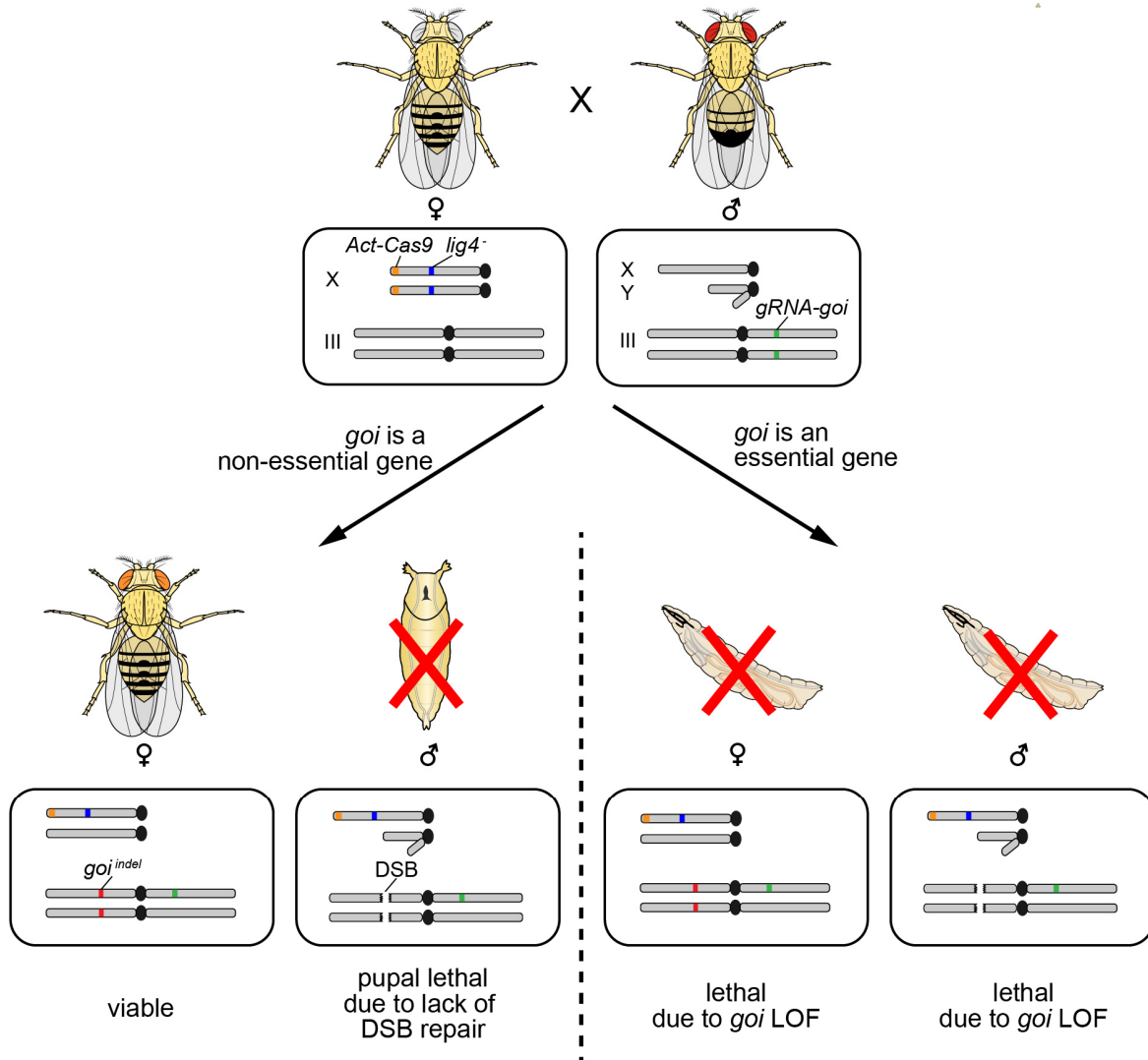


Figure 3.S1. Cas9-LEThAL assay, related to Figure 3.6.

In Cas9-LEThAL (for Cas9-induced lethal effect through the absence of Lig4) assay, homozygous males of gRNA for *goi* (a hypothetical gene name for *gene of interest*, which is on the third chromosome in the illustrated example) are crossed to *Act-Cas9 lig4* homozygous females. As *Act-Cas9* and the *lig4* null mutation are both on the X chromosome, the male progeny from the cross is *lig4* deficient and therefore cannot repair DNA double-strand breaks (DSBs) through NHEJ. In contrast, the female progeny is heterozygous for *lig4* and thus can repair DSBs. Efficient gRNAs will target the *goi* locus to create bi-allelic DSBs, which will be repaired to generate indels in female somatic cells but left unrepaired in male somatic cells. If *goi* is a non-essential gene, female progeny with indel mutations at the *goi* locus should be viable while male progeny will die in the pupal stage due to the lack of DSB repair. If *goi* is an essential gene, *goi* LOF will cause both female and male progeny to die to at a stage similar to the lethal phase of *goi* zygotic null mutants. Viable male progeny from this cross indicates inefficient gRNAs. All flies in this assay carry a *w* mutation, which is omitted from the diagram.

Table 3.S2. Results of the Cas9-LEThAL assay

Gene Name	Cas9-LEThAL assay lethal phase	Reported lethal phase of null mutants
<i>e</i>	Males: prepupae; females: viable	viable
<i>Ptp69D</i>	Pharate adults	Pupae with rare escapers ¹⁷
<i>Nsf1 (comt)</i>	Males: early pupae; female: pharate adults to newly eclosed adults (dead in the food)	Late pupae (pharate adults) ¹⁶
<i>Nsf2</i>	1st instar larvae	1st instar larvae ¹⁶
<i>Nsf1/Nsf2</i>	1st instar larvae	unknown
<i>Snap24</i>	2 nd instar larvae to early 3 rd instar larvae	unknown
<i>Snap25</i>	Males: early pupae; females: pharate adults	Late pupae (pharate adults) ¹⁸
<i>Snap29</i>	1st instar larvae to early 3rd instar larvae	Early larvae ¹⁹
<i>Snap24/Snap25</i>	1st instar larvae	unknown
<i>Snap24/Snap25/Snap29</i>	Late embryos to early 1st instar larvae	unknown

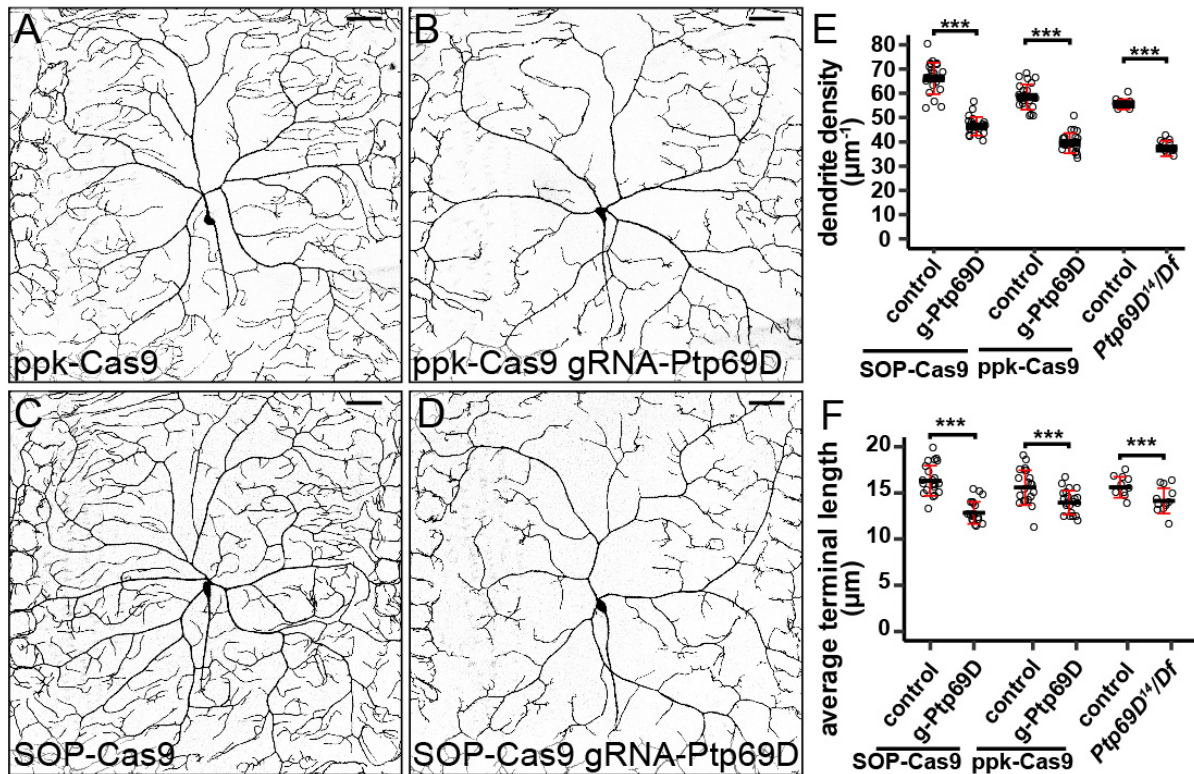


Figure 3.5. Post-mitotic knockout of *Ptp69D* is sufficient to reveal its function in C4da neurons. See also Table 3.S2.

(A-D) DdaC neurons in *ppk-Cas9* control (A), *ppk-Cas9 gRNA-Ptp69D* (B), *SOP-Cas9* control (C), and *SOP-Cas9 gRNA-Ptp69D* (D). (E and F) Quantification of total dendrite density (E) and average terminal dendrite length (F) in the genotypes indicated. Each circle represents an individual neuron: *ppk-Cas9* (n=22); *ppk-Cas9 gRNA-Ptp69D* (n=21); *SOP-Cas9* (n=22); *SOP-Cas9 gRNA-Ptp69D* (n=20). Data for *Ptp69D¹⁴/Df(3L)8ex34* (n=12) and its control (n=10) are from(4) Figure 2.6 for comparison. *** $p \leq 0.001$; Unpaired t-test. Black bar, mean; red bars, SD. (Scale bars, 50 μm). Molecular cloning of *gRNA-Ptp69D* was performed by Bei Wang. Live imaging and quantifications were performed by Amy Poe.

CRISPR-TRiM reveals the redundancy and perdurance of NSF and SNAP genes in dendrite morphogenesis

CRISPR/Cas9 can simultaneously mutate multiple genes in *Drosophila* somatic cells (20). Such an application would be very useful for studying the roles of redundant genes during development. To test whether CRISPR-TRiM can efficiently knock out multiple genes that may exhibit redundant functions, we targeted SNARE complex components in C4da neurons. Because SNAREs are required for all vesicle fusions (38), interference with the complex should severely hamper C4da dendrite growth. *Drosophila* contains two NSF genes (*comt/Nsf1* and *Nsf2*) which are necessary for the recycling of the SNARE complex after membrane fusion (39). *Drosophila* also has three *SNAP-25* paralogues (*Snap24*, *Snap25*, and *Snap29*) that encode the SNAP (or Qbc.IV) group of SNARE proteins thought to be involved in secretion (40). The potential functional redundancy of NSF and SNAP genes has not to date been examined during neuronal morphogenesis.

To conduct CRISPR-TRiM analyses, we used the tgFE design to generate dual-gRNA constructs for every NSF and SNAP gene. Also using the tgFE design, we made 4-gRNA constructs to knock out *Nsf1/Nsf2* simultaneously and *Snap24/Snap25* simultaneously, and a 6-gRNA construct to knock out all three SNAP genes. The efficiencies of these gRNA lines were first validated with the Cas9-LEThAL assay (Table 3.S2). The lethal phase induced by each single-gene gRNA line was consistent with published results for null mutants of the corresponding gene, indicating that the gRNAs are efficient in mutagenesis. We found that *gRNA-Nsf1-Nsf2* was as effective as *gRNA-Nsf2* in causing lethality at 1st instar larvae, while *gRNA-Nsf1* caused lethality in late pupae. This suggests that increasing the number of gRNAs from 2 to 4 in one construct does not reduce the efficiency of gRNAs. Interestingly, compared to

gRNA-Snap24 or *gRNA-Snap25* alone, which produced animals surviving to the late pupal stage, *gRNA-Snap24-Snap25* caused lethality at the 1st instar larvae, demonstrating that Snap24 and Snap25 are redundantly required for the larval development. *gRNA-Snap24-Snap25-Snap29* further advanced the lethal phase to late embryos, suggesting that Snap29 is also redundant with Snap24 and Snap25.

We knocked out NSF and SNAP genes in C4da neurons using both *ppk-Cas9* and *SOP-Cas9*. Removing individual NSF genes did not cause obvious dendritic reductions (Figures S1A-C, H-J), but surprisingly *SOP-Cas9/gRNA-Nsf2* neurons instead showed a mild but consistent increase of dendrite length and density (Figures 3.6G-H). Knocking out both *Nsf1* and *Nsf2* using *ppk-Cas9* produced weak and variable C4da dendrite reduction (Figures 3.6A, B, G-H), while *SOP-Cas9/gRNA-Nsf1-Nsf2* animals showed stronger and more consistent dendrite reductions (Figures 3.6E, G-H). These data suggest that *Nsf1* and *Nsf2* act redundantly to promote dendrite growth. Furthermore, the observation that *SOP-Cas9* caused a stronger phenotype than *ppk-Cas9* suggest that NSF gene products made in sensory organ precursors are not sufficient to support dendrite growth but those made at the time of post-mitotic mutagenesis allow neurons to grow a significant amount of dendrites.

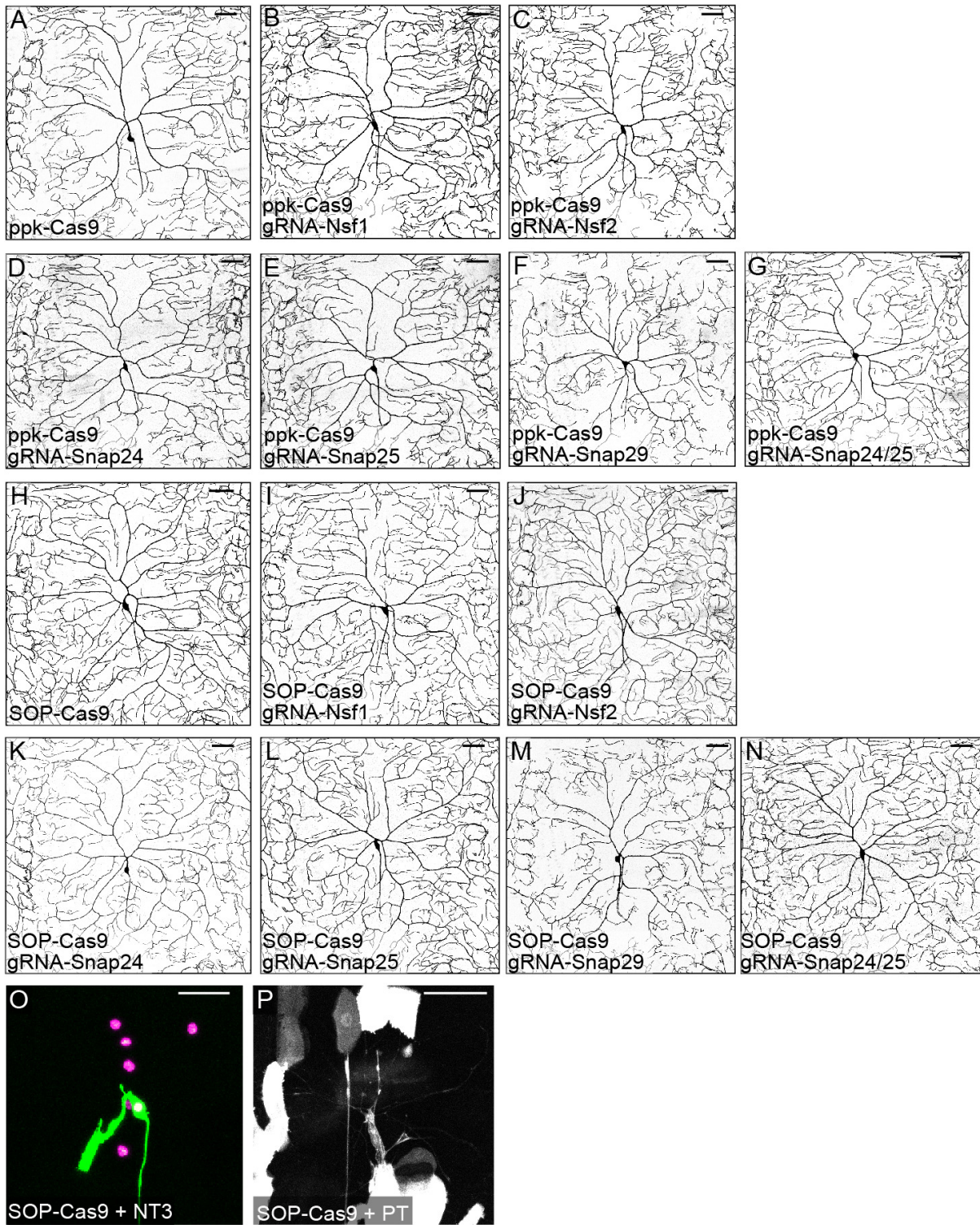
Tissue-specific knockout of individual SNAP genes using *ppk-Cas9* or *SOP-Cas9* produced either no obvious phenotypes (for *Snap24* and *Snap25*) or weak dendrite reductions (for *Snap29*) (Figures 3.S1D-F, K-M). Knocking out both *Snap24* and *Snap25* similarly did not cause obvious dendrite defects (Figures 3.S1G, N). We next knocked out all three SNAP genes using *gRNA-Snap24-Snap25-Snap29*. While *ppk-Cas9*-mediated knockout only slightly reduced dendrite density (Figures 3.6C, G-H), *SOP-Cas9*-mediated knockout caused strong C4da dendrite reduction and degeneration (n=16/19 neurons) in second instar larvae (Figure 3.6F) and

late larval lethality. Although *SOP-Cas9* is highly efficient in da neurons as shown by the NT3 negative tester (Figure 3.S1O), this lethality might be independent of neuronal defects, because *SOP-Cas9* also labeled a small number of random larval epidermal cells with the positive tester (Figure 3.S1P). Nevertheless, our results suggest that, like NSF genes, all three SNAP genes are redundantly required in C4da neurons and that mutagenesis before the neuronal birth is required to unmask the LOF phenotype of SNAP genes.

As the SNARE machinery is required for all vesicle trafficking in the cell, we were curious why knocking out all NSF or all SNAP genes in neurons with *SOP-Cas9* was not sufficient to suppress all dendritic growth. One possibility is that membrane trafficking-independent mechanisms exist that allow neurons to elaborate dendrites. Alternatively, NSF and SNAP gene products contributed maternally or made before *SOP-Cas9* activity persist long enough to support a small degree of larval dendrite growth. To distinguish between these possibilities, we turned to adult C4da neurons. C4da neurons *ddaC* and *v'ada* prune all their dendrites during metamorphosis and regrow new dendritic arbors in late pupae (41). Because dendritic pruning removes all existing gene products except for the residual amounts left in the cell body, dendrite regrowth must rely on new transcription. If NSF and SNAP genes are required for all dendrite growth, knocking out all NSF or SNAP genes during larval stages should prevent dendrite regrowth. Indeed, adult *v'ada* neurons lacking *Nsf1 Nsf2* or *Snap24 Snap25 Snap29* via *ppk-Cas9*-mediated knockout either did not regrow primary branches or showed severe reduction in total dendrite length (Figures 3.6I-L). These data suggest that *ppk-Cas9* can effectively remove redundant genes in post-mitotic neurons and that neuronal dendrite growth absolutely requires SNARE function.

Figure 3.S2. LOF of individual NSF and SNAP genes in C4da neurons, related to Figure 3.7.

(A-G) DdaC neurons in the *ppk-Cas9* control (A), *ppk-Cas9 gRNA-Nsf1* (B), *ppk-Cas9 gRNA-Nsf2* (C), *ppk-Cas9 gRNA-Snap24* (D), *ppk-Cas9 gRNA-Snap25* (E), *ppk-Cas9 gRNA-Snap29* (F), and *ppk-Cas9 gRNA-Snap24-Snap25* (G). (H-N) DdaC neurons in the *SOP-Cas9* control (H), *SOP-Cas9 gRNA-Nsf1* (I), *SOP-Cas9 gRNA-Nsf2* (J), *SOP-Cas9 gRNA-Snap24* (K), *SOP-Cas9 gRNA-Snap25* (L), *SOP-Cas9 gRNA-Snap29* (M), and *SOP-Cas9 gRNA-Snap24-Snap25* (N). (O and P) Cas9 activity patterns of *SOP-Cas9* with the negative tester NT3 (O) and the positive tester (PT) and (P). (Scale bars, 50 μm). Molecular cloning of all gRNAs was performed by Bei Wang. Live imaging was performed by Amy Poe.



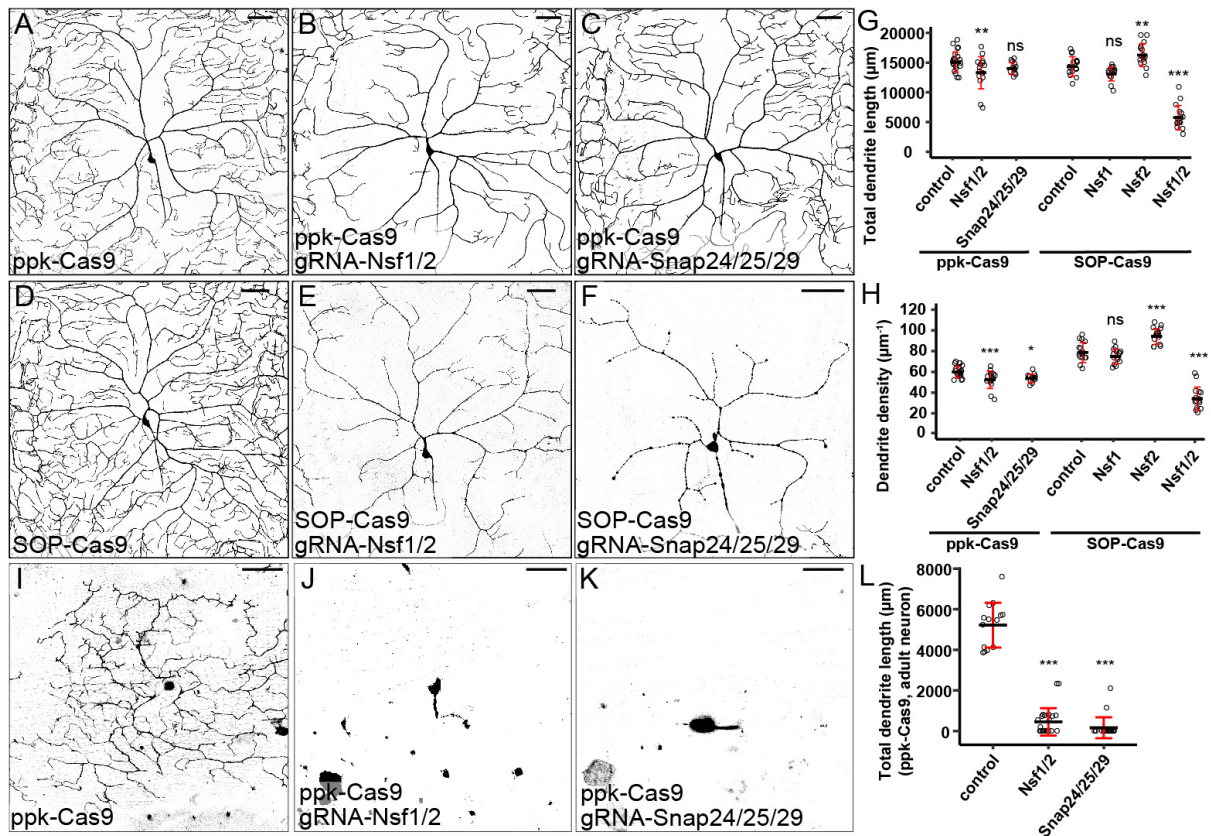


Figure 3.6. CRISPR-TRiM analyses of NSF and SNAP genes in C4da dendrite morphogenesis. See also Figure S2 and Table S2.

(A-C) DdaC neurons in *ppk-Cas9* (A), *ppk-Cas9 gRNA-Nsf1-Nsf2* (B), and *ppk-Cas9 gRNA-Snap24-Snap25-Snap29* (C). (D-F) DdaC neurons in *SOP-Cas9* (D), *SOP-Cas9 gRNA-Nsf1-Nsf2* (E), and *SOP-Cas9 gRNA-Snap24-Snap25-Snap29* (F). (G and H) Quantification of total dendrite length (G) and dendrite density (H) in the genotypes indicated. Each circle represents an individual neuron: *ppk-Cas9* (n=22); *ppk-Cas9 gRNA-Nsf1-Nsf2* (n=16); *ppk-Cas9 gRNA-Snap24-Snap25-Snap29* (n=11); *SOP-Cas9* (n=15), *SOP-Cas9 gRNA-Nsf1* (n=15); *SOP-Cas9 gRNA-Nsf2* (n=15); *SOP-Cas9 gRNA-Nsf1-Nsf2* (n=15). * $p \leq 0.05$; ** $p \leq 0.01$; *** $p \leq 0.001$; ns, not significant; one-way ANOVA and Dunnett's test. (I-K) V'ada neurons in day 0 adults of *ppk-Cas9* (I), *ppk-Cas9 gRNA-Nsf1-Nsf2* (J), *ppk-Cas9 gRNA-Snap24-Snap25-Snap29* (K). (L) Quantification of total dendrite length of adult v'ada neurons expressing *ppk-Cas9* and the gRNAs indicated. Each circle represents an individual neuron: *ppk-Cas9* (n=14), *ppk-Cas9 gRNA-Nsf1-Nsf2* (n=23), *ppk-Cas9 gRNA-Snap24-Snap25-Snap29* (n=20). *** $p \leq 0.001$; one-way ANOVA and Dunnett's test. Black bar, mean; red bars, SD. (Scale bars, 50 µm). Molecular cloning of all gRNAs was performed by Bei Wang. Live imaging and quantifications were performed by Amy Poe.

DISCUSSION

In this study, we describe an optimized strategy that we call CRISPR-TRiM for tissue-specific gene mutagenesis using CRISPR/Cas9 in *Drosophila*. To implement this method, we developed a toolkit for generating and evaluating enhancer-driven Cas9 lines, created convenient cloning vectors for making efficient multi-gRNA transgenes, and established an assay for assessing the mutagenic efficiency of transgenic gRNAs. Using our CRISPR-TRiM tools, we demonstrate that post-mitotic knockout of *Ptp69D* is sufficient to cause LOF in neurons, while SNARE complex components are strongly redundant and perdurant in supporting neuronal dendrite development.

Comparison of CRISPR-TRiM with other tissue-specific LOF methods

Flp/FRT-based mosaic analyses have been widely used for investigating tissue-specific roles of genes in *Drosophila* (42). Among these techniques, MARCM and its variants are considered gold standards for neuronal studies due to the positive labeling of homozygous mutant cells and the single cell resolution they offer (1, 43). However, MARCM and other Flp/FRT-based mosaic analyses also have some obvious limitations. First, they require preexisting mutations in the gene of interest recombined with FRT on the appropriate chromosome arm. Second, because these techniques rely on mitotic chromosome crossovers which would result in wildtype “twin spots”, it is impossible to remove gene function in every cell of the tissue of interest. Third, these techniques require at least five genetic components in the final genotype, making it harder to introduce additional components. Lastly, generating cells mutant for multiple genes located on different chromosome arms is extremely difficult, if not impossible. In contrast, the bipartite CRISPR-TRiM system requires only transgenic components that are independent of all existing binary expression systems. Using efficient Cas9 and gRNA

reagents, LOF in all cells of the target tissue can be expected. These features make CRISPR-TRiM much more convenient than traditional mosaic-based methods.

Compared to *UAS-Cas9* driven by tissue-specific Gal4s, at least with the *ppk* enhancer, the CRISPR-TRiM system has the advantages of faster Cas9 expression (and therefore more complete LOF) and decreased cytotoxicity due to lower Cas9 expression levels. These advantages of enhancer-driven Cas9 are likely more important for studying early gene function in neuronal morphogenesis. An additional benefit of using enhancer-driven Cas9 in CRISPR-TRiM is that the Gal4/UAS system is available for other genetic manipulations in the same experiment.

In the last decade, several genome-wide *UAS-RNAi* resources have greatly accelerated gene identification and characterization in *Drosophila* (2, 3). However, RNAi results in incomplete LOF and suffers from off-target effects (5). In comparison, CRISPR methods can generate true gene knockout, and ever-improving gRNA selection algorithms have mostly mitigated the off-target effects (44-46). In addition, *UAS-Dcr-2* overexpression, which is often necessary for maximizing the knockdown efficiency of dsRNAs, can also cause deleterious effects in the expressing cells. The CRISPR-TRiM method can avoid most of these concerns.

Caveats of CRISPR-TRiM and potential solutions

Due to the nature of CRISPR/Cas9-induced mutagenesis, CRISPR-TRiM will generate tissues composed of heterogenous cells carrying different mutations. This mosaicism could complicate phenotypic analysis, given that different mutations could impact gene function in diverse ways. Although immunostaining could alleviate this problem by revealing whether individual cells make the final protein product, antibodies are not always available nor are all

assays compatible with immunostaining. For this reason, we recommend the use of at least two gRNAs for each target gene to enhance the chance of mutagenesis.

Nonetheless, even with multiple efficient gRNAs we observed that CRISPR-TRiM sometimes produced variable phenotypes among cells (e.g. *Nsf1 Nsf2* knockout by *ppk-Cas9*, Figures 3.6G, L), likely due to the differences in the timing of mutagenesis and/or the nature of the mutations induced in different cells. This variability could actually be beneficial for the analysis of tissues like da neurons where each cell can be evaluated separately: The mosaicism could reveal a fuller spectrum of phenotypes associated with different strengths of LOF. Moderately efficient gRNAs could potentially be exploited for this purpose.

Designing efficient gRNA constructs and assessing gRNA efficiency

Our comparison of several dual-gRNA designs using the same targeting sequences revealed that the tgFE design is particularly efficient for mutagenesis in larval sensory neurons. We found that the same design also performs well in other somatic tissues (data not shown). The tgFE design combines tRNA-processing for releasing multiple gRNAs from a single transcript (20, 29) and F+E modifications in the gRNA scaffold (23). Because the F+E gRNA scaffold has been found to greatly enhance Cas9-mediated gene editing in worms (47) and the use of tRNA in polycistronic gRNAs did not seem by itself to enhance mutagenesis (20), the tgFE design's high efficiency is likely due to the F+E gRNA scaffold. Whether this design also works well in the germ line for creating heritable mutations remains to be determined.

Although large deletions induced by two gRNAs would be more effective in causing LOF, we found that the frequency of large deletions in somatic cells is too low to be reliable. Therefore, to maximize the chance of LOF mutagenesis, we recommend selecting targeting sites in coding sequences shared by all protein isoforms, preferably in conserved protein domains. In

our experience, choosing common top hits by using multiple experimentally-validated gRNA selection algorithms (44, 48, 49) usually yield very efficient gRNAs.

We also recommend evaluating the *in vivo* efficiency of gRNA lines using the Cas9-LEThAL assay before conducting CRISPR-TRiM analyses. In our hands, the lethal phase of male progeny in this assay reliably indicates gRNA efficiency for our CRISPR-TRiM experiments.

CRISPR-TRiM reveals gene functions in neuronal morphogenesis

We provide two examples of CRISPR-TRiM analysis in dendrite morphogenesis of C4da neurons. Our results show that the timing of mutagenesis and the perdurance of gene products influence the extent of LOF; therefore, these parameters must be considered when choosing the most appropriate *Cas9* line. The CRISPR-TRiM analysis of *Ptp69D* shows that post-mitotic mutagenesis is sufficient to cause its LOF, because Ptp69D either is expressed late in neuronal development or turns over quickly. In contrast, SNARE components are made early in the neuronal lineage and are highly perdurant. The early-acting *SOP-Cas9* therefore is required to reveal SNARE LOF phenotypes in neurons. Moreover, we found that dendrite regrowth of adult C4da neurons provides an opportunity to unmask fully the requirements of SNARE components for dendrite morphogenesis. This technique should be useful for circumventing potential perdurance because gene products are removed by dendrite pruning prior to the regrowth. Our results imply that perdurance could be an underappreciated concern for studying development roles of housekeeping genes in any mutation-based LOF analysis.

The potential redundancy of SNARE components in neuronal morphogenesis have been mostly elusive. The *SNAP-25* gene family encodes the Qbc.IV subgroup of SNAREs in metazoa and are thought to mediate all secretions (40). The roles of *Drosophila Snap24* and *Snap25* in

dendrite growth of da neurons have been investigated by RNAi but knockdown of each gene only resulted in minor defects (50). At the neuromuscular junction, *Snap25* mutations were found to cause defective synaptic transmission only in pharate adults, prompting the hypothesis that *Snap24* and *Snap25* play redundant roles in larval neurotransmission (51). However, due to the inability to remove multiple SNAP genes, these previous studies were unable to determine whether *Drosophila* SNAP genes are redundant in neural development. CRISPR-TRiM allowed us to mutate SNAP genes in combination. Our results show that SNAP genes are highly redundant in C4da neurons and the removal of all three genes is required to block all dendrite branching morphogenesis. Our NSF LOF data demonstrate that Nsf1 and Nsf2 also play redundant roles in C4da neurons, which is consistent with the previous finding that these two genes can substitute for each other in the nervous system (39). Of interest, we observed a distinction between NSF and SNAP LOF phenotypes. Both with *SOP-Cas9* in the larva and *ppk-Cas9* in the adult, SNAP LOF appears to produce a more severe dendritic reduction than NSF LOF. This distinction likely reflects the different roles of these proteins in the SNARE machinery. Because NSFs are responsible for recycling the SNARE complex after membrane fusion, newly synthesized SNARE components can still mediate vesicle fusion in the absence of NSFs. In contrast, SNAP LOF causes secretion to stop completely, thereby generating a stronger phenotype.

The *Drosophila* genome contains a large number of paralogous genes that may carry redundant functions. The lack of efficient ways to remove multiple genes simultaneously in specific tissues has hampered the characterization of these genes in development. The CRISPR-TRiM tools we present here offer an efficient and convenient way for investigating not only developmental roles of individual genes, but also those of potential redundant gene groups.

These tools can be applied to address a broad range of developmental, cell biological, and physiological questions in *Drosophila*.

ACKNOWLEDGEMENTS

We thank Ying Peng, Yi Guo, and Bloomington Stock Center for fly stocks; Norbert Perrimon and Addgene for plasmids; Michael Goldberg, Mariana Wolfner, David Deitcher, Dion Dickman, and Quan Yuan for critical reading and suggestions on the manuscript. This work was supported by a Cornell Fellowship awarded to H.J.; a Cornell start-up fund and NIH grants (R01NS099125 and R21OD023824) awarded to C.H.

METHODS

Fly Stocks

ppk-Gal4 (52), *UAS-CD4-tdTom* (24), *UAS-CD4-tdGFP* (24), *UAS-Cas9* (19), *UAS-Dcr-2* (2), *ppk-CD4-tdGFP* (24), *tub-Gal80* (1), *tubP-Gal4 UAS-CD8-GFP* (1), *Gal4²¹⁻⁷* (53), *gRNA-e* (19) have been described previously. *Act-Gal4* (#3954), *UAS-GFP* (#6658), *UAS-mCherryNLS* (#38425), *UAS-RedStinger* (#8547), *nsyb-Gal4* (#39171), *Act-Cas9 w lig4* (#58492), *R28E04-Gal4* (#45169) were obtained from Bloomington Stock Center (BDSC). *ppk-Cas9*, *RluA1-Cas9*, *SOP-Cas9*, *hh-Cas9*, *nsyb-tdGFP*, and various gRNA lines were made in this study.

To compare different gRNA-GFP designs, the strain *w; RluA1-Cas9; nsyb-GAL4 UAS-CD8-GFP* were crossed to various gRNA-GFP lines. To visualize large DNA deletions in individual neurons, *y Act5C-Cas9 w; nsyb-tdGFP^{VK37}* and *y Act5C-Cas9 w; nsyb-tdGFP^{VK33}* were crossed to various gRNA lines. *gRNA-Gal80* was used as *gRNA-0*.

Cas9-LEThAL assay

Act-Cas9 w lig4 homozygous females were crossed to *gRNA* homozygous males. The crosses were transferred several times to collect embryos in plastic vials on standard media. The embryo

density was controlled at around 100 embryos per vial. The vials were monitored daily and animal lethal phases were recorded. If animals could pupariate, we counted the numbers of dead prepupae (before head eversion), dead pupae (post head eversion), dead pharate adults, and eclosed adults. For each lethal phase, we counted at least 100 animals for each cross.

Molecular Cloning

pDEST-APIC-Cas9: A synthetic core promoter containing Hsp70 core promoter, Inr, MTE, and DPE was synthesized as a gBlock fragment (Integrated DNA Technologies, Inc.) and was used to replace the Hsp70 core promoter of pDEST-HemmarR (24). The CD4-tdTom coding sequence of the resulting plasmid was then replaced with a fragment containing the *Streptococcus pyogenes* Cas9 coding sequence and two in-frame nuclear localization signals at both N- and C-termini of Cas9, which was amplified by PCR from pnos-Cas9 (10) (a gift from Norbert Perrimon).

Enhancer entry vectors: pENTR-ppk was previously described (24). The R28E04 enhancer was PCR amplified from R28E04-Gal4 genomic DNA and was combined with pDONR221 (Thermo Fisher Scientific) to make pENTR-hh through a Gateway BP reaction. The pENTR-RluA1 was made similarly using a 3.2 kb RluA1 enhancer that was PCR amplified from *w¹¹¹⁸* genomic DNA. The SOP enhancer contains 8 copies of *sc-E1* element (32) and was cloned into Sall/XhoI sites of pENTR11 (Thermo Fisher Scientific).

Cas9 expression vectors: ppk-Cas9, RluA1-Cas9, SOP-Cas9, hh-Cas9 expression vectors were generated by Gateway LR reactions using the appropriate entry vectors and a Cas9 destination vector which is similar to pDEST-APIC-Cas9 but does not contain Inr, MTE, and DPE in the Hsp70 core promoter.

nsyb-tdGFP: pAPIC-CD4-tdGFP (24) was digested by SphI and BamHI and assembled with a nsyb enhancer fragment, which was PCR-amplified from *R57C10-Gal4* genomic DNA, and a Hsp70 core promoter-intron fragment using NEBuilder DNA Assembly (New England Biolabs).

gRNA cloning vectors: Four gRNA cloning vectors were made using a pAC (attB-CaSpeR4) vector derived from pCaSpR4 (54). pCFD4-U61-U63(19) was first digested by BbsI and then ligated with a SapI adapter made with annealed complementary oligos. A BglIII-XbaI fragment from the resulting plasmid was isolated and cloned into BamHI/XbaI sites of pAC to make pAC-U61-SapI (i.e. Forward). An SpeI-XbaI fragment containing U6:1 promoter, SapI adapter, gRNA scaffold, and U6 3' flanking sequence was then isolated from pAC-U61-SapI and ligated back to SpeI/XbaI digested pAC-U61-SapI in the reverse orientation to make pAC-U61-SapI-Rev (i.e. Reverse). A Gypsy insulator fragment was PCR amplified from pEDST-HemmarR (24) and cloned into EcoR/SpeI sites of pAC-U61-SapI to make pAC-U61-SapI-In (i.e. Insulated). To make pAC-U63-tgRNA-Rev (i.e. tgFE), a DNA fragment containing *Drosophila* Gly tRNA, SapI adapter, the (F+E) gRNA scaffold, and U6 3' flanking sequence was synthesized as a gBlock (Integrated DNA Technologies, Inc.) and assembled with SapI/XbaI digested pAC-U63-SapI using NEBuilder DNA Assembly. The resulting plasmid was then digested by XbaI/SpeI, followed by re-ligation of the insert and the backbone in the reversed orientation.

gRNA PCR template vectors: Three PCR template vectors were made for generating PCR fragments used for assembling the final gRNA expression vectors. pTGC-U62 and pTGC-U63 are for cloning up to 3 gRNAs driven by separate U6 promoters in one construct (in Forward, Reverse, or Insulated design). pMGC is for making multiplex tRNA-gRNA vectors using the tgFE design. Each of these vectors were made by assembling a synthetic gBlock DNA fragment with a PCR-amplified Kanamycin-resistant backbone using NEBuilder DNA Assembly. The

region to be PCR-amplified from pTGC-U62 contains the conventional gRNA scaffold, PolIII transcription terminator, and U6:2 promotor (19). The region to be PCR-amplified from pTGC-U63 contains the conventional gRNA scaffold, PolIII transcription terminator, and U6:3 promotor (19). The region to be PCR-amplified from pMGC contains the (F+E) gRNA scaffold (23) and rice Gly tRNA(20).

Cloning of gRNA expression vectors: Primers were designed according to Table S4 and used to generate PCR products with the appropriate gRNA PCR template vectors. The PCR products were then assembled with SapI-digested gRNA cloning vectors using NEBuilder DNA Assembly.

***Drosophila* Transgenic Lines**

Injections were carried out by Rainbow Transgenic Flies. Cas9 expression vectors were transformed using P-element-mediated random insertions. *nsyb-tdGFP* was generated by Φ C31-mediated integration at attP^{VK37} and attP^{VK33} sites. Unless noted otherwise, gRNA expression vectors were integrated into the attP^{VK27} site.

Identification of gRNA target sequence

We used two gRNA prediction tools, sgRNA Scorer 2.0 (48) (<https://crispr.med.harvard.edu>) and Benchling (www.benchling.com), to identify candidate gRNA target sequences that have high on-target scores in both algorithms. Target sequences predicted to have more than one target site by CasFinder (55) were rejected. For each gene, we selected two target sequences that are against coding exons of all splicing isoforms. We prefer to use target sequences in the first half of common coding exons. All targeting sequences designed by this study are listed in Table S3.

Live Imaging

Snapshot live imaging of larval da neurons was performed as described previously (4). Briefly, animals were reared at 25°C in density-controlled vials. Third instar larvae at 96 hr AEL (unless specified otherwise) were mounted in glycerol and imaged with a Leica SP8 confocal. For dendritic phenotypes, the A2-A3 segments of 8-10 larvae were imaged for each genotype using a 20X oil objective. For all other experiments, the A1-A4 segments of 5-6 larvae were imaged for each genotype using a 40X oil objective. To image larvae younger than 72 hr AEL, larvae were anesthetized by isoflurane for 2 minutes & then mounted in halocarbon oil.

To image day 0 adults, the wings of newly eclosed male and female flies were removed. A thin layer of vacuum grease was placed on a glass slide and flies were then mounted with the dorsal side pressed into the grease. A small amount of UV glue (glue NOA61; Norland) was then added to the ventral side of the animal (about 0.1 μ L) and a coverslip was placed on top of the animals and pressed slightly. Then, the glue was cured by UV light (a modified version of WorkStar 2003 NDT 365 nm UV-A Inspection Light) at Hi setting for 30 seconds. V'ada neurons of the abdominal segments were then imaged using a 40X oil objective.

Imaginal disc imaging

Dissection of imaginal discs was performed as described previously(56). Briefly, wandering 3rd instar larvae were dissected in a small petri dish filled with PBS. The anterior half of the larva was inverted and the trachea and gut were removed. The sample was then transferred to 4% formaldehyde in PBS and fixed for 15 minutes at room temperature. After washing with PBS, the imaginal discs were placed in SlowFade Diamond Antifade Mountant (Thermo Fisher Scientific) on a glass slide. A coverslip was slightly pressed on top and the discs were imaged using a 40X oil objective.

Image analysis and quantification

Tracing and measuring of C4da dendrites was performed as described previously (4). Briefly, for tracing and measuring C4da dendrites (Figure 3.5G, Figure 3.6, and Figure 3.7) in Fiji/ImageJ, images of dendrites (1,024 X 1,024 pixels) taken with a 20X objective were first processed by Gaussian Blur (Sigma: 0.8) and then Auto Local Threshold (Phansalkar method, radius: 50). Isolated particles below the size of 120 pixels were removed by the Particles4 plugin (<http://www.mecourse.com/landinig/software/software.html>). The dendrites were then converted to single-pixel-width skeletons using the Skeletonize (2D/3D) plugin and processed using Analyze Skeleton (2D/3D) plugin. The length of skeletons was calculated based on pixel distance; terminal dendrites in the dendritic field or regions of interest were counted based on the endings of terminal dendrites. Skeletons of terminal dendrites in regions of interest were isolated using the Strahler Analysis plugin (http://imagej.net/Strahler_Analysis). Dendrite density was calculated using the formula: $1000 \times \text{dendritic length } (\mu\text{m}) / \text{dendritic area } (\mu\text{m}^2)$; normalized terminal dendrite number was calculated using the formula: $1000 \times \text{terminal dendrite number} / \text{dendritic area } (\mu\text{m}^2)$.

The GFP fluorescence intensity of neurons were measured in Fiji/ImageJ (Figure 3.2, Figure 3.3, and Figure 3.5). Z-stack images were taken for each dorsal sensory cluster with a 40X oil objective. The slice with the brightest and most uniform GFP signal at the cell body and primary dendrites of the neuron of interest was identified and a region of interest (ROI) was defined at the cell body or primary dendrites. For experiments involving negative testers, regions overlapping with neuronal nuclei were not included in the ROIs in order to avoid potential bleed-through from the RFP channel. To identify cell bodies that had very weak fluorescence, the images were first brightened up using the Brightness/Contrast tool.

To count GFP-positive neurons in Figure 3.4, each slice in image stacks was inspected and all visible cell bodies were counted as GFP-positive neurons. The identities of missing PNS neurons were estimated based on relative cell body locations in the PNS dorsal cluster.

Statistical Analysis

R was used to perform one-way analysis of variance (ANOVA) with Tukey's HSD test for most experiments (unless specified otherwise). Excel was used to perform Student's t-test where indicated.

REFERENCES

1. Lee T & Luo L (1999) Mosaic analysis with a repressible cell marker for studies of gene function in neuronal morphogenesis. *Neuron* 22(3):451-461.
2. Dietzl G, *et al.* (2007) A genome-wide transgenic RNAi library for conditional gene inactivation in Drosophila. *Nature* 448(7150):151-156.
3. Ni JQ, *et al.* (2011) A genome-scale shRNA resource for transgenic RNAi in Drosophila. *Nat Methods* 8(5):405-407.
4. Poe AR, *et al.* (2017) Dendritic space-filling requires a neuronal type-specific extracellular permissive signal in Drosophila. *Proc Natl Acad Sci U S A* 114(38):E8062-E8071.
5. Ma Y, Creanga A, Lum L, & Beachy PA (2006) Prevalence of off-target effects in Drosophila RNA interference screens. *Nature* 443(7109):359-363.
6. Jinek M, *et al.* (2012) A programmable dual-RNA-guided DNA endonuclease in adaptive bacterial immunity. *Science* 337(6096):816-821.
7. Bassett AR, Tibbit C, Ponting CP, & Liu JL (2013) Highly efficient targeted mutagenesis of Drosophila with the CRISPR/Cas9 system. *Cell Rep* 4(1):220-228.
8. Gratz SJ, *et al.* (2013) Genome engineering of Drosophila with the CRISPR RNA-guided Cas9 nuclease. *Genetics* 194(4):1029-1035.
9. Yu Z, *et al.* (2013) Highly efficient genome modifications mediated by CRISPR/Cas9 in Drosophila. *Genetics* 195(1):289-291.
10. Ren X, *et al.* (2013) Optimized gene editing technology for Drosophila melanogaster using germ line-specific Cas9. *Proc Natl Acad Sci U S A* 110(47):19012-19017.
11. Kondo S & Ueda R (2013) Highly improved gene targeting by germline-specific Cas9 expression in Drosophila. *Genetics* 195(3):715-721.
12. Sebo ZL, Lee HB, Peng Y, & Guo Y (2014) A simplified and efficient germline-specific CRISPR/Cas9 system for Drosophila genomic engineering. *Fly (Austin)* 8(1):52-57.
13. Gaj T, Gersbach CA, & Barbas CF, 3rd (2013) ZFN, TALEN, and CRISPR/Cas-based methods for genome engineering. *Trends Biotechnol* 31(7):397-405.
14. Gratz SJ, *et al.* (2014) Highly specific and efficient CRISPR/Cas9-catalyzed homology-directed repair in Drosophila. *Genetics* 196(4):961-971.

15. Xue Z, *et al.* (2014) Efficient gene knock-out and knock-in with transgenic Cas9 in *Drosophila*. *G3 (Bethesda)* 4(5):925-929.
16. Ghosh S, Tibbit C, & Liu JL (2016) Effective knockdown of *Drosophila* long non-coding RNAs by CRISPR interference. *Nucleic Acids Res* 44(9):e84.
17. Ewen-Campen B, *et al.* (2017) Optimized strategy for in vivo Cas9-activation in *Drosophila*. *Proc Natl Acad Sci U S A* 114(35):9409-9414.
18. Xue Z, *et al.* (2014) CRISPR/Cas9 mediates efficient conditional mutagenesis in *Drosophila*. *G3 (Bethesda)* 4(11):2167-2173.
19. Port F, Chen HM, Lee T, & Bullock SL (2014) Optimized CRISPR/Cas tools for efficient germline and somatic genome engineering in *Drosophila*. *Proc Natl Acad Sci U S A* 111(29):E2967-2976.
20. Port F & Bullock SL (2016) Augmenting CRISPR applications in *Drosophila* with tRNA-flanked sgRNAs. *Nat Methods* 13(10):852-854.
21. Jiang W, Brueggeman AJ, Horken KM, Plucinak TM, & Weeks DP (2014) Successful transient expression of Cas9 and single guide RNA genes in *Chlamydomonas reinhardtii*. *Eukaryot Cell* 13(11):1465-1469.
22. Ren X, *et al.* (2014) Enhanced specificity and efficiency of the CRISPR/Cas9 system with optimized sgRNA parameters in *Drosophila*. *Cell Rep* 9(3):1151-1162.
23. Chen B, *et al.* (2013) Dynamic imaging of genomic loci in living human cells by an optimized CRISPR/Cas system. *Cell* 155(7):1479-1491.
24. Han C, Jan LY, & Jan YN (2011) Enhancer-driven membrane markers for analysis of nonautonomous mechanisms reveal neuron-glia interactions in *Drosophila*. *Proc Natl Acad Sci U S A* 108(23):9673-9678.
25. Jenett A, *et al.* (2012) A GAL4-driver line resource for *Drosophila* neurobiology. *Cell Rep* 2(4):991-1001.
26. Kvon EZ, *et al.* (2014) Genome-scale functional characterization of *Drosophila* developmental enhancers in vivo. *Nature* 512(7512):91-95.
27. Weiler KS & Wakimoto BT (1995) Heterochromatin and gene expression in *Drosophila*. *Annu Rev Genet* 29:577-605.
28. Grueber WB, Ye B, Moore AW, Jan LY, & Jan YN (2003) Dendrites of distinct classes of *Drosophila* sensory neurons show different capacities for homotypic repulsion. *Curr Biol* 13(8):618-626.
29. Xie K, Minkenberg B, & Yang Y (2015) Boosting CRISPR/Cas9 multiplex editing capability with the endogenous tRNA-processing system. *Proc Natl Acad Sci U S A* 112(11):3570-3575.
30. Grueber WB, Jan LY, & Jan YN (2002) Tiling of the *Drosophila* epidermis by multidendritic sensory neurons. *Development* 129(12):2867-2878.
31. Pfeiffer BD, Truman JW, & Rubin GM (2012) Using translational enhancers to increase transgene expression in *Drosophila*. *Proc Natl Acad Sci U S A* 109(17):6626-6631.
32. Powell LM, Zur Lage PI, Prentice DR, Senthinathan B, & Jarman AP (2004) The proneural proteins Atonal and Scute regulate neural target genes through different E-box binding sites. *Mol Cell Biol* 24(21):9517-9526.
33. Pastor-Pareja JC & Xu T (2011) Shaping cells and organs in *Drosophila* by opposing roles of fat body-secreted Collagen IV and perlecan. *Dev Cell* 21(2):245-256.

34. Lee HB, Sebo ZL, Peng Y, & Guo Y (2015) An optimized TALEN application for mutagenesis and screening in *Drosophila melanogaster*. *Cell Logist* 5(1):e1023423.
35. Culi J & Modolell J (1998) Proneural gene self-stimulation in neural precursors: an essential mechanism for sense organ development that is regulated by Notch signaling. *Genes Dev* 12(13):2036-2047.
36. Lai EC & Orgogozo V (2004) A hidden program in *Drosophila* peripheral neurogenesis revealed: fundamental principles underlying sensory organ diversity. *Dev Biol* 269(1):1-17.
37. Desai CJ, Popova E, & Zinn K (1994) A *Drosophila* receptor tyrosine phosphatase expressed in the embryonic CNS and larval optic lobes is a member of the set of proteins bearing the "HRP" carbohydrate epitope. *J Neurosci* 14(12):7272-7283.
38. Wickner W & Schekman R (2008) Membrane fusion. *Nat Struct Mol Biol* 15(7):658-664.
39. Golby JA, Tolar LA, & Pallanck L (2001) Partitioning of N-ethylmaleimide-sensitive fusion (NSF) protein function in *Drosophila melanogaster*: dNSF1 is required in the nervous system, and dNSF2 is required in mesoderm. *Genetics* 158(1):265-278.
40. Kloepper TH, Kienle CN, & Fasshauer D (2007) An elaborate classification of SNARE proteins sheds light on the conservation of the eukaryotic endomembrane system. *Mol Biol Cell* 18(9):3463-3471.
41. Shimono K, *et al.* (2009) Multidendritic sensory neurons in the adult *Drosophila* abdomen: origins, dendritic morphology, and segment- and age-dependent programmed cell death. *Neural Dev* 4:37.
42. Griffin R, Binari R, & Perrimon N (2014) Genetic odyssey to generate marked clones in *Drosophila* mosaics. *Proc Natl Acad Sci U S A* 111(13):4756-4763.
43. Yu HH, Chen CH, Shi L, Huang Y, & Lee T (2009) Twin-spot MARCM to reveal the developmental origin and identity of neurons. *Nat Neurosci* 12(7):947-953.
44. Doench JG, *et al.* (2016) Optimized sgRNA design to maximize activity and minimize off-target effects of CRISPR-Cas9. *Nat Biotechnol* 34(2):184-191.
45. Haeussler M, *et al.* (2016) Evaluation of off-target and on-target scoring algorithms and integration into the guide RNA selection tool CRISPOR. *Genome Biol* 17(1):148.
46. Chari R, Mali P, Moosburner M, & Church GM (2015) Unraveling CRISPR-Cas9 genome engineering parameters via a library-on-library approach. *Nat Methods* 12(9):823-826.
47. Zhao P, *et al.* (2016) One-step homozygosity in precise gene editing by an improved CRISPR/Cas9 system. *Cell Res* 26(5):633-636.
48. Chari R, Yeo NC, Chavez A, & Church GM (2017) sgRNA Scorer 2.0: A Species-Independent Model To Predict CRISPR/Cas9 Activity. *ACS Synth Biol* 6(5):902-904.
49. Moreno-Mateos MA, *et al.* (2015) CRISPRscan: designing highly efficient sgRNAs for CRISPR-Cas9 targeting in vivo. *Nat Methods* 12(10):982-988.
50. Peng Y, *et al.* (2015) Regulation of dendrite growth and maintenance by exocytosis. *J Cell Sci* 128(23):4279-4292.
51. Vilinsky I, Stewart BA, Drummond J, Robinson I, & Deitcher DL (2002) A *Drosophila* SNAP-25 null mutant reveals context-dependent redundancy with SNAP-24 in neurotransmission. *Genetics* 162(1):259-271.
52. Han C, *et al.* (2012) Integrins regulate repulsion-mediated dendritic patterning of *Drosophila* sensory neurons by restricting dendrites in a 2D space. *Neuron* 73(1):64-78.

53. Song W, Onishi M, Jan LY, & Jan YN (2007) Peripheral multidendritic sensory neurons are necessary for rhythmic locomotion behavior in *Drosophila* larvae. *Proc Natl Acad Sci U S A* 104(12):5199-5204.
54. Thummel CS & Pirrotta V (1992) New pCaSpeR P-element vectors. *Drosophila Inf. Serv.* 71:150.
55. Aach J, Mali P, & Church GM (2014) CasFinder: Flexible algorithm for identifying specific Cas9 targets in genomes. *bioRxiv*.
56. Han C, Belenkaya TY, Wang B, & Lin X (2004) *Drosophila* glypicans control the cell-to-cell movement of Hedgehog by a dynamin-independent process. *Development* 131(3):601-611.

CHAPTER 4

Suppression of FoxO expression and autophagy underlies preferential dendrite growth of *Drosophila* neurons during nutrient restriction³

INTRODUCTION

During animal development, the growth of individual organs and tissues must coordinate with overall body growth. In the peripheral nervous system (PNS), the coordination of sensory neuron growth with animal size is particularly important because the neuron must adapt to a constantly growing receptive field in order to properly collect sensory inputs. Under optimal laboratory conditions, peripheral sensory neurons grow their dendritic arbors in coordination with their receptive field in a process called scaling (1). However, nutrient deprivation during development poses a significant challenge to the organism. In response to a reduction in nutrients, many tissues undergo a decline in cell proliferation and growth, resulting in undersized animals (2). Although many organs reach a smaller size when few nutrients are available, growth of some organs is spared (3). During human fetal development, reductions in food availability to the mother result in smaller newborns with disproportionately large heads. In this phenomenon, intra-uterine growth restriction (IUGR), the growth of critical organs such as the brain is spared at the expense of the rest of the body (4). Brain sparing has also been observed in *Drosophila melanogaster* grown under nutrient restriction. Neural stem cells in the central nervous system (CNS) grow and divide preferentially through the activity of the receptor tyrosine kinase, anaplastic lymphoma kinase (Alk) (5). Although organ sparing under nutrient restriction has been observed in other tissues in *Drosophila* including the wing imaginal disc (5) and male

³A version of this chapter will be submitted as Poe, A.R., Xu, Y., Zhang, C., Li, K., Labib, D., Lee, Y., Han, C. Suppression of FoxO expression and autophagy underlies preferential dendrite growth of *Drosophila* neurons during nutrient restriction. Work contributed by Yineng Xu, Christine Zhang, David Labib, and Yuna Lee is denoted in the figure legends. The initial analysis of yeast concentrations was performed by Kailyn Li.

genitalia (6), little is known about how post-mitotic cells respond to the organism's nutritional state. Even less is known about how scaling of dendritic arbors is influenced by the nutritional environment.

The nutritional regulation of dendritic field size likely relies on cross-talk between multiple cell size regulatory pathways including insulin signaling, the Target of rapamycin (TOR) signaling pathway, and amino acid sensing pathways (3). The *Drosophila* fat body plays a key role in communicating nutritional status of the entire organism to the insulin-producing cells (IPCs) in the brain to regulate *Drosophila* insulin-like peptide (Dilp) production (3). When dietary nutrients are abundant, levels of Dilps are high which then activate their receptor, the insulin-like receptor (InR) to promote cell growth through the activity of PI3 kinase (PI3K) and Akt kinase (7). In addition to its role in proliferating cells, the PI3K-Akt pathway also promotes dendrite growth in *Drosophila* sensory neurons (1) and mammalian hippocampal neurons (8, 9). Cells also respond to the amino acid levels in the environment through the TOR kinase which acts in two distinct protein complexes, TORC1 and TORC2. In addition to regulating a variety of biological processes, TORC1 phosphoregulates 4EBP and the p70 ribosomal protein S6 Kinase (S6K) to promote protein synthesis leading to an increase in cell growth (3). TORC2 regulates the actin cytoskeleton (10) and is necessary for preventing dendritic field overlaps in *Drosophila* sensory neurons (11). Although cell-size regulatory pathways play a role in dendritic growth, it is unclear how reductions in nutrients affect dendritic arbor expansion.

The autophagy pathway is a good candidate to examine for a role in regulating neuronal size in low nutrient conditions because autophagy is highly inducible under nutrient deprivation and acts to inhibit cell growth (12). Cells under nutrient stress recycle portions of their own cytoplasm including organelles and other cellular components by delivering these components to

lysosomes for degradation. This process, known as autophagy, occurs through autophagosome formation and subsequent autophagosome-lysosome fusion (13). Autophagy regulation occurs through many mechanisms including TORC1-mediated inhibition and transcriptional regulation by *forkhead box, sub-group O (FoxO)* (10, 14). Additionally, autophagy regulates axon growth in mammalian cortical neurons (15) and is necessary for proper functioning of the *Drosophila* central nervous system (16). However, it is not known how autophagy activation affects peripheral sensory neuron growth and organ sparing under nutrient stress.

The *Drosophila* dendritic arborization (da) neurons are a good model system for investigating the coordination of neuron and non-neural tissue growth under nutrient deprivation. Da neurons develop in a two-dimensional space along the basal surface of epidermal cells (17). Of the four classes of da neurons, the class IV da (C4da) neurons have the most complex branching patterning (18) and scale with the rest of the larval body (19). While C4da dendritic growth relies on both intrinsic and extrinsic mechanisms (20), these mechanisms must coordinate to regulate dendrite growth with the developing larval epidermis. Recent evidence indicates that epidermal cells ensure dendritic scaling through the activity of the microRNA *bantam* (1). This microRNA inhibits neuronal growth at later developmental stages by inhibiting the neuronal PI3K-Akt kinase pathway and altering dendrite-substrate interactions (1, 21). A recent study has found that dendritic branching patterns of C4da neurons become more complex in low-yeast conditions suggesting a dis-coordination between C4da dendrite growth and animal growth (22). However, the molecular mechanisms responsible for this dis-coordination between dendrite growth and larval body growth under nutrient restriction are not well understood.

In this study, we determined that *Drosophila* da neurons exhibit differential responses to nutrient restriction with C3da and C4da neurons growing excessively while overall larval body

growth is delayed. However, as previously reported (22), the branching patterns of C1da neurons were not affected by a reduction in nutrients. We performed a developmental analysis of C4da dendrite growth in low nutrient conditions and determined that preferential dendrite growth occurs later in larval development. This uncoordinated growth between neurons and larval epidermal cells results from differentially regulated InR-Tor signaling in these two tissues. Surprisingly, C4da neurons exhibit preferential suppression of autophagy under nutrient deprivation with epidermal cells showing an increase in autophagosome formation. Finally, we present evidence that FoxO activity likely underlies the differential growth response of C4da neurons and epidermal cells.

RESULTS

C4da neurons exhibit a growth advantage under nutrient restriction

To determine if C4da neurons and the larval body show differential growth responses to nutrient restriction, we examined both C4da neuronal morphology and larval body growth under both low (1% yeast) and high (8% yeast) nutrient conditions. Starting at 48 hours after egg laying (AEL), we examined C4da dendrite growth with *Gal4^{ppk}*-driven *tdTom* and epidermal cell size using the septate junction marker Nrg-GFP every 24 hours (Figures 4.1A-H'). Compared to the 8% yeast condition, the 1% yeast condition caused a significant delay in larval body growth with animals on 1% yeast taking 264 hrs AEL to reach a similar segment size as animals at 120 hrs AEL on 8% yeast (Figure 4.1I). However, as the animals developed, the C4da neurons grew excessively in the 1% yeast condition showing a dramatic increase in total dendrite length compared to the control (Figure 4.1J).

To more accurately measure larval body growth, we first compared three different measurement parameters: total larval body length, segment width, and average epidermal cell

size of each segment. Segment width measures the distance between the tendon cells at the muscle attachment site at the posterior and anterior borders of the segment (shown as a red line in Figure 4.1C). Because epidermal cell size can vary based on the location in the larval body (data not shown), we only measured cells on the dorsal side of each segment (red cells in Figure 4.1C'). Under both yeast conditions, the three measurement parameters correlated tightly (Figures 4.S1A, B) as the larvae grew in size. Therefore, we used segment width measurement as an indicator of animal size.

We next wanted to determine how C4da neuron growth changes as the animal develops in both nutrient conditions. Early in larval development, total dendrite length was similar between the two yeast conditions (Figure 4.1K). However, dendrite density (defined as dendritic length per unit area) in the 1% yeast condition was higher throughout development based on either the segment width of the animal (Figure 4.1L) or the average epidermal cell size (Figure 4.S1C). This increase in dendrite density likely reflects differences in total animal width on the two conditions with animals on the 1% yeast being visibly thinner (data not shown). Compared to the 8% yeast condition, the 1% yeast condition caused an increase in dendrite growth in the larger animals (Figures 1.1K, L). In both conditions, dendrite density was less variable when the segment width size is between 500-550 microns, providing the most consistent comparison between the two nutrient conditions. Therefore, for subsequent experiments, we chose to compare dendrite density in animals with segment widths between 500-550 microns. Together, our results indicate that C4da neurons preferentially grow dendrites under nutrient restriction.

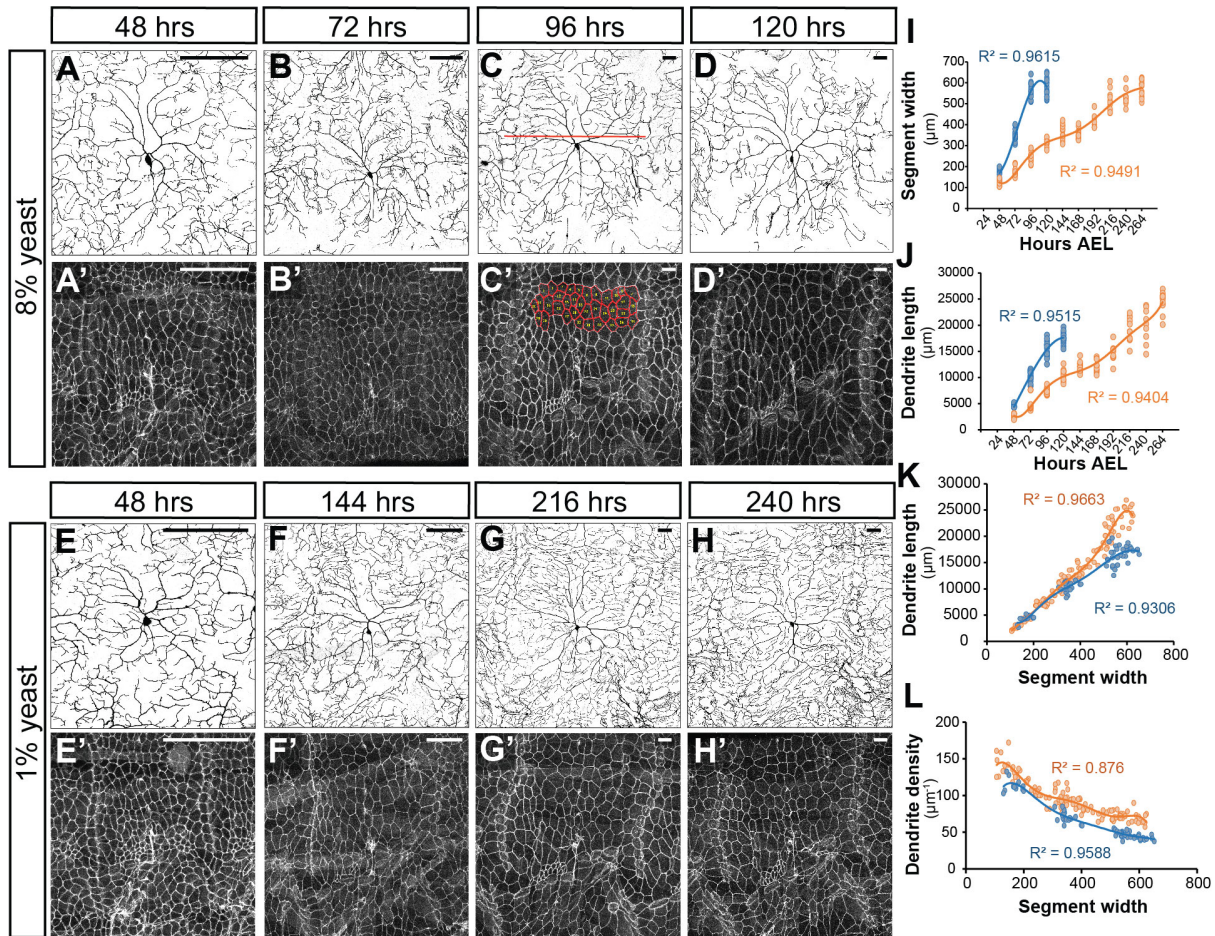


Figure 4.1. C4da neurons exhibit a growth advantage under nutrient deprivation.

(A-D') DdaC dendritic fields (A-D) and expression of Nrg-GFP (A'-D') in animals grown on 8% yeast at four developmental stages. The red line in (C) represents sample segment width measurement. Red epidermal cells in (C') represent sample epidermal cell quantification. (E-H') DdaC dendritic fields (E-H) and expression of Nrg-GFP (E'-H') of animals grown on 1% yeast at four developmental stages. (I) Quantification of segment width at different time points after egg laying (AEL) for animals grown on 8% and 1% yeast. (J) Quantification of total dendrite length at different time points AEL for animals grown on 8% and 1% yeast. (K and L) Quantification of total dendrite length (K) and total dendrite density (L) in relation to segment width. For all quantifications, blue circles represent animals grown on 8% yeast and orange circles represent animals grown on 1% yeast. Each circle represents a neuron. R-square values indicate correlation coefficients for the trendline. Scale bars represent 100 microns in (A-A'), (B-B'), (E-E'), and (F-F'). Scale bars represent 50 microns in (C-C'), (D-D'), (G-G'), and (H-H'). Nrg-GFP was detected using a GFP trap line. Imaging was performed by Christine Zhang, David Labib, and Amy Poe. Quantifications were performed by Christine Zhang and Amy Poe.

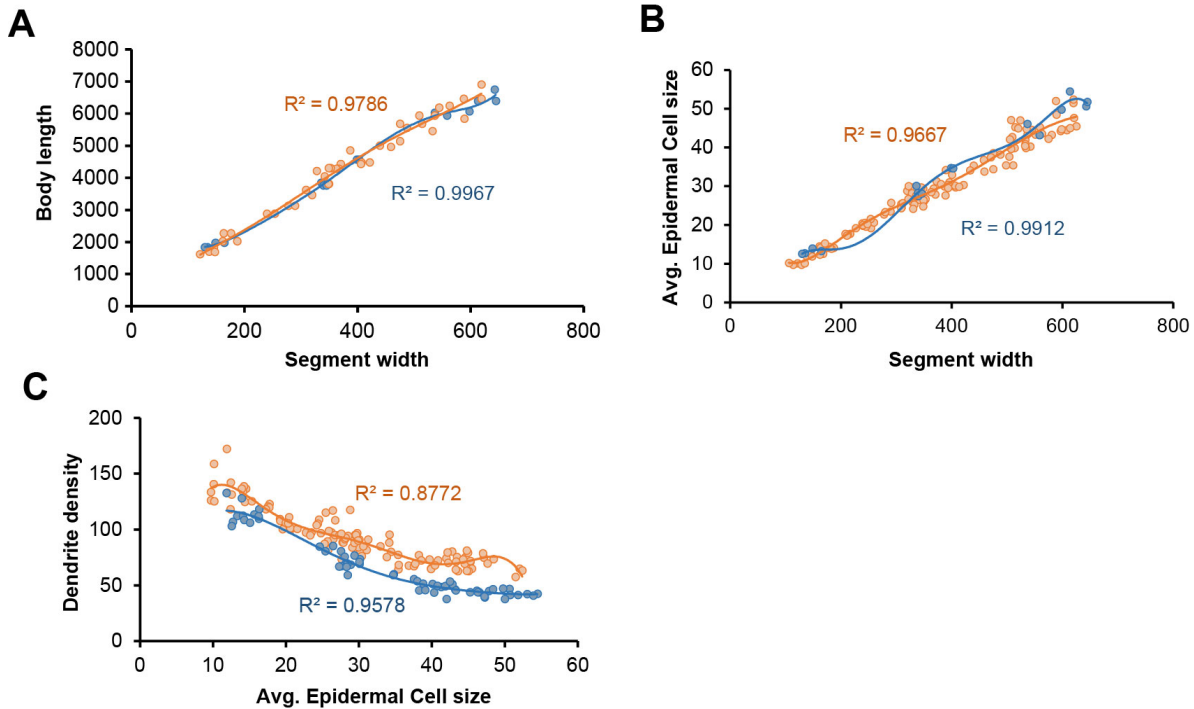


Figure 4.S1. Segment width provides a reliable measurement of animal size.

(A) Quantification of total animal length in relation to segment width. (B) Quantification of average epidermal cell size in relation to segment width. (C) Quantification of total dendrite density in relation to average epidermal cell size. For all quantifications, blue circles represent animals grown on 8% yeast and orange circles represent animals grown on 1% yeast. Each circle represents a neuron. R-square values indicate correlation coefficients for the trendline. Imaging was performed by Christine Zhang, David Labib, and Amy Poe. Quantifications were performed by Christine Zhang and Amy Poe.

Preferential neuronal growth relies on InR-Tor signaling

The insulin/IGF signaling pathway is important for coordinating cell growth with nutritional conditions (7). To determine if insulin signaling is necessary for the preferential growth of C4da neurons in the 1% yeast condition, we knocked down *Insulin-like receptor (InR)* (Figures 4.2B, E) by RNA interference (RNAi) using a C4da-neuron specific driver *Gal4^{ppk}*. We also expressed a version of *InR* containing a dominant negative (DN) K1409A protein variant (*UAS-InR-DN*) (Figures 4.S2B, E) in C4da neurons using the same *Gal4^{ppk}*. Compared to the

control (Figures 4.2A, D), *ppk>InR* RNAi and *ppk>InR-DN* caused a reduction in dendrite growth (Figure 4.2G), but did not affect the coverage index (defined as the dendritic field area divided by the total receptive field area) (Figure 4.S2G) indicating that the dendritic arbor develops normally. However, the dendrite density ratio (defined as the average dendrite density on 1% divided by the average dendrite density on 8%) was reduced in *ppk>InR* RNAi and *ppk>InR-DN* (Figures 4.2H). This data indicates that the LOF of InR signaling affects neurons more severely on the 1% than 8% yeast conditions.

The protein kinase Target of rapamycin (TOR) is the main regulator of cell growth in response to nutrient conditions. TOR is regulated by many nutritional signals including insulin levels through InR signaling (2) and amino acid levels (23). We next determined if Tor signaling is also underlying the preferential C4da dendrite growth under nutrient stress by expressing *Tor* RNAi and a dominant negative form of *Tor* (*UAS-dTor^{TED}*) (24) using the same *Gal4^{ppk}*. Compared to the control (Figures 4.2A, D), *ppk>Tor* RNAi (Figures 4.2C, F) and *ppk>Tor^{TED}* (Figures 4.S2C, F) caused a reduction in dendrite growth (Figure 4.2G) and did not affect the coverage index (Figure 4.S2G). Moreover, the dendrite density ratio was reduced in both *ppk>Tor* RNAi and *ppk>Tor^{TED}* (Figure 4.2H) indicating that Tor LOF affects dendrite growth more severely on the 1% yeast condition. Together, this data suggests that InR-Tor signaling is necessary for the preferential growth of C4da dendrites under nutrient stress.

To demonstrate that altering the relative growth rates of epidermal cells and neurons is sufficient to change the dendrite density, we tried to slow down epidermal cell growth on 8% yeast by knocking down *InR* or overexpressing *InR-DN* in a stripe of epidermal cells in the middle of the segment using *Gal4^{R16D01}*. We then examined the cell size of both the RNAi-expressing cells and wildtype epidermal cells in the same segment using the septate junction

marker Nrg-GFP. Compared to the control (Figures 4.2I, L), these manipulations effectively reduced epidermal cell sizes (Figures 4.2J, M, O and 4.S2I, L) on both yeast conditions. Additionally, reducing Tor signaling with *R16D01>Tor* RNAi (Figures 4.2K, N) or *R16D01>-dTor^{TEED}* (Figures 4.S2J, M) overexpression also reduced epidermal cell size in both yeast conditions (Figure 4.2O). Interestingly, the reduction in average cell size was more severe in the 1% yeast condition (Figure 4.2O) which suggests that cells may be more sensitive to perturbations in InR-Tor signaling under nutrient stress. This data demonstrates that disrupting InR-Tor signaling is sufficient to reduce epidermal cell growth in both nutrient conditions.

Because InR-Tor signaling is necessary for epidermal cell growth, we wondered if the knockdown of these genes in the entire larval epidermis using *Gal4^{R38F11}* would delay animal growth in 8% yeast. This delay in animal growth might then mimic the preferential growth of C4da neurons under nutrient restriction. Indeed, compared to the control, knockdown of *InR* (Figure 4.2Q) and overexpression of *InR-DN* (Figure 4.S2O) in all epidermal cells caused an increase in C4da dendrite growth (Figure 4.2S). This increase in C4da dendrite growth was also observed in *Tor RNAi* (Figure 4.2R) and *UAS-dTor^{TEED}* (Figure 4.S2P) overexpression using the same *Gal4^{R38F11}* (Figure 4.2S). This data indicates that a slight delay in epidermal cell growth is sufficient to induce preferential growth of C4da dendrites.

Figure 4.2. Preferential neuronal growth relies on InR-Tor signaling.

(A-F) DdaC dendritic fields in the *Gal4^{ppk}* control on 8% and 1% yeast (A and D) and animals expressing *Gal4^{ppk}*-driven *InR RNAi* (B and E) and *Tor RNAi* (C and F) on 8% and 1% yeast. (G and H) Quantification of total dendrite density (G) and dendrite density ratio (H) in the genotypes indicated. *** $p \leq 0.001$; Student's t-test. (I-N) Expression of Nrg-GFP in the *Gal4^{R16D01}* control animals on 8% and 1% yeast (I and L) and animals expressing *Gal4^{R16D01}*-driven *InR RNAi* (J and M) and *Tor RNAi* (K and N) on 8% and 1% yeast. RNAi-expressing cells are labeled in magenta and all epidermal cells are labeled in green. (O) Quantification of average epidermal cell size in the RNAi-expressing region divided by average epidermal cell size in the WT region (RNAi/WT ratio) in the genotypes indicated. (P-R) DdaC dendritic fields in the *Gal4^{R38F11}* control (P) and animals expressing *Gal4^{R38F11}*-driven *InR RNAi* (Q) and *Tor RNAi* (R) on 8% yeast. (S) Quantification of total dendrite density in the genotypes indicated. *** $p \leq 0.001$; Student's t-test. For all quantifications, each circle represents a neuron. Black bar: mean; red bars: SD. Scale bars represent 50 μm for A-F and P-R. Scale bars represent 100 μm for I-N. Nrg-GFP was detected using a GFP trap line. Imaging in A-F was performed by Yineng Xu and Amy Poe. Quantifications in G and H were performed by Christine Zhang, Yuna Lee, and Amy Poe. Imaging in I-N and P-R was performed by Amy Poe. Quantifications in O were performed by Yineng Xu. Quantifications in S were performed by Yuna Lee.

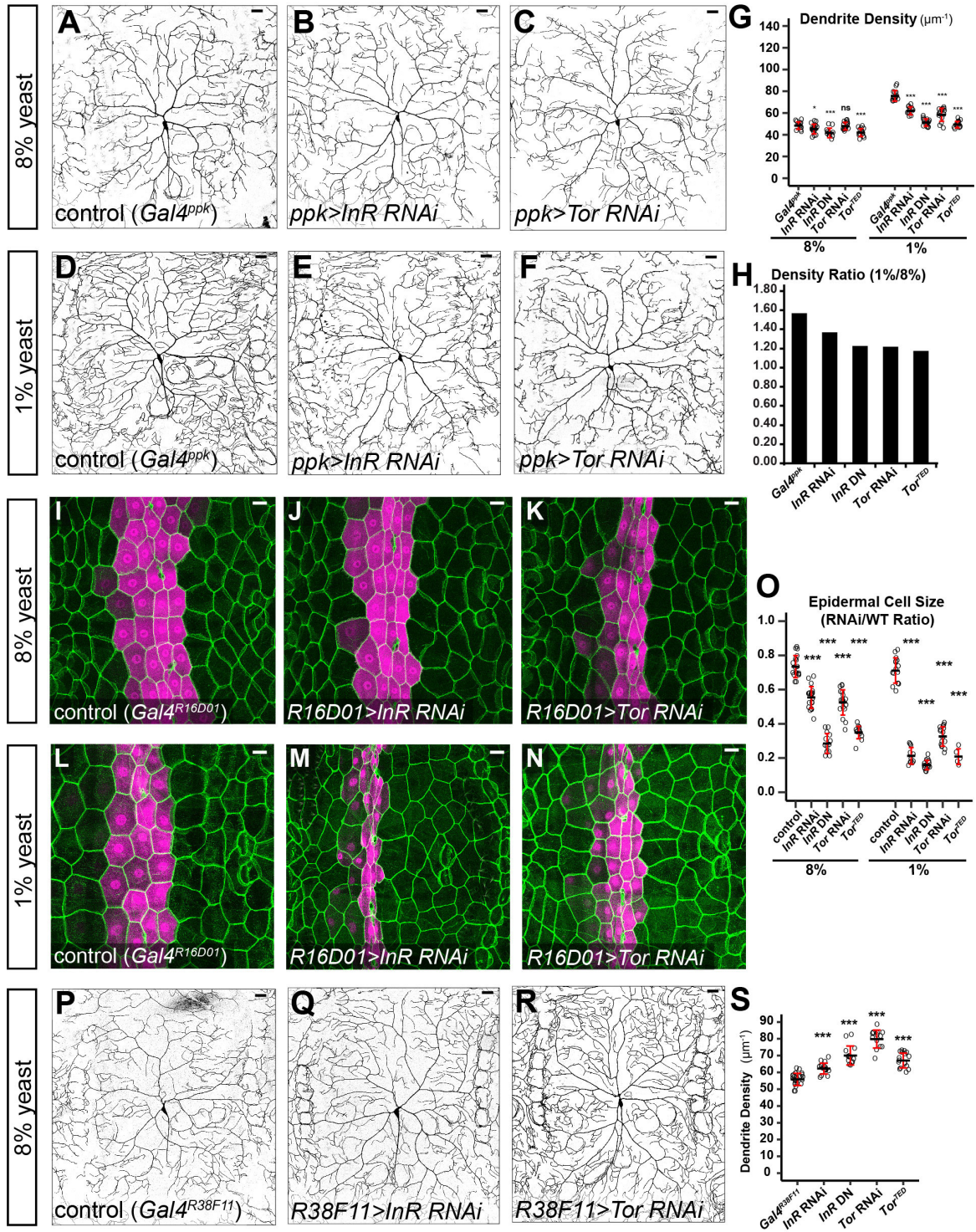
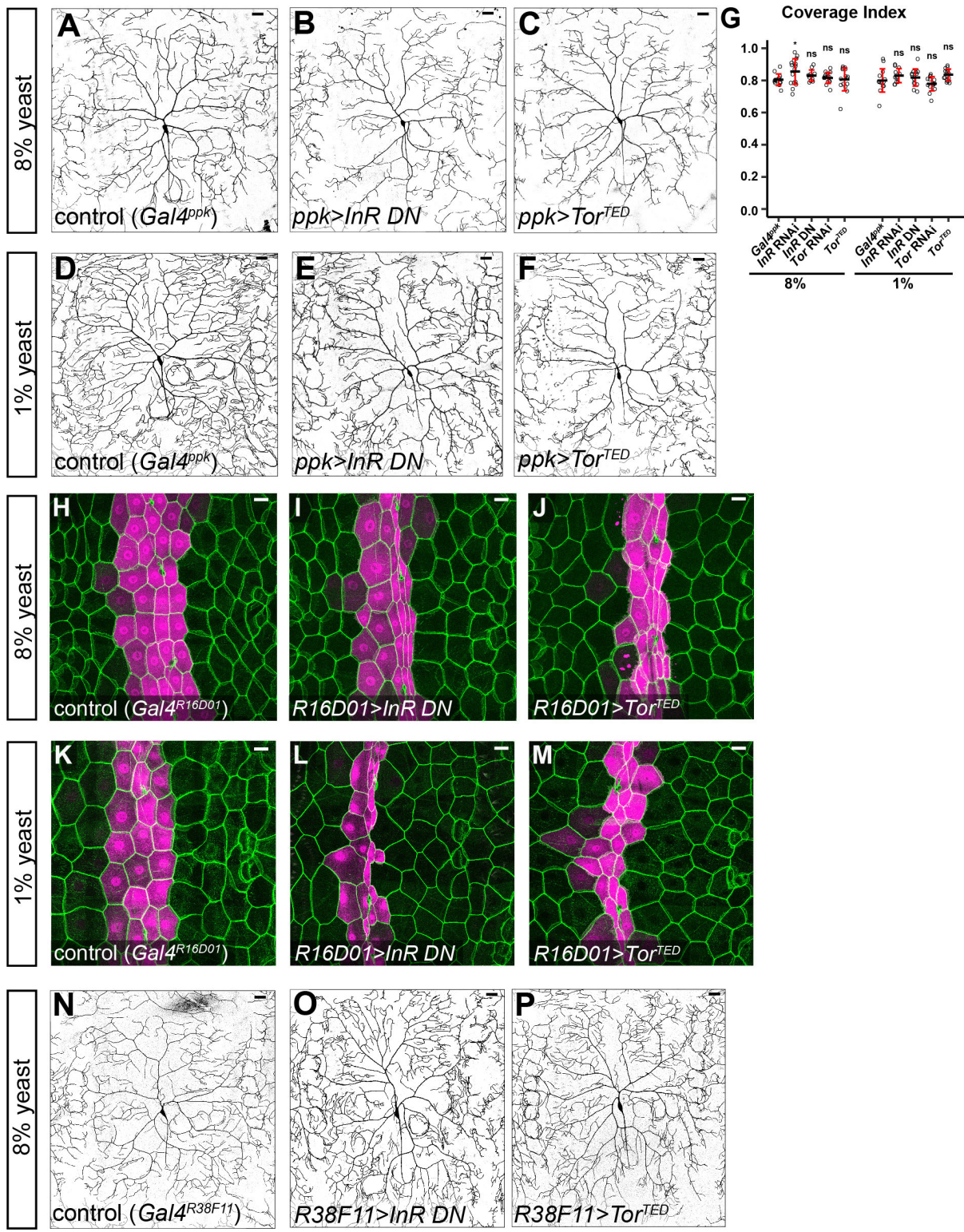


Figure 4.S2. InR-Tor signaling is necessary for neuronal cell growth.

(A-F) DdaC dendritic fields in the *Gal4^{ppk}* control on 8% and 1% yeast (A and D) and animals expressing *Gal4^{ppk}*-driven *InR-DN* (B and E) and *UAS-dTor^{TE}* (C and F) on 8% and 1% yeast. (G) Quantification of coverage index in the genotypes indicated. * <0.05 ; ns, not significant; Student's t-test. Each circle represents a neuron. Black bar: mean; red bars: SD. (H-M) Expression of Nrg-GFP in the *Gal4^{R16D01}* control animals on 8% and 1% yeast (I and L) and animals expressing *Gal4^{R16D01}*-driven *InR-DN* (I and L) and *UAS-dTor^{TE}* (J and M) on 8% and 1% yeast. RNAi-expressing cells are labeled in magenta and all epidermal cells are labeled in green. (N-P) DdaC dendritic fields in the *Gal4^{R38F11}* control (N) and animals expressing *Gal4^{R38F11}*-driven *InR-DN* (O) and *UAS-dTor^{TE}* (P) on 8% yeast. Scale bars represent 50 μm for A-F and N-P. Scale bars represent 100 μm for H-M. Nrg-GFP was detected using a GFP trap line. Imaging in A-F was performed by Yineng Xu and Amy Poe. Quantifications in G were performed by by Christine Zhang, Yuna Lee, and Amy Poe. Imaging in H-P was performed by Amy Poe.



Neurons exhibit suppression of autophagy under nutrient restriction

In starvation conditions, low nutrient levels inhibit cell growth through activation of autophagy (7, 12). We next wondered if C4da neurons and epidermal cells exhibit differences in autophagic activity in the 1% and 8% yeast conditions. To monitor the endogenous levels of autophagic structures, we used a previously described 3xmCherry-tagged Atg8a reporter driven by its endogenous promoter (25). This reporter labels all autophagic structures including phagophores, autophagosomes and autolysosomes (26). Compared to the 8% yeast condition, epidermal cells in the 1% yeast condition showed a dramatic increase in the number of autophagic structures indicating that autophagy is induced in these cells under nutrient restriction (Figures 4.3A-C). However, the number of autophagic structures in C4da neurons was not affected by nutrient restriction (Figures 4.3A-C) which suggests that autophagy is suppressed in these cells.

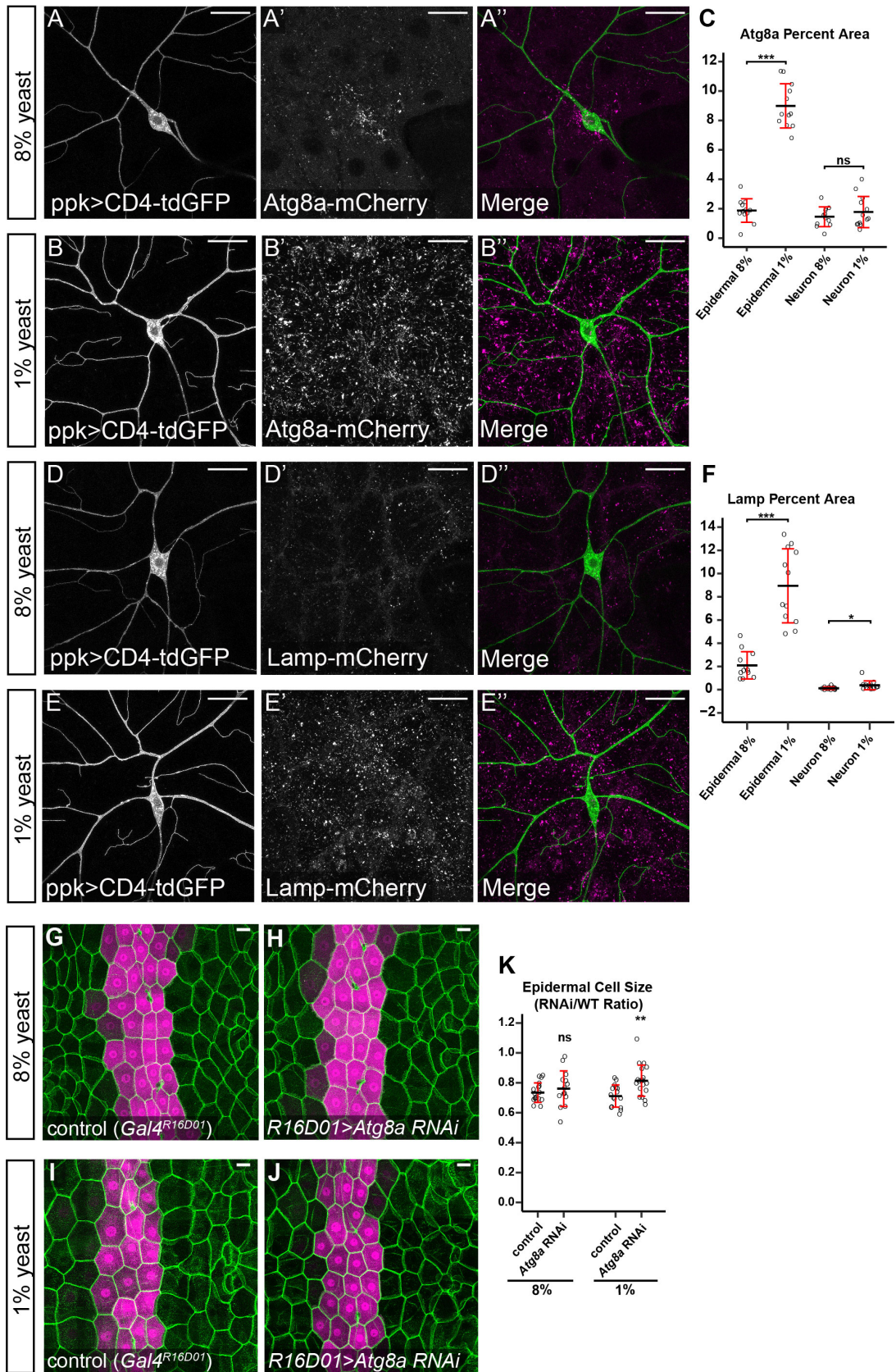
In order to compare autolysosome formation in both nutrient conditions, we next examined the levels of lysosomes using a previously described endogenous Lamp-promoter driven dLamp-3xmCherry reporter (25). The dLamp-3xmCherry reporter labels lysosomes independently from their acidification state (26). Consistent with the 3xmCherry-Atg8a data (Figures 4.3A-C), the number of dLamp-3xmCherry vesicles was dramatically increased in epidermal cells under nutrient restriction (Figures 4.3D-F) indicating an induction in autophagy. Additionally, the number of dLamp-3xmCherry vesicles in C4da neurons was not affected by nutrient restriction (Figures 4.3D-F). Together, this data indicates that C4da neurons suppress autophagy in low nutrient conditions.

Because epidermal cells and C4da neurons exhibit different levels of autophagy under nutrient restriction, we next wanted to know if autophagy activation is responsible for the

differential growth response of these cells. If autophagy activation is necessary to inhibit epidermal cell growth in low nutrient conditions, then we predict that blocking autophagy will cause an increase in epidermal cell size in the 1% yeast condition. To block autophagy, we disrupted the activity of a ubiquitin-like protein, *Autophagy-related 8a (Atg8a)*, which is necessary for autophagosome formation (27). We knocked down *Atg8a* (Figures 4.3H, J) in a stripe of epidermal cells in the middle of the segment using *Gal4^{R16D01}*. We then examined the cell size of the RNAi-expressing cells and wildtype epidermal cells in the same segment using the septate junction marker Nrg-GFP. Compared to the control (Figures 4.3G, I), *R16D01>Atg8a* RNAi caused an increase in epidermal cell size in the low yeast condition (Figure 4.3K). This data suggests that autophagy is necessary for suppressing epidermal cell growth under nutrient stress.

Figure 4.3. Neurons exhibit suppression of autophagy under nutrient deprivation.

(A-B'') Expression of 3xmCherry-tagged Atg8a reporter in animals expressing *Gal4^{ppk}>CD4tdGFP* on 8% (A-A'') and 1% yeast (B-B''). Right panels show *Gal4^{ppk}>CD4tdGFP* in green and 3xmCherry-Atg8a in magenta. (C) Quantification of percent area with 3xmCherry-Atg8a expression in epidermal cells and neurons in both yeast conditions. (D-E'') Expression of 3xmCherry-tagged dLamp reporter in animals expressing *Gal4^{ppk}>CD4tdGFP* on 8% (D-D'') and 1% yeast (E-E''). (F) Quantification of percent area with 3xmCherry-dLamp expression in epidermal cells and neurons in both yeast conditions. ns, not significant; * <0.05 ; *** $p\leq 0.001$; Student's t-test. (G-J) Expression of Nrg-GFP in the *Gal4^{R16D01}* control animals on 8% and 1% yeast (G and H) and animals expressing *Gal4^{R16D01}*-driven *Atg8a RNAi* (H and J) on 8% and 1% yeast. RNAi-expressing cells are labeled in magenta and all epidermal cells are labeled in green. (K) Quantification of the RNAi cell size/WT cell size ratio in the genotypes indicated. For all quantifications, each circle represents an individual neuron. The black bars represent the mean and the red bars represent the standard deviation. Scale bars represent 100 μm . Nrg-GFP was detected using a GFP trap line. Imaging in A-E'' was performed by Yineng Xu. Quantifications in C and F were performed by Amy Poe. Imaging in G-J was performed by Amy Poe. Quantifications in K were performed by Yineng Xu.



Differential responses of other classes of da neurons under nutrient restriction

The *Drosophila* peripheral nervous system (PNS) has four classes of da sensory neurons with overlapping dendritic fields (18). We next wondered if the class I or class III da neurons exhibit growth advantage under nutrient restriction. We examined the dendritic patterns of dorsal class I *ddaE* (Figures 4.4A-C) and dorsal class III *ddaA* and *ddaF* (Figures 4.4D-H) in both the 1% and 8% yeast conditions. As previously reported (22), nutrient restriction did not affect the branching patterns of the *ddaE* dendrites (Figure 4.4C). However, nutrient restriction caused a dramatic increase in total dendrite length (Figure 4.4F), terminal dendrite length (Figure 4.4G), and terminal dendrite number (Figure 4.4H) in the *ddaA* and *ddaF* neurons. Combined with the C4da neuron data (Figure 4.1), these data indicate that da neurons exhibit differential growth responses to nutrient deprivation.

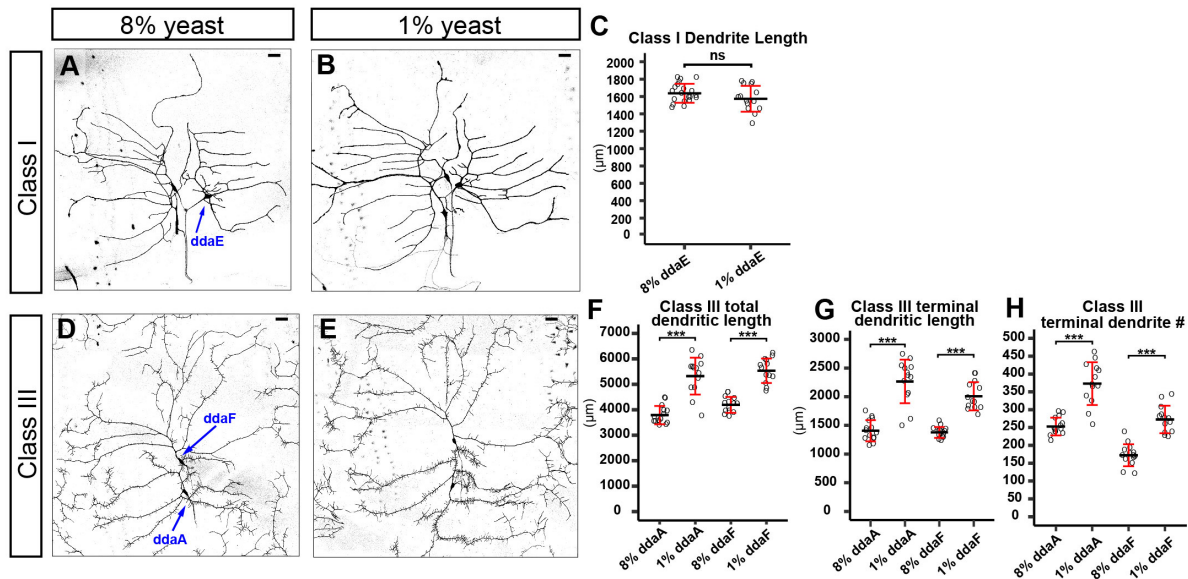


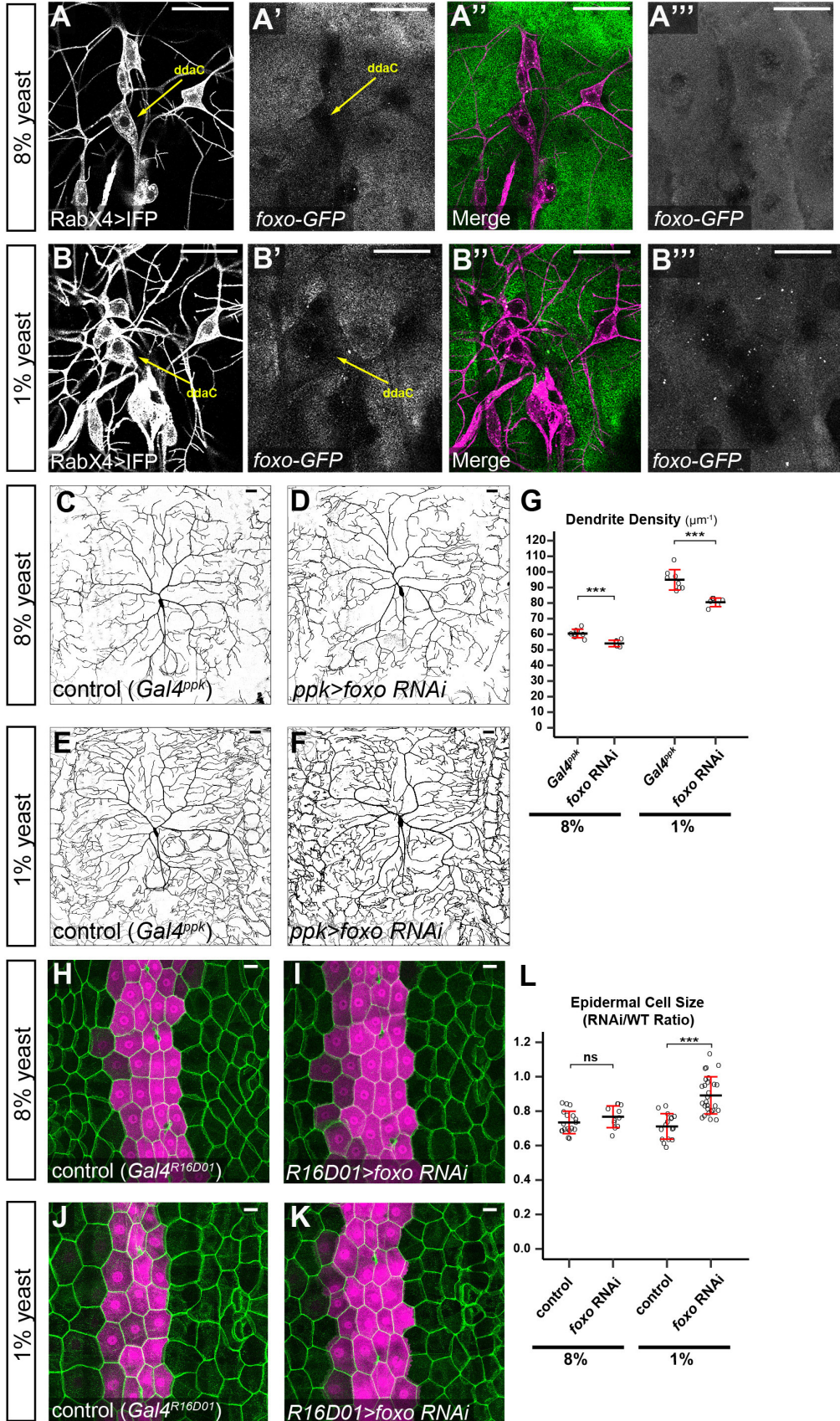
Figure 4.4. Differential responses of other classes of da neurons under nutrient deprivation.

(A and B) Dendritic fields of class I *ddaE* neurons in animals grown on 8% yeast (A) and 1% yeast (B). (C) Quantification of total dendrite length in animals on 8% and 1% yeast. ns, not significant; Student's t-test. (D and E) Dendritic fields of class III *ddaA* and *ddaF* neurons in animals grown on 8% yeast (D) and 1% yeast (E). (F-H) Quantification of total dendrite length (F), terminal dendritic length (G), and terminal dendrite numbers (H) in animals on 8% and 1% yeast. *** $p \leq 0.001$; Student's t-test. For all quantifications, each circle represents an individual neuron. The black bars represent the mean and the red bars represent the standard deviation. Scale bars represent 50 μm . Imaging and quantifications were performed by Amy Poe.

FoxO activity underlies differential growth of neurons and epidermal cells

During nutrient deprivation, autophagy-related genes (*Atg*) are activated by many transcription factors including *forkhead box, sub-group O* (*FoxO*). Activation of *Atg* genes then leads to an increase in autophagosome formation (14). Because we observed an increase in autophagy in epidermal cells under nutrient stress, we next wanted to know if differences in FoxO activity are responsible for the differential growth response of these cells. We first examined *foxo* expression in C4da neurons and epidermal cells on 1% and 8% yeast using a genomic *foxo-GFP* reporter. We used *Gal4^{RabX4}*-driven *IFP* to label all classes of da neurons. By examining the maximum projected images, we found that *foxo* is expressed in the cytoplasm of epidermal cells on both the 8% (Figure 4.5A''') and 1% (Figure 4.5B''') yeast conditions. This data suggests that *foxo* is active in epidermal cells in both nutrient conditions. Surprisingly, when we examined individual z-stacks, we did not detect obvious *foxo* expression in C4da neurons on either the 8% (Figures 4.5A-A'') or 1% (Figures 4.5B-B'') yeast conditions. Together, these data demonstrate that neurons and epidermal cells exhibit different expression patterns of FoxO which suggests that FoxO is only active in epidermal cells.

Figure 4.5. FoxO activity underlies differential growth of neurons and epidermal cells. (A-B''') Expression of *foxo-GFP* in animals expressing *Gal4^{RabX4}*-driven *IFP* on 8% (A-A''') and 1% (B-B''') yeast. The first three panels show an individual z-stack for the da neurons labeled with *IFP* (left panel), *foxo-GFP* expression (middle panel), and the merge showing *foxo-GFP* (green) and da neurons (magenta) (right panel). Panels on the far right show the processed maximum projected image of only the *foxo-GFP* expression channel. Yellow arrows in A-A' and B-B' indicate the location of the class IV ddaC neuron. (C-F) DdaC dendritic fields in the *Gal4^{ppk}* control on 8% and 1% yeast (C and E) and animals expressing *Gal4^{ppk}*-driven *foxo RNAi* (D and F) on 8% and 1% yeast. (G) Quantification of total dendrite density in the genotypes indicated. (H-K) Expression of *Nrg-GFP* in the *Gal4^{R16D01}* control animals on 8% and 1% yeast (H and J) and animals expressing *Gal4^{R16D01}*-driven *foxo RNAi* (I and K). RNAi-expressing cells are labeled in magenta and all epidermal cells are labeled in green. (L) Quantification of the RNAi cell size/WT cell size ratio in the genotypes indicated. ns, not significant; *** $p \leq 0.001$; Student's t-test. For all quantifications, each circle represents an individual neuron. The black bars represent the mean and the red bars represent the standard deviation. Scale bars represent 50 μm in C-F and 100 μm in A-B''' and H-K. *Nrg-GFP* was detected using a GFP trap line. Imaging in A-B''' was performed by Yineng Xu. Imaging in C-F and H-K was performed by Amy Poe. Quantifications in G were performed by Kush Dubey. Quantifications in L were performed by Yineng Xu.



Based on the expression analysis, a plausible model to explain the differential growth response of these cells under nutrient stress is that, in epidermal cells, FoxO activates autophagy leading to inhibition of cell growth. However, C4da neurons exhibit low levels of FoxO activity resulting in suppression of autophagy and thereby promoting neuronal cell growth. Based on this model, we predict that the LOF of FoxO will not affect C4da dendrite growth in either yeast condition, but will promote epidermal cell growth in the low yeast condition. To test this prediction, we first knocked down *foxo* (Figures 4.5D, F) by RNAi using a C4da-neuron specific driver *Gal4^{ppk}*. Surprisingly, compared to the control (Figures 4.5C, E), *foxo* KD in C4da neurons caused a reduction in dendrite growth in both the 8% and 1% yeast conditions (Figure 4.5G). Together with the *foxo-GFP* expression data (Figures 4.5A-B'''), this suggests that very low levels of *foxo* are necessary in C4da neurons to slightly promote dendrite growth. To confirm knockdown efficiency, we tested the efficiency of RNAi in knocking down overexpressed *foxo-GFP* in a stripe of epidermal cells using *Gal4^{R16D01}*. Foxo-GFP was strongly expressed in *R16D01>foxo-GFP* control animals (Figure 4.S3A), but was absent in animals also coexpressing *foxo RNAi* (Figures 4.S3B, C). These data demonstrate that the *foxo* knockdown is effective. Together, these data suggest that low levels of FoxO in C4da neurons are necessary to promote dendrite growth.

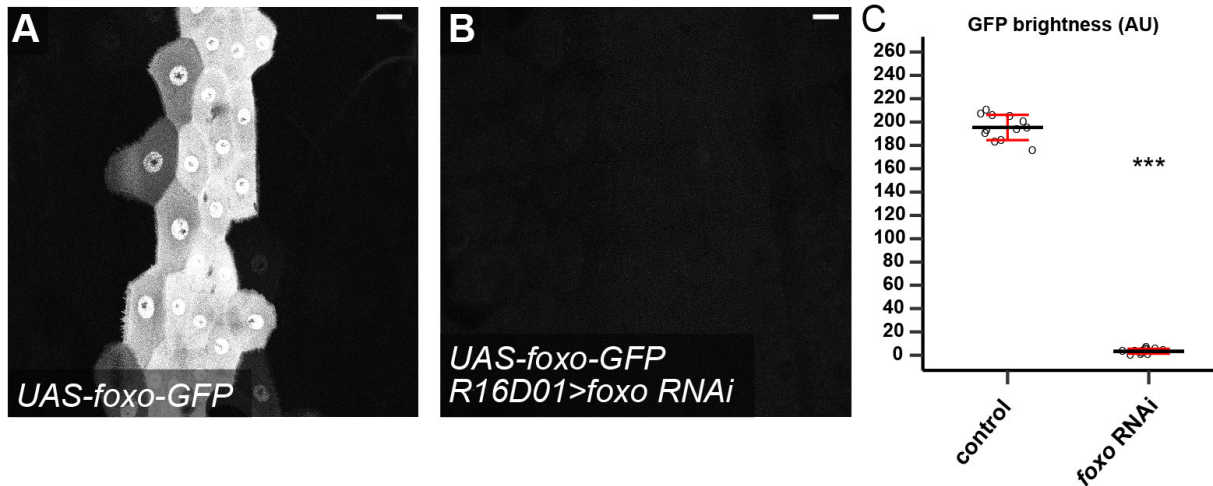


Figure 4.S3. Effectiveness of foxo RNAi.

(A and B) An animal expressing *Gal4^{R16D01}UAS-foxo-GFP* (A) and an animal expressing *Gal4^{R16D01}UAS-foxo-GFP UAS-foxo RNAi* (B). (C) Quantification of GFP brightness in the *Gal4^{R16D01}*-expressing region in the genotypes indicated. *** $p \leq 0.001$; Student's t-test. Each circle represents an individual segment. The black bars represent the mean and the red bars represent the standard deviation. Scale bars represent 100 μm . Reagents were contributed by Amy Poe. Imaging was performed by Yineng Xu. Quantifications were performed by Christine Zhang.

To next determine if FoxO is necessary for the suppression of epidermal cell growth under nutrient restriction, we knocked down *foxo* (Figures 4.5I, K) in a stripe of epidermal cells in the middle of the segment using *Gal4^{R16D01}*. We then examined the cell size of the RNAi-expressing cells and wildtype epidermal cells in the same segment using the septate junction marker *Nrg-GFP*. Compared to the control (Figures 4.5H, J), *R16D01>foxo RNAi* caused a dramatic increase in epidermal cell size on 1% yeast (Figure 4.5L). This data indicates that FoxO activity is necessary for restricting epidermal cell growth in low yeast conditions. Together with the C4da neuron data (Figures 4.5C-G), this suggests that FoxO activity has differential effects on epidermal cell and neuronal growth. Therefore, FoxO activity is likely responsible for the differential growth response of these cells under nutrient restriction.

DISCUSSION

The *Drosophila* peripheral sensory dendrites exhibit two phases of growth during larval development: a rapid expansion of the dendritic arbor to establish the receptive field early in larval development and then synchronous growth with the body wall epithelium in a process called scaling (1). Dendritic scaling ensures that as the animal grows the sensory neuron maintains proper coverage of the receptive field. Although much has been recently learned about the coordination between epidermal cell and C4da neuron growth (1, 21), the role of the organism's nutritional environment in dendritic scaling remains poorly understood. In particular, it is unknown how nutrient restriction affects neuron-epidermal cell growth coordination. Here we demonstrate that in nutrient poor conditions two classes of *Drosophila* da neurons grow preferentially compared to larval epidermal cell growth. Our analysis of C4da dendrite growth and epidermal cell growth indicates that the apparent overgrowth of dendrites under nutrient restriction is due to the greater impact of nutrient levels on larval body wall growth than on neuronal growth. We also determined that epidermal cells and C4da neurons exhibit different levels of autophagosome formation under nutrient stress with C4da neurons preferentially suppressing autophagy. Additional evidence indicates that the transcription factor, FoxO, is likely responsible for the dis-coordination of C4da dendrite and epidermal cell growth. Our study, therefore, reveals a potential molecular mechanism responsible for the dis-coordination of growth between dendrites and their epithelial substrate.

Mechanism for Preferential Neuronal Growth under Nutrient Deprivation

Our results demonstrate that, in response to low nutrients, C4da neurons grow excessively relative to epidermal cell growth in the later dendritic scaling phase of larval development. Our analysis of autophagy induction using *Atg8a-mCherry* and *Lamp-mCherry*

expression levels reveals that an excess of autophagy in epidermal cells likely inhibits cell growth in low yeast conditions. Indeed, knockdown of a gene necessary for autophagosome formation, *Atg8a*, in epidermal cells caused an increase in epidermal cell growth in the low yeast environment (Figure 4.3). However, autophagy levels are unchanged in C4da neurons in the low nutrient condition which likely permits excess dendrite growth. Interestingly, the transcription factor, FoxO, exhibits distinct cell-specific expression patterns with high expression in epidermal cells and low or no detectable expression in C4da neurons when larvae are grown on 1% yeast. Using LOF analysis, we found that FoxO activity slightly enhances C4da dendrite growth but inhibits epidermal cell growth in low nutrient conditions. Our results strongly suggest that FoxO plays differential roles in regulating cell growth in different cell types. Given FoxO's role in activating transcription of autophagy genes in other tissues including skeletal muscle, mouse primary cerebellar granule neurons, and human cancer cell lines (14), a likely interpretation is that FoxO induces transcription of autophagy genes in epidermal cells thereby inhibiting cell growth. However, additional experiments are necessary in order to further elucidate these interactions and to determine the mechanisms regulating FoxO expression. In the future, it would be important to first examine the effect of FoxO LOF on autophagy levels in both epidermal cells and neurons in low nutrient conditions. It would also be interesting to determine if activating or increasing autophagy levels in C4da neurons restricts the preferential dendrite growth phenotype.

FoxOs in Nervous System Development

FoxO plays a key role in regulating many neuronal processes including neural stem cell homeostasis, neuronal polarity, and neurite development (28-33). Our LOF analysis supports the previous finding (31) that FoxO promotes C4da dendrite branching through regulation of microtubule dynamics. Although we did not detect FoxO expression in C4da neurons using *foxo-*

GFP, our genetic data suggests that FoxO is indeed expressed in neurons, but probably at a very low level. Several additional studies demonstrate that FoxO acts as a conserved regulator of neurite outgrowth. In *C. elegans*, the *foxO* homolog, *daf-16*, promotes axon outgrowth of the AIY interneuron (33). In addition, *Drosophila* FoxO regulates synaptic microtubule stability at the neuromuscular junction (34). Mammalian FoxO6 is required for dendritic spine density formation and memory consolidation in hippocampal neurons (32). Furthermore, knockdown of FoxO activity in primary cerebellar granule neurons dramatically reduced axon length (33). It will be interesting to find out whether these FoxO-expressing neurons preferentially grow dendrites in nutrient poor conditions.

Organ Sparing under Nutrient Deprivation

Organisms developing in nutrient deprived conditions face many challenges in order to reach the necessary overall body and tissue size. When nutrients are scarce, the animal's physiology must adapt. As such, the growth of certain essential tissues is spared at the expense of overall animal growth. For example, the growth of neural stem cells (neuroblasts) in the *Drosophila* brain is protected from nutrient restriction through the activity of the receptor tyrosine kinase, anaplastic lymphoma kinase (Alk) and its glial-derived ligand, Jelly belly (Jeb). In low nutrient conditions, Alk signaling acts as an alternative pathway to InR signaling to activate PI3-kinase and RagA/Rheb/TORC1 (5). However, our preliminary data indicate that Alk is not necessary for the preferential growth of C4da dendrites under nutrient stress (data not shown). This suggests that Alk signaling plays different roles in regulating neuronal development in dividing and nondividing cells. Currently, it is not known what effect nutrient deprivation has on neurite development in terminally differentiated neurons in the *Drosophila* CNS. Do neurites in these cells show a similar preferential growth response to a low nutrient

environment? If so, does this occur through differences in FoxO activity? While FoxO expression has been observed in the *Drosophila* larval ventral nerve cord (34), the expression pattern of FoxO in the entire CNS has not been well characterized. Therefore, it would be interesting to examine FoxO expression in the developing CNS in both low yeast and high yeast conditions. This analysis would provide insight into the conserved molecular mechanisms regulating dendrite growth under nutrient stress.

Autophagy in Neural Development and Neurodegenerative Diseases

As nondividing cells, neurons must regulate the accumulation of potentially toxic cytoplasmic components and proteins. Therefore, autophagy-dependent degradation of cytoplasmic components is essential for neuronal cell survival and maintenance (35). Additionally, neurons in the CNS have been shown to exhibit low levels of autophagosomes even under nutrient rich conditions. These low levels of autophagosomes are due to active basal autophagy levels (35). Recent evidence indicates that autophagy regulates neurite formation and growth (15, 36). Inhibiting autophagy in primary cortical neurons led to elongation of the axon while activation of autophagy in these neurons suppressed axon growth (15). Additionally, alterations in autophagic flux in adult-born hippocampal neurons disrupt dendrite and spine development (36).

Many neurodegenerative diseases such as Alzheimer's disease, Parkinson's disease, and Huntington's disease are associated with disruptions in autophagic flux leading to the accumulation of intracellular protein aggregates in neurons (37). Indeed, suppression of autophagy in the mouse central nervous system led to neurodegeneration and overall deficits in motor functioning (38). Similarly, in the *Drosophila* brain, the accumulation of autophagosomes

in neurons due to the blockage of autophagosome-lysosome fusion resulted in neuronal dysfunction and locomotion defects (16).

In the future, it will be important to determine the functional relevance of preferential dendrite growth in the C3da and C4da neurons under nutrient restriction. The C3da neurons mediate behavioral responses to gentle touch sensation (39) and noxious cold temperatures (40). The C4da neurons are nociceptive neurons responding to noxious heat and harsh mechanical stimuli with a characteristic corkscrew-like rolling behavioral response (41). Previous studies have shown that reductions in class IV dendrite complexity correlate with impaired nociceptive responses (31, 42, 43). Therefore, an interesting hypothesis is that excessive C4da dendrite growth results in larvae that are hypersensitive to noxious stimuli. Future studies will examine the behavioral responses of larvae developing in low nutrient conditions. This will provide a more complete understanding of the functional necessity of growing more sensory dendrites under nutrient deprivation.

METHODS

Live imaging

Snapshot live imaging of larval da neurons was performed as described previously (17). Briefly, animals were raised at 25°C in density-controlled vials containing between 50-70 embryos collected in a 3 hour time window. To achieve optimum embryo densities, approximately 50 virgin females were aged 5 days on molasses food with yeast paste, crossed with approximately 15-20 males, and then allowed to mate for 1-2 days on molasses food with yeast paste. Embryo collections were then performed in a 3 hour time window on both 1% and 8% yeast food. For Figures 4.2, 4.S2, 4.3, 4.4, and 4.5, third instar larvae at 86 hrs AEL on 8% yeast or 216 hrs AEL on 1% yeast were mounted in glycerol and imaged with a Leica SP8 confocal. The A2-A3

segments of 8-10 larvae were imaged for each genotype using a 20X oil objective. To image larvae younger than 72 hr AEL, larvae were anesthetized by isoflurane for 2 minutes & then mounted in halocarbon oil.

Fly Food Recipe

Fly food was prepared using the following recipes. The exact yeast percentage for each batch of food was calculated based on total final volume. Animal growth on different yeast concentrations was initially analyzed by Kailyn Li. Larvae grown on yeast concentrations below 1% do not develop.

Ingredients for 20 vials:

Ingredients:	1% yeast	8% yeast
Distilled H ₂ O	240mL	234mL
Agar	2.4g (12g/L)	2g (10g/L)
Glucose	20g	20g
Inactive yeast	2.5g	20g
Acid mix (phosphoric acid + propionic acid)	2mL	2mL
Target final solution volume	250mL	250mL

*This recipe allows for the dispersal of ~12mL into 20 vials.

Acid Mix: (for 100ml)

Solution A (500 ml): 41.5 ml Phosphoric Acid + 458.5 ml distilled water

Solution B (500 ml): 418 ml Propionic Acid + 82 ml distilled water

Mix Solution A and Solution B together to make Acid Mix

Fly Stocks

Nrg-GFP (#6844), *R16D01-Gal4* (#48722), *R38F11-Gal4* (#50014), *RabX4-Gal4* (#51602),

UAS-InR-RNAi (#51518), *UAS-InR-DN* (#8253), *UAS-Tor-RNAi* (#34639), *UAS-Tor.TED*

(#7013), *UAS-foxo-RNAi* (#32427), *UAS-foxo-GFP* (#44214), *PBac{foxo-GFP.FLAG}* (#38644),

UAS-Atg8a-RNAi (#58309) were obtained from Bloomington Stock Center (BDSC).

pAtg8apromoter-3xmCherry-Atg8a and pdLamppromoter-dLamp-3xmCherry were a gift from Gábor Juhász.

We used the following neuronal markers to label specific classes of da neurons: *ppk-CD4-tdGFP* (44), *ppk-Gal4* (19), *UAS-CD4-tdGFP* and *UAS-CD4-tdTom* (44) for C4da; *R10D05-CD4-tdTom* (45) for C1da; *NompC-LexA::p65 LexAop-CD4-tdTom* (45) for C3da. *RabX4-Gal4 UAS-mIFP-2A-HOI* (this study) was used to label all classes of da neurons.

RNAi

RNAi knockdown of *InR*, *Tor*, *foxo* in neurons was carried out with *ppk-Gal4 UAS-CD4-tdTom*. RNAi knockdown of *InR* and *Tor* in all epidermal cells was carried out with *ppk-CD4-tdGFP*; *R38F11-Gal4*. RNAi knockdown of *InR*, *Tor*, *Atg8a*, and *foxo* in stripes of epidermal cells was carried out with *Nrg-GFP*; *R16D01-Gal4 UAS-mIFP-2A-HOI*. *UAS-mIFP-2A-HOI* was used to label RNAi-expressing epidermal cells. *ppk-Gal4 UAS-CD4-tdTom* and *ppk-CD4-tdGFP* were used to label C4da neurons. The effectiveness of *foxo* RNAi was determined by crossing *UAS-foxo-GFP*; *UAS-foxo-RNAi* flies with *Gal4^{R16D01} UAS-mIFP-2A-HOI* flies. Imaging of autophagy was performed by crossing *Atg8a-mCherry* and *Lamp-mCherry* with *ppk-Gal4 UAS-CD4-tdGFP* to label C4da neurons. For C1da and C2da neurons, we used *R10D05-CD4-tdTom* and *R20C11-CD4-tdGFP* to label C1da and C2da neurons, respectively. For C3da neurons, we used *NompC-LexA::p65 LexAOP-CD4-tdTom* to label C3da neurons. Foxo expression was determined by crossing *foxo-GFP* with *foxo-GFP*; *RabX4-Gal4 UAS-mIFP-2A-HOI* to label all classes of da neurons.

Image analysis and quantification

Tracing and measuring of C1da, C3da, and C4da dendrites was performed as described previously (45). Briefly, for tracing and measuring C1da, C3da, and C4da dendrites in

Fiji/ImageJ, images of dendrites (1,024 X 1,024 pixels) taken with a 20X objective were first processed by Gaussian Blur (Sigma: 0.8) and then Auto Local Threshold (Phansalkar method, radius: 50). Isolated particles below the size of 120 pixels were removed by the Particles4 plugin (<http://www.mecourse.com/landinig/software/software.html>). The dendrites were then converted to single-pixel-width skeletons using the Skeletonize (2D/3D) plugin and processed using the Analyze Skeleton (2D/3D) plugin. The length of skeletons was calculated based on pixel distance; terminal dendrites in the dendritic field or regions of interest were counted based on the endings of terminal dendrites. Skeletons of terminal dendrites in regions of interest were isolated using the Strahler Analysis plugin (http://imagej.net/Strahler_Analysis). Dendrite density was calculated using the formula: $1000 \times \text{dendritic length } (\mu\text{m}) / \text{dendritic area } (\mu\text{m}^2)$; normalized terminal dendrite number was calculated using the formula: $1000 \times \text{terminal dendrite number} / \text{dendritic area } (\mu\text{m}^2)$. Dendrite density ratio was calculated using the formula: average dendrite density on 1% / average dendrite density on 8%. Coverage index was calculated using the formula: $\text{dendritic area } (\mu\text{m}^2) / \text{receptive field area } (\mu\text{m}^2)$.

Epidermal cell quantification

Epidermal cell size in Figures 4.1, 4.2, 4.3, and 4.5 was determined using custom-built scripts written by Chun Han in Fiji/ImageJ. Images of epidermal cells (1,024 X 1,024 pixels) taken with a 20X objective were first processed by Gaussian Blur (Sigma: 1) and then Auto Local Threshold (Phansalkar method, radius: 30). Isolated particles below the size of 500 pixels were removed by the Particles4 plugin (<http://www.mecourse.com/landinig/software/software.html>). The Nrg-GFP signal was then converted to single-pixel-width skeletons of epidermal cell borders using the Skeletonize (2D/3D) plugin and processed using the Options plugin. Images were then visually inspected to ensure that all epidermal cell borders were accurately labeled. Any

erroneous epidermal cell borders were broken using the brush tool with black as the drawing color. Another custom-built script was then run to clean up these images by converting the images to a mask, removing the broken lines with the Options plugin, and re-running the Skeletonize (2D/3D) plugin. For Figures 4.2, 4.3, and 4.5, the regions of interest (ROIs) in the RNAi-expressing and control regions were manually drawn. A third custom-built script was then run to convert the epidermal cell border to particles and measure the area, perimeter, Feret, and minFeret for each epidermal cell. For Figures 4.2, 4.3, and 4.5, we divided the average cell size in the RNAi-expressing region by the average cell size in the WT region to determine the RNAi/WT cell size ratio.

Autophagy quantification

Lamp-mCherry and Atg8a-mCherry levels were determined using custom-built scripts written by Chun Han in Fiji/ImageJ. Z-stack images of dendrites and Lamp-mCherry or Atg8a-mCherry (1,024 X 1,024 pixels) taken with a 40X objective were first processed using a local threshold of 20 for dendrites, 60 for Lamp images and 80 for Atg8a images. Then single pixel hotspots were removed from the dendrite channel to remove background signal and the dendrites were converted into a black/white image using the Convert to Mask plugin (method=Moments background=Dark black). The autophagy (Lamp or Atg8a) signal was then converted into a black/white image using the Convert to Mask plugin (method=MaxEntropy background=Dark black). The masks for each channel were then used to assemble a composite maximum projection image. Using the maximum projected image, a ROI in neuronal cell body and a ROI outside the neuron were drawn manually and the mean gray value of the area was calculated for either the Lamp or Atg8a signal.

Foxo RNAi validation quantification

The GFP fluorescence intensity of RNAi-expressing cells was measured in Fiji/ImageJ. The RNAi-expressing cells labeled with *UAS-mIFP-2A-HOI* were selected using the magic wand tool and a ROI was defined for those cells. Then the mean gray value of the *UAS-foxo-GFP* channel was calculated. Background GFP fluorescence in a nearby WT region was measured for each image. The normalized gray value for each image was then calculated by subtracting the background mean gray value from the mean gray value in the RNAi-expressing cells.

Statistical Analysis

Excel was used to perform Student's t-test where indicated.

REFERENCES

1. Parrish JZ, Xu P, Kim CC, Jan LY, & Jan YN (2009) The microRNA bantam functions in epithelial cells to regulate scaling growth of dendrite arbors in drosophila sensory neurons. *Neuron* 63(6):788-802.
2. Hietakangas V & Cohen SM (2009) Regulation of tissue growth through nutrient sensing. *Annu Rev Genet* 43:389-410.
3. Boulan L, Milan M, & Leopold P (2015) The Systemic Control of Growth. *Cold Spring Harb Perspect Biol* 7(12).
4. Lanet E & Murance C (2014) Building a brain under nutritional restriction: insights on sparing and plasticity from Drosophila studies. *Front Physiol* 5:117.
5. Cheng LY, *et al.* (2011) Anaplastic lymphoma kinase spares organ growth during nutrient restriction in Drosophila. *Cell* 146(3):435-447.
6. Tang HY, Smith-Caldas MS, Driscoll MV, Salhadar S, & Shingleton AW (2011) FOXO regulates organ-specific phenotypic plasticity in Drosophila. *PLoS Genet* 7(11):e1002373.
7. Grewal SS (2009) Insulin/TOR signaling in growth and homeostasis: a view from the fly world. *Int J Biochem Cell Biol* 41(5):1006-1010.
8. Kumar V, Zhang MX, Swank MW, Kunz J, & Wu GY (2005) Regulation of dendritic morphogenesis by Ras-PI3K-Akt-mTOR and Ras-MAPK signaling pathways. *J Neurosci* 25(49):11288-11299.
9. Jaworski J, Spangler S, Seeburg DP, Hoogenraad CC, & Sheng M (2005) Control of dendritic arborization by the phosphoinositide-3'-kinase-Akt-mammalian target of rapamycin pathway. *J Neurosci* 25(49):11300-11312.
10. Laplante M & Sabatini DM (2012) mTOR signaling in growth control and disease. *Cell* 149(2):274-293.
11. Koike-Kumagai M, Yasunaga K, Morikawa R, Kanamori T, & Emoto K (2009) The target of rapamycin complex 2 controls dendritic tiling of Drosophila sensory neurons through the Tricornered kinase signalling pathway. *EMBO J* 28(24):3879-3892.

12. Scott RC, Juhasz G, & Neufeld TP (2007) Direct induction of autophagy by Atg1 inhibits cell growth and induces apoptotic cell death. *Curr Biol* 17(1):1-11.
13. Mizushima N & Komatsu M (2011) Autophagy: renovation of cells and tissues. *Cell* 147(4):728-741.
14. Hale AN, Ledbetter DJ, Gawriluk TR, & Rucker EB, 3rd (2013) Autophagy: regulation and role in development. *Autophagy* 9(7):951-972.
15. Ban BK, *et al.* (2013) Autophagy negatively regulates early axon growth in cortical neurons. *Mol Cell Biol* 33(19):3907-3919.
16. Takats S, *et al.* (2013) Autophagosomal Syntaxin17-dependent lysosomal degradation maintains neuronal function in Drosophila. *J Cell Biol* 201(4):531-539.
17. Han C, *et al.* (2012) Integrins regulate repulsion-mediated dendritic patterning of drosophila sensory neurons by restricting dendrites in a 2D space. *Neuron* 73(1):64-78.
18. Grueber WB, Jan LY, & Jan YN (2002) Tiling of the Drosophila epidermis by multidendritic sensory neurons. *Development* 129(12):2867-2878.
19. Grueber WB, Ye B, Moore AW, Jan LY, & Jan YN (2003) Dendrites of distinct classes of Drosophila sensory neurons show different capacities for homotypic repulsion. *Curr Biol* 13(8):618-626.
20. Dong X, Shen K, & Bulow HE (2015) Intrinsic and extrinsic mechanisms of dendritic morphogenesis. *Annu Rev Physiol* 77:271-300.
21. Jiang N, Soba P, Parker E, Kim CC, & Parrish JZ (2014) The microRNA bantam regulates a developmental transition in epithelial cells that restricts sensory dendrite growth. *Development* 141(13):2657-2668.
22. Watanabe K, Furumizo Y, Usui T, Hattori Y, & Uemura T (2017) Nutrient-dependent increased dendritic arborization of somatosensory neurons. *Genes Cells* 22(1):105-114.
23. Gokhale RH & Shingleton AW (2015) Size control: the developmental physiology of body and organ size regulation. *Wiley Interdiscip Rev Dev Biol* 4(4):335-356.
24. Hennig KM & Neufeld TP (2002) Inhibition of cellular growth and proliferation by dTOR overexpression in Drosophila. *Genesis* 34(1-2):107-110.
25. Hegedus K, *et al.* (2016) The Ccz1-Mon1-Rab7 module and Rab5 control distinct steps of autophagy. *Mol Biol Cell* 27(20):3132-3142.
26. Lorincz P, Mauvezin C, & Juhasz G (2017) Exploring Autophagy in Drosophila. *Cells* 6(3).
27. Mizushima N, Yoshimori T, & Ohsumi Y (2011) The role of Atg proteins in autophagosome formation. *Annu Rev Cell Dev Biol* 27:107-132.
28. Paik JH, *et al.* (2009) FoxOs cooperatively regulate diverse pathways governing neural stem cell homeostasis. *Cell Stem Cell* 5(5):540-553.
29. Renault VM, *et al.* (2009) FoxO3 regulates neural stem cell homeostasis. *Cell Stem Cell* 5(5):527-539.
30. de la Torre-Ubieta L, *et al.* (2010) A FOXO-Pak1 transcriptional pathway controls neuronal polarity. *Genes Dev* 24(8):799-813.
31. Sears JC & Broihier HT (2016) FoxO regulates microtubule dynamics and polarity to promote dendrite branching in Drosophila sensory neurons. *Dev Biol* 418(1):40-54.
32. Salih DA, *et al.* (2012) FoxO6 regulates memory consolidation and synaptic function. *Genes Dev* 26(24):2780-2801.

33. Christensen R, de la Torre-Ubieta L, Bonni A, & Colon-Ramos DA (2011) A conserved PTEN/FOXO pathway regulates neuronal morphology during *C. elegans* development. *Development* 138(23):5257-5267.
34. Nechipurenko IV & Broihier HT (2012) FoxO limits microtubule stability and is itself negatively regulated by microtubule disruption. *J Cell Biol* 196(3):345-362.
35. Lee JA (2012) Neuronal autophagy: a housekeeper or a fighter in neuronal cell survival? *Exp Neurobiol* 21(1):1-8.
36. Schaffner I, *et al.* (2018) FoxO Function Is Essential for Maintenance of Autophagic Flux and Neuronal Morphogenesis in Adult Neurogenesis. *Neuron*.
37. Son JH, Shim JH, Kim KH, Ha JY, & Han JY (2012) Neuronal autophagy and neurodegenerative diseases. *Exp Mol Med* 44(2):89-98.
38. Hara T, *et al.* (2006) Suppression of basal autophagy in neural cells causes neurodegenerative disease in mice. *Nature* 441(7095):885-889.
39. Yan Z, *et al.* (2013) *Drosophila* NOMPC is a mechanotransduction channel subunit for gentle-touch sensation. *Nature* 493(7431):221-225.
40. Turner HN, *et al.* (2016) The TRP Channels Pkd2, NompC, and Trpm Act in Cold-Sensing Neurons to Mediate Unique Aversive Behaviors to Noxious Cold in *Drosophila*. *Curr Biol* 26(23):3116-3128.
41. Hwang RY, *et al.* (2007) Nociceptive neurons protect *Drosophila* larvae from parasitoid wasps. *Curr Biol* 17(24):2105-2116.
42. Ferreira T, Ou Y, Li S, Giniger E, & van Meyel DJ (2014) Dendrite architecture organized by transcriptional control of the F-actin nucleator Spire. *Development* 141(3):650-660.
43. Stewart A, Tsubouchi A, Rolls MM, Tracey WD, & Sherwood NT (2012) Katanin p60-like1 promotes microtubule growth and terminal dendrite stability in the larval class IV sensory neurons of *Drosophila*. *J Neurosci* 32(34):11631-11642.
44. Han C, Jan LY, & Jan YN (2011) Enhancer-driven membrane markers for analysis of nonautonomous mechanisms reveal neuron-glia interactions in *Drosophila*. *Proc Natl Acad Sci U S A* 108(23):9673-9678.
45. Poe AR, *et al.* (2017) Dendritic space-filling requires a neuronal type-specific extracellular permissive signal in *Drosophila*. *Proc Natl Acad Sci U S A* 114(38):E8062-E8071.

CHAPTER 5

General Discussion

In this thesis, I presented two studies examining the regulation of sensory dendrite space-filling and scaling in *Drosophila* class IV (C4da) dendritic arborization neurons. With help from my collaborators, we identified mechanisms by which extracellular signals and the organism's nutritional environment influence dendrite development. I also described the optimization of a tissue-specific gene loss-of-function (LOF) strategy using the CRISPR/Cas9 system. These studies enhance our understanding of dendrite branching pattern formation in *Drosophila* sensory neurons and provide insights into general organization principles of the nervous system.

In Chapter 2, we determined that epidermal cell-derived heparan sulfate proteoglycans (HSPGs) act as permissive signals for C4da dendrite growth. Our results suggest that the HS chains either activate a novel neuronal receptor or act as coligands for an epidermal cell membrane protein or locally secreted molecule. Both scenarios lead to activation of an unknown receptor on the dendritic membrane resulting in microtubule stabilization. The identities of the potential coligands and neuronal receptor are currently not known, and therefore our results provide many exciting areas of future investigation. Recent evidence indicates that local levels of the epidermal cell-derived TGF- β ligand, Maverick (Mav), promote C4da dendrite growth and stability through the receptor tyrosine kinase (RTK), Ret. Similar to the HS chain knockdown phenotypes (Figure 2.1), Mav KD in a stripe of epidermal cells caused a local reduction in terminal dendrite growth in the RNAi-expressing region (1). Additional evidence indicates that Mav overexpression in subsets of epidermal cells directs C4da dendrite growth towards the higher Mav-expressing regions (1). This study suggests that Mav acts as a local epidermal cell-derived dendrite growth-promoting cue (1). Therefore, it is possible that HSPGs are necessary

for the local diffusion of Mav. In the future, it would be interesting to determine if HSPGs and Mav physically interact and act in the same genetic pathway to promote C4da dendrite growth.

Intriguingly, both Mav KD (1) and *ttv* KD (Figure 2.1) in stripes of epidermal cells caused a cell nonautonomous increase in terminal dendrites indicating that C4da neurons have an intrinsic need to grow a certain amount of dendrites in the dendritic field. This observation raises several interesting questions. First, what is the functional relevance of growing a certain level of terminal dendrites? How does the C4da neuron recognize when it has achieved the proper dendritic length requirements? Finally, what molecular mechanisms are responsible for regulating this phenomenon? Answering these questions would provide a more comprehensive understanding of dendritic field formation.

Another area of considerable interest is understanding the mechanisms by which the receptor protein tyrosine phosphatase (RPTP), Ptp69D, promotes C4da dendrite growth. Our data demonstrates that Ptp69D regulates dendritic growth in a HSPG-independent pathway. The molecular mechanisms are not known, however they provide another area for future analysis. A recent study determined that the RTK, Ret, is necessary for dendritic growth and stability. Ret LOF in C4da neurons causes incomplete coverage of the receptive field with reductions in total branch length and an increase in isoneuronal dendrite crossings (2). However, C4da-specific expression of a kinase-dead version of Ret in Ret LOF animals did not fully rescue the LOF phenotype, but caused a distinct dendritic reduction phenotype that is visually similar to the Ptp69D LOF phenotype (1). As RPTPs have been shown to phosphoregulate the kinase activity of RTKs (3), it is possible that Ptp69D normally dephosphorylates Ret to regulate C4da dendrite growth. In the future, it would be interesting to determine if Ptp69D interacts with Ret to promote dendrite growth.

In Chapter 3, our CRISPR-mediated tissue-restricted mutagenesis (CRISPR-TRiM) method revealed that many housekeeping genes such as components of the SNARE complex are made early in the neuronal cell lineage and are highly perdurant. Using the early-acting *SOP-Cas9* or analyzing dendrite regrowth in adult C4da neurons provide strategies for identifying the roles of perdurant genes in dendrite morphogenesis. The functions of housekeeping genes in dendrite development could also be investigated by combining the later-acting *ppk-Cas9* with tissue-specific gene knockdown using RNAi. While this strategy may be challenging genetically, it would alleviate larval lethality issues caused by the random epidermal cell expression of *SOP-Cas9* (Figure 3.S2P).

Using CRISPR-TRiM, we observed variable phenotypes among cells likely due to the nature of mutations induced by the CRISPR/Cas9 system. Each cell has its own unique gene mutation which can complicate phenotypic analysis of gene functioning. One way to improve our current system is to generate marked mutant cells using a CRISPR co-selection (co-CRISPR) strategy. This strategy has been used successfully in *Drosophila* to screen for CRISPR/Cas9-mutagenesis events using a sgRNA targeting an easily identifiable marker such as *ebony* or *white* and a sgRNA targeting a gene of interest (4, 5). These studies observed that fly lines with a mutation in the marker locus are more likely to also have a mutation in the gene of interest (4). In the future, it would be interesting to artificially label cells with a fluorescent reporter and then ubiquitously express sgRNAs against both the fluorescent reporter and a gene of interest. Therefore, cells in which the fluorescent reporter is absent are also likely to have LOF mutations for the gene of interest. An additional strategy to improve our CRISPR-TRiM technique would be to further optimize the gRNA efficiency by investigating the effect that changes in the gRNA scaffold have on mutagenesis frequency. A recent study in human red blood cells used a newly

optimized single-guide RNA scaffold to achieve efficient gene mutagenesis. Modifications to the sgRNA secondary structure improved sgRNA stability and editing efficiency (6). It would be interesting to determine if these sgRNA scaffold modifications improve gene mutagenesis of the redundantly acting SNARE components in *Drosophila* da neurons.

In Chapter 4, we found that C4da neurons show growth advantages over larval epidermal cell growth in low nutrient conditions. This study revealed differences in the cell-specific growth response to nutrient stress and raises several interesting questions. First, why do neurons develop more sensory dendrites in nutrient deprived conditions? Does this preferential growth of the dendrites under nutrient stress occur in other types of sensory neurons such as the *C. elegans* PVD neurons or zebrafish Rohon-Beard neurons? A comparison of dendrite morphologies in different sensory neurons under nutrient restriction would elucidate how conserved this phenomenon is in other organisms. In the future, it would be exciting to determine if preferential dendrite growth is beneficial to the organism for detecting changes in the sensory environment. Future studies will first determine if the nociceptive C4da neurons are more sensitive to noxious stimuli when they develop in nutrient poor conditions.

Additionally, our analysis determined that the growth of single neurons is influenced by the nutritional environment. We uncovered distinct molecular mechanisms that protect sensory neuron growth in the peripheral nervous system (PNS) and neural stem cell (neuroblast) division in the central nervous system (CNS) under nutrient deprivation. Neuroblasts in the CNS are insensitive to reductions in amino acids and insulin-like peptides due to the activity of the receptor tyrosine kinase, anaplastic lymphoma kinase (Alk) (7). Neuroblasts in early larval stages generate 90% of the neurons that will make up the adult CNS by dividing asymmetrically to give rise to another neuroblast and a ganglion mother cell (GMC). The GMC then divides to produce

either neurons or glia (8). However, it is not known what affect nutrient deprivation has on neurite growth in post-mitotic neurons in the *Drosophila* CNS. Would CNS neurons show similar responses to nutrient stress? What affect do changes in autophagy levels or FoxO activity have on neural development in the *Drosophila* brain? Answering these questions would provide additional insight into neuron/non-neural growth coordination throughout the nervous system.

REFERENCES

1. Hoyer N, *et al.* (2018) Ret and Substrate-Derived TGF-beta Maverick Regulate Space-Filling Dendrite Growth in *Drosophila* Sensory Neurons. *Cell Rep* 24(9):2261-2272 e2265.
2. Soba P, *et al.* (2015) The Ret receptor regulates sensory neuron dendrite growth and integrin mediated adhesion. *Elife* 4.
3. Tonks NK (2006) Protein tyrosine phosphatases: from genes, to function, to disease. *Nat Rev Mol Cell Biol* 7(11):833-846.
4. Kane NS, Vora M, Varre KJ, & Padgett RW (2017) Efficient Screening of CRISPR/Cas9-Induced Events in *Drosophila* Using a Co-CRISPR Strategy. *G3 (Bethesda)* 7(1):87-93.
5. Ge DT, Tipping C, Brodsky MH, & Zamore PD (2016) Rapid Screening for CRISPR-Directed Editing of the *Drosophila* Genome Using white Coconversion. *G3 (Bethesda)* 6(10):3197-3206.
6. Grevet JD, *et al.* (2018) Domain-focused CRISPR screen identifies HRI as a fetal hemoglobin regulator in human erythroid cells. *Science* 361(6399):285-290.
7. Cheng LY, *et al.* (2011) Anaplastic lymphoma kinase spares organ growth during nutrient restriction in *Drosophila*. *Cell* 146(3):435-447.
8. Homem CC & Knoblich JA (2012) *Drosophila* neuroblasts: a model for stem cell biology. *Development* 139(23):4297-4310.